STANDARD MODEL FOREGROUNDS IN NUCLEAR AND PARTICLE ASTROPHYSICS

BY

NACHIKETA CHAKRABORTY

DISSERTATION

Submitted in partial fulfillment of the requirements
for the degree of Doctor of Philosophy in Astronomy
in the Graduate College of the
University of Illinois at Urbana-Champaign, 2013

Urbana, Illinois

Doctoral Committee:

Professor B. D. Fields, Chair
Professor P. M. Ricker
Associate Professor A. J. Kemball
Professor J. C. Peng

Abstract

Nuclear and particle astrophysics comprises of applying standard principles of nuclear and particle physics to astronomical systems and making predictions for observation. Also, extreme environments in astronomical systems often serve as a probe for re-evaluating fundamental principles of physics and astronomy. The research described here comprises of both these aspects of nuclear and particle astrophysics. There are two broad themes : primordial nucleosynthesis and cosmic gamma-ray sources. As a part of the first theme, the "cosmological lithium problem", and a possible nuclear physics solution to it is examined. The theoretical prediction of the abundance of ^{7}Li produced in the big bang exceeds the observationally inferred abundance by a factor of 3-4, that is very difficult to explain within the Standard Model of particle physics and cosmology. The possibility of missed nuclear resonances in the network of nuclear reactions used to compute the theoretical primordial abundance is discussed. Three such candidate resonances are found prompting experiments to either find them or rule them out. In the light of recent experiments eliminating the most promising of these candidates, requirement of new physics beyond the Standard Model looms large as a a possible solution. In the second area of research, properties of cosmic gamma-ray emitting sources such as star forming galaxies and blazars are studied. The gamma-ray sky has contributions from these guaranteed sources and potentially others such as particle dark matter. In the light of this, gamma-rays properties of the guaranteed astronomical sources as spectral slope, photon count statistics and polarisation of X-rays and soft gamma-rays is studied in the hope of achieving the broad goal of understanding the underlying physics of radiative emission of these sources and hopefully disentangling these "foregrounds" from

other exotic sources such as particle dark matter.

Acknowledgments

My research and life in general throughout my Ph.D. would not have been successful without the contribution of several people.

First and foremost, my advisor Brian Fields has and continues to be a tremendous institution for my training as a scientist. In a profession where the input of your mentor is paramount, I have been fortunate to have a phenomenal scientist and a superlative person to mould me into a scientist. I have learnt everything from scientific aspects of astrophysics to the social aspects of building collaborations with other scientists from Brian. Alongside doing good research, communicating it well is also very important. In this aspect, my communication skills through talks and other means have improved significantly under Brian's tutelage. My entire research experience with Brian has been a thoroughly enjoyable experience. I am very, very lucky to have forged a strong, fruitful collaboration with a scientist and person, I deeply admire. And I sure wish to continue working on interesting projects with Brian throughout my career.

I have also been very fortunate to work with Prof. Athol Kemball. It was terrific fun to do radio astronomy stuff with him, which brought back memories of my Master's research. My training with him in technical aspects of the field was also, in no small part responsible for my successful application with my future employers. He has been extremely kind to me and I hope to continue our collaboration in future.

Also, I have been privileged to have worked with two giants of particle physics and astrophysics, Prof. Keith Olive and Prof. Scott Dodelson. My first paper with Prof. Olive was a huge learning experience, and absolute delight and occasional fright to keep up with

the lightning speed of thought and profound depth of understanding. Having read Prof. Dodelson's book on Modern Cosmology and papers, collaborating with him has been a highlight of my Ph.D. work. Once, again it was a lot of fun in addition to being a huge challenge to try to keep up with the high standards of research.

The support and encouragement of senior graduate students is very important to the growth of a new graduate student. I have been very fortunate to have wonderful seniors who have become great friends aside from being fine examples to look upto.

My friend and senior at UIUC, Rishi Khatri has been a huge influence and support even before the time I reached UIUC. From helping me settle down in a new country to guiding me about some research decisions with his characteristic candour, he has and continues to be an inspiration and an excellent friend.

One of my most favourite persons who also belongs to the Fields research family and has been a very good friend and a part of my research support system is Amy Lien. She is without a doubt, a true protege of Brian, always being the nicest person and also an excellent scientist. My collaboration and friendship with Amy has enriched my life as a graduate student, and I cherish our friendship and collaboration.

Another member of the Fields research family, the prolific Vasiliki Pavlidou has been a tremendous source of encouragement and inspiration. I have begun collaborating with Vaso towards the end of my Ph.D. and I look forward to many papers together. I also, look forward to her eminently enjoyable company as I head to Europe.

My life as a graduate student has been so very enjoyable due to the presence of good friends in this very tightly knit department. Kuo-Chuan Pan, I-Jen, Hotaka, Yiran and David have been wonderful friends and classmates. They have always been there for me research and otherwise. I will always have fond memories of all the fun times we have had together as a group and feel lucky to have made such good friends.

This department and its various members have been very kind and helpful to me at every step of my six years of graduate life. Jeri, Mary-Margaret, Sandy, Bryan and Judy have been

extremely helpful and made it so much easier for me to do my research with everything else taken care of. I certainly owe them a lot for comfortable life as a graduate student. And Jeri, of course, is the kindest and sweetest person on this planet ! I will miss her a lot along with everyone else in the department.

A huge part of my support system in Urbana-Champaign, are my friends from outside the astronomy department. I cherish my friendship with Vineeth, Sarang, Pragnyadipta, Sandeep, Vineet, Anika and the quintessential scientist Ritoban Basu Thakur. They have all been of tremendous help in me settling down in the US and shared an unforgettable common experience. My times spent taking classes and discussing science with Rito or RBT, is something that has helped me strive towards doing exciting science. He has made me better at being a scientist. Sandeep has been the most influential, my mentor at physical training which has made me a lot sharper at my work. Indeed their friendship has been invaluable and the gain of a lifetime that I take back with me.

Finally, my family including my parents, grandparents and my wife Soma, has been my ultimate support system that made it possible for me to stay away from them and yet function with some degree of success. My parents have been instrumental in me pursuing science while being in India, still not a very popular choice. However, their atypical choices have inspired me to do the same. Its their constant support and encouragement in chasing my ambition of being a physicist that has given me freedom to do what I want, the way I want. My father, Maloy who did his Ph.D. in Chemistry has always been a great source of support, inspiration and encouragement taking a lot of detailed interest in my career. The pride my parents take in my accomplishments is the biggest reward I gain.

My wife Soma has been the ideal partner in every possible way. It is testament to her character, that she has never made us feel the geographical distance and has been central to my growth as a scientist and person. She has helped me maintain the balance of the personal and the professional in my life, impeccably. Being a researcher herself, Soma has shown great patience and understanding throughout my Ph.D. and given a lot of importance

to the accomplishment of my long and short term goals. At the same time, she has kept me honest with my feet on the ground at all times. And therefore, when in doubt both professionally and personally, she is the one I go to. I look forward to my future with her in Europe. I hope, we can continue to support and improve each other as a scientist and a person.

This work is a culmination of contributions from all these people, and particularly my family. I dedicate my thesis to my family, particularly my beloved late grandfather who has always had a lot of pride in my achievements.

Table of Contents

Chapter 1

Introduction

Nuclear and particle astrophysics comprises of applying standard principles of nuclear and particle physics to astronomical systems and making predictions for observation. Also, extreme environments in astronomical systems often serve as a probe for re-evaluating fundamental principles of physics. The research in this thesis comprises of both these aspects of nuclear and particle astrophysics. One of the first steps in exploring new fundamental physics with astrophysical probes, is to attain a systematic and comprehensive understanding of the standard astrophysical processes and sources. Only after modeling these astrophysical "foregrounds" can we confidently constrain models beyond the Standard Model of particle physics and cosmology. With this broad vision in mind, I have worked on various projects in the areas of primordial nucleosynthesis, the cosmic gamma-rays, high energy polarisation, forecasting radio supernovae discovery, etc.

1.1 Primordial nucleosynthesis

As a part of the first topic, I have worked on the "Cosmological Lithium Problem". The big bang produces light elements namely H, He, Li and isotopes and isobars. And comparison of theoretical predictions about the production of these elements with observations constrains big bang cosmology (Wagoner et al., 1967a; Kolb & Turner, 1990; Cyburt, 2004a; Steigman, 2007, etc.). Big bang nucleosynthesis represents the competition between rate of nuclear, weak and electromagnetic reactions, Γ and the expansion rate of the universe, or the Hubble rate, $H = \dot{a}/a$. Here a is the scale factor by which is unity at the present moment. The

reactions proceed to produce and destroy nuclei and achieve nuclear statistical equilibrium between the various production and destruction reactions. This depends on the temperature of the universe and also the baryon $n_{\rm b}$ and photon densities n_γ. In equilibrium, the rate of interactions per particle exceed the expansion rate as

$$\Gamma = n\sigma v \gg H \tag{1.1}$$

where σ is the interaction cross-section. Nucleosynthesis is quantified by through abundances. And abundance of an element i is defined in terms of mole fraction $Y_{\rm i} = n_{\rm i}/n_{\rm b}$, with respect to the baryon density of the universe at the time. The abundances are defined to be the mole fractions, given relative to hydrogen, as

$$\frac{Y_{\rm i}}{Y_{\rm H}} = \frac{n_{\rm i}/n_{\rm b}}{n_{\rm H}/n_{\rm b}} \tag{1.2}$$

The dilution in the amount of these elements due to the expansion is precisely calculable and a common factor for all nuclei. $Y_{\rm i}$ is thus independent of this dilution factor. More quantitatively the nuclear statistical equilibrium for a nucleus with abundance Y can be quantified in terms of the abundances of projectiles, $Y_{\rm proj}$ that produce it at a rate $\Gamma_{\rm prod}$ and destruction rates, $\Gamma_{\rm dest}$

$$\begin{aligned} \frac{dY}{dt} &= n_{\rm b}\Big(\sum_{prod} Y_{proj}\Gamma_{\rm prod} - \sum_{dest} Y\Gamma_{\rm dest}\Big) \\ => \frac{a}{Y_{\rm eq}}\frac{dY}{da} &= -\frac{\Gamma}{H}\left(\left(\frac{Y}{Y_{\rm eq}}\right)^2 - 1\right) \end{aligned} \tag{1.3}$$

and the equilibrium abundance corresponding to $\Gamma \gg H$ is

$$Y_{\rm eq} = \frac{\sum Y_{proj}\Gamma_{\rm prod}}{\sum \Gamma_{\rm dest}} \tag{1.4}$$

These abundances are functions of the temperature and also the baryon-to-photon ratio. Now as the universe undergoes accelerated expansion, the expansion rate exceeds the production and destruction reactions. As a result of this, different reactions fall out of equilibrium, and the abundances set by those reactions are held fixed aside from the obvious dilution due to expansion. This is falling out of equilibrium is known as "freeze-out" and the condition is given as

$$\Gamma \approx H \tag{1.5}$$

Once, the expansion rate, H far exceeds reaction rate, Γ the abundances, Y are fixed. These frozen out abundances depend only upon the baryon-to-photon density ratio represented by $\eta = n_{\rm b}/n_\gamma \propto \Omega_{\rm b}/\Omega_\gamma$. Here the $\Omega' s$ are ratio of matter-energy density of that component to the critical density required to close the universe i.e. keep it from expanding forever.

Nucleosynthesis occurs at MeV energies and finishes within the first 3 minutes post the big bang. It begins with protons and neutrons combining to produce deuterium. Weak interactions interconvert neutrons and protons and when expansion exceeds the weak interaction scale, the weak freezeout occurs setting the neutron to proton ratio $\left(\frac{n}{p}\right) \sim 1/6$. The neutron decays with a mean lifetime of ~ 882 seconds. So a further decay of neutrons reduces this ratio to 1/7, and this is when nucleosynthesis begins at the scale of the weak freezeout i.e. at MeV temperatures. However, in addition to nucleons, there are about a billion times as many photons in the radiation dominated universe at the time. This prevents neutrons and protons from combining effectively. As a result, deuterium is photo-disintegrated as soon as it is produced. This continues till about 100 seconds, at which point the universe cools to below the binding energy of deuterium and "bottleneck" is released. Nucleosynthesis proceeds to produce He and Li. The abundances of these elements after their respective freezeouts are functions of the baryon-to-photon ratio alone. Therefore, observations of the elemental abundances put constraints on this baryon-to-photon ratio other than parameters like the

gravitational constant, number of relativistic species, etc. that are fixed within the Standard Model of nuclear and particle physics and cosmology. And through the baryon-to-photon ratio or simply the baryon density, these abundances put constraints on big bang cosmology (Kolb & Turner, 1990).

Further advances in the measuring the cosmic microwave background (CMB) have made it a more precise baryometer than big bang nucleosynthesis (BBN) (Kneller et al., 2001; Cyburt et al., 2003; Cuoco et al., 2004). Using the CMB value of $\Omega_{\rm b}$, it possible to make predictions for the elemental abundances of elements deuterium, tritium, helium and lithium and isobars and isotopes. And these can be compared with observations. Thus, within the framework of the Standard Model of particle physics and cosmology, there is no room / freedom for adjusting the theoretical predictions of light elemental abundances.

Ideally, one would hope to observe these elements in pristine sites unpolluted by post BBN- processing. However, in practice the observations are often affected by non-primordial processes as stellar nucleosynthesis (For eg., Korn et al., 2006), cosmic rays and other astronomical processes. Constraints from CMB are either weak as in the case of ^{4}He or unattainable due to the very nature of recombination. So the observations need to be performed at the metal poor astronomical sites, minimally polluted by the heavier elements or "metals" produced by aforementioned processes. ^{4}He is observed in metal poor compact dwarfs (Izotov et al., 1999). D is constrained from quasar absorption lines (O'Meara et al., 2006; Fumagalli et al., 2011). ^{3}He is observed in Galactic HII regions (Bania et al., 2002). Observations of ^{7}Li are performed at multiple sites as metal poor halo field stars (For e.g. Spite & Spite, 1982; Ryan et al., 2000; Asplund et al., 2006) , globular cluster stars (Bonifacio et al., 2002; Bonifacio, 2002; González Hernández et al., 2009) and more recently, in the Small Magellanic Cloud (Howk et al., 2012). The ^{7}Li observations in metal poor halo stars show signs of a plateau called the "Spite Plateau" with a small scatter consistent with observational uncertainties. This suggests that the abundance is primordial. The observations (Ryan et al., 2000) however, show an abundance 3-4 times less (Cyburt et al., 2008) than

predicted by standard BBN theory. This is known as the cosmological lithium problem.

One possible solution to the lithium problem is to look at nuclear reactions destroying ^{7}Li or ^{7}Be. ^{7}Be is important as it is predominantly in this isobaric form that mass 7 nuclei are formed in the early universe. Being β unstable it undergoes decay to produce the lithium that is ultimately observed. The theoretical computation of the elemental abundances are made by evolving the nuclear reactions both production and destruction, with the expansion of the universe (Wagoner et al., 1967a; Smith et al., 1993). This in principle requires a complete database of nuclear reactions whose properties are measured experimentally. In practice, there are 12 important reactions including the neutron decay Smith et al. (1993). Nuclear reactions that compete with these reactions that were either missed before or have newer measurements will alter the abundances. Also, alternate nuclear channels, defined by the quantum state of the reactants in these reactions, which were missed should also be accounted for.

In Chakraborty et al. (2011), a systematic and complete study of these effects were made. The ^{7}Li and ^{7}Be production reactions are very well measured leaving very little scope for further exploration. So only destruction reactions need to be considered. It was found from a semi-analytic estimate that only nuclear resonances were competitive enough with the 12 key reactions to alter the ^{7}Li or ^{7}Be abundances. This is based on the equilibrium abundance in eq. 1.4). Thereby, a complete, systematic study of such resonances destroying ^{7}Li and ^{7}Be down to observed abundances was made. The existence of such a resonance would represent a nuclear solution to the cosmological ^{7}Li problem that doesn't require any new physics beyond the Standard Model of particle physics and cosmology.

In doing so, data on resonances was used from resources such as NACRE [1], TUNL [2], NNDC [3], etc. to construct resonant reaction rates to expand the nuclear reaction network (Caughlan & Fowler, 1988; Angulo et al., 1999), in addition to the existing non-resonant

[1] *http://pntpm3.ulb.ac.be/Nacre/barre_database.htm*
[2] *http://www.tunl.duke.edu/nucldata/*
[3] *http://www.nndc.bnl.gov/*

contributions. Resonant energies and widths were parametrised where data was not available and constrained the parameter space where ^{7}Li acquires observed values. In doing so I also, computed the amounts of heavier elements like ^{9}Be are not overproduced by these destruction reactions. Three candidate resonant levels for the initial states $^7\mathrm{Be} + d$, $^7\mathrm{Be} + t$ and ^{7}Be+^{3}He were found to have inelastic exit channels including p,^{3}He and ^{4}He which could not be immediately dismissed based on the data on channel energies and widths available then. However, owing to large Coulomb barriers, they all needed large channel radii ($a > 10$ fm) for solving the ^{7}Li problem which makes this very difficult. More recently, ^{7}Be + d channel was ruled out explicitly by new data. This strongly suggests that systematically accounting for standard nuclear physics cannot by itself solve the ^{7}Li problem. As a result, the ^{7}Li problem may point to physics beyond the Standard Model of particle physics and cosmology. These results along with work of others (Cyburt & Pospelov, 2012; Boyd et al., 2010a) have prompted experiments (Charity et al., 2011; Kirsebom & Davids, 2011; O'Malley et al., 2011) to look for these resonances. And these experiments have ruled out the best candidate(s) as solutions to the lithium problem.

In absence, of this solution, it is a possibility that new physics beyond the Standard Model has to be invoked in order to find a theoretical solution to the lithium problem. Several ways of destroying exist from dark matter decay (Jedamzik, 2004; Jedamzik & Pospelov, 2009; Ellis et al., 2005, etc.), variation of fundamental constants like quark masses (Dmitriev et al., 2004), neutron lifetime, (Coc et al., 2007, etc.), etc., to formation of bound states (Cyburt et al., 2006, etc.). Another class of solutions lies in stellar depletion of lithium in stars via rotational mixing, turbulence, diffusion, etc (For e.g. Meléndez et al., 2010b). Aside from ways of destroying lithium, a reinterpretation of the observations due to an improved model of stellar atmospheres may modify and reconcile the observed abundance with the theoretical predictions (For e.g. Meléndez et al., 2010a)

1.2 Cosmic gamma-rays

High energy radiation provides a natural, astrophysical probe to the some of the highest energy phenomena and particles in the universe, all the way upto Planck scales. Thus, cosmic gamma rays emitted by various astronomical sources both cosmological and local are a powerful probe to the high energy universe. With the advances in gamma-ray astronomy and the current state of the art with *Fermi* -LAT, it has become possible to investigate individually interesting sources as well as populations of sources such as star forming galaxies (Abdo et al., 2010f,a, etc.,), active galaxies or active galactic nuclei (Nolan et al., 2012a) (AGN), compact objects like gamma-ray bursts (Fermi-LAT Collaboration, 2013), ordinary black holes, etc. Now, in addition to known sources, gamma-rays are probes to the unknown and the exotic. Just as BBN, cosmic gamma-rays too are an indirect probe of particle dark matter (Ando et al., 2007; Regis & Ullio, 2008; Ackermann et al., 2012b). Dark matter decays and annihilations produce gamma-rays at various energies and studying their properties gives clues about dark matter models. However, it is crucial as in the case of BBN to eliminate all the Standard Model foregrounds that could mimic or distort the dark matter signature. Or alternately, we must model all the standard astrophysical sources that can explain the data before invoking physics beyond Standard Model as would be the case for dark matter. Therefore, even in the study of the dark matter, it is important to study the known sources mentioned before. Various properties of gamma-ray sources such as source spectra (Stecker & Venters, 2011; Lacki et al., 2012; Fields et al., 2010; Ackermann et al., 2012c), flux distribution and statistics (Abdo et al., 2010l; Malyshev & Hogg, 2011), anisotropies (Ackermann et al., 2012a; Hensley et al., 2010), etc. have been studied in order to firstly, understand the distinctive signatures of the various astrophysical sources producing gamma-rays. This is achieved by studying these properties of the resolved sources. Secondly, EGRET (Sreekumar et al., 1998) and now *Fermi* -LAT (Abdo et al., 2010j) has helped confirm the existence of a diffuse, extra-Galactic gamma-ray background (EGB). Efforts are on to try to identify the origin of this diffuse EGB. Blazars or AGNs with their jets pointed

towards the observer, have been identified as the being the dominant source class amongst the resolved sources. It is therefore natural to determine their contribution to the unresolved sources or diffuse background. It is clear from the results of various groups including ours (For eg Chakraborty & Fields, 2012; Stecker & Venters, 2011; Malyshev & Hogg, 2011) that the diffuse background is multi-component. It is unlikely to be dominated by AGNs due to guaranteed contribution from other sources mainly star forming galaxies Pavlidou & Fields (2002); Fields et al. (2010). Despite knowing this, there is still debate on the exact contribution of the star forming galaxies and AGNs, the two guaranteed sources of the EGB. It is important to sharpen the constraints on their relative contributions.

As individuals objects, star-forming galaxies are laboratories of cosmic ray physics with X-ray and gamma-ray telescopes being the apparatus. High energy radiation is produced in sites of supernova remnants (SNR) due to cosmic ray interactions. Therefore, the gamma-rays produced for instance are cosmic gamma rays. Multiwavelength observations provide evidence of cosmic ray acceleration in sites of SNR upto energies of $\sim 10^{15}$ eV (Uchiyama et al., 2007; Helder et al., 2009, etc.,). The cosmic ray flux $\phi_{\rm CR}$ is the proportional to the supernova rate. The supernova rate in turn, is proportional to the massive star-formation rate, which ties it to the gamma-ray luminosity in sites of SNR in star-forming galaxies. There exist direct connections between cosmic gamma rays and star-formation. This connection is manifested in the context of the gamma-ray luminosities of individual galaxies as well as the diffuse extra-Galactic gamma ray background (EGB).Star-forming galaxies produce gamma-rays by cosmic ray interactions with the interstellar medium (ISM). And therefore, the gamma-ray emissivity, q_γ is given in terms of the cosmic ray flux $\phi_{\rm CR}$ and the ISM density $n_{\rm ISM}$ as,

$$q_\gamma \sim \phi_{\rm CR} \sigma_{\rm int} n_{\rm ISM} \tag{1.6}$$

Gamma ray luminosities of individual star-forming galaxies are correlated to the galactic

star-formation rate and the cosmic star-forming background to the cosmic star-formation rate. The exact nature of the correlation depends on the emission mechanism, hadronic or leptonic and their efficiencies.

Star-forming galaxies from the Local Group have been detected at GeV energies by *Fermi* -LAT (Abdo et al., 2010g). In addition to the Milky Way this includes normal galaxies M 31(Abdo et al., 2010g), Large Magellanic Cloud (LMC) (Abdo et al., 2010h), Small Magellanic Cloud (SMC) (Abdo et al., 2010c) and starbursts M 82 and NGC 253 (Abdo et al., 2010b). M33 is very likely to be detected by *Fermi* -LAT in the upcoming years (Abdo et al., 2010g). It is believed that the dominant emission mechanism for Milky Way type galaxies GeV gamma-ray production is hadronic or due to interactions of cosmic ray protons with interstellar gas. (neutral, ionised and molecular hydrogen) to produce neutral pion that decay in flight into gamma rays. The gamma-ray emission can be viewed in terms of collisions between projectiles i.e. the cosmic ray protons with the targets i.e. the ISM protons.

$$p_{\rm CR} + p_{\rm ISM} \rightarrow p + p + \pi^0 \qquad \pi^0 \rightarrow \gamma\gamma \tag{1.7}$$

However, in some cases as in the Magellanic Clouds, this is not clear as the gas and the gamma rays show very little spatial correlation. The next most important process of producing gamma-rays is inverse-Compton scattering of cosmic ray electrons off the interstellar radiation field. Here the projectiles are the cosmic ray electrons and the targets are the ISRF photons.

$$e^-_{\rm CR} + \gamma_{\rm ISRF} \rightarrow e^- + \gamma_{\rm HE} \tag{1.8}$$

In order to determine the exact contribution of star forming galaxies, it is important to study the individual galaxies in detail as only the handful mentioned above have been detected in gamma-rays Abdo et al. (2010g) in contrast the vast majority of AGNs. There-

fore, while for AGNs a statistical understanding of the gamma-ray emission suffices, for star forming galaxies knowing details of the emission mechanisms in these handful are useful to extrapolate to get their cosmological emission. Emission mechanisms of the individual galaxies as well as the number density of these galaxies differ depending on whether they are a starburst that has heightened periods of star formation activity or not. The ones which dont have this starburst activity are called normal galaxies. Pavlidou & Fields (2002); Fields et al. (2010), computed a model for the hadronic emission due to neutral pion decay from normal star forming galaxies. This involves computation of the projectile or cosmic ray flux in terms of the star formation rate based on the aforementioned correlation and normalised to the Milky Way. The target density is the interstellar hydrogen density in various forms i.e. neutral, molecular and ionised. The relevant quantity here is the surface gas density that in turn is related to the surface density of star formation Kennicutt (1998). This implies that the gamma-ray luminosity L_γ is a non-linear function of the star formation rate ψ. This is a critical result from Pavlidou & Fields (2002); Fields et al. (2010) that sets the overall scaling relation between the gamma-ray luminosity and the star formation rate. The shape of course, is very well defined. A pion decaying at rest would have a delta function peak at the rest mass of 67.5 MeV. However, the pion decays in flight. Furthermore, Galactic rotation produces dispersion, and the peak becomes a bump. For external galaxies at cosmic distances, there is a redshifting as well. Using Hα as a tracer for these normal star forming galaxies, the distribution function is constructed. The intensity is then computed as the line of sight integral of product of the distribution as well as the luminosity of a single galaxy. Fields et al. (2010) find that the cosmological contribution of the normal galaxies due to neutral pion decay is significant and could in fact dominate the extra-Galactic diffuse background upto around 10 GeV. The LAT range of course, extends to around 300 GeV.

Given that the inverse-Compton contribution from normal galaxies is also guaranteed and the next most important, this contribution was computed in Chakraborty & Fields (2012). Also, since, the inverse Compton spectral shape is flatter at higher energies it

could apriori be significant at energies above 10 GeV. This provides strong motivation to perform this computation. This leptonic contribution has cosmic ray electrons as projectiles instead of protons. Once again as for protons, the cosmic ray electron flux scales as the star formation rate, being accelerated in the same SNR as protons. Their efficiency could be different though. Electrons propagate differently from the protons. Radiative losses are significant for electrons, unlike protons that are heavier. Also, while electrons diffuse they do not escape the galaxy whereas proton losses in the normal galaxies are dominated by escape. The radiative energy lost by electrons is equal to the energy output in photons at various energies depending on loss mechanism. This is known as calorimetry. For instance, synchrotron losses produce photons from radio all the way to X-rays. Inverse Compton losses produce some X-rays and certainly gamma-rays. And thus the gamma-ray IC emission is basically the fraction of the total energy lost in IC. As a result the gamma-ray luminosity depends not the the background seed photon or ISRF density, but fraction of IC. Once again from the luminosity and the Hα distribution the intensity of cosmological emission is computed.

1.3 High energy polarisation

In section 1.2, gamma-ray properties of star forming galaxies and AGNs discussed include the source intensity, spectra, flux distribution, etc. A property with tremendous scientific potential in gamma-ray and even X-ray astronomy that is being explored more recently (For e.g. McNamara et al., 2009; Krawczynski, 2012; Weisskopf et al., 2010) is polarisation. Measurement of polarisation at X-ray and even soft gamma-rays is very challenging. But several experiments in various stages of operation, design and commission are about to change this and open a new window of opportunities in investigating extreme objects like AGNs, GRBs, black holes in general, neutron stars, etc (McNamara et al., 2009; Krawczynski, 2012; Götz et al., 2009). Some of the above sources are either established as or candidates

for particle accelerators all the way upto nearly the ankle of the cosmic ray spectrum ($\sim 10^{19}$eV). HIgh energy polarisation will probe of emission mechanisms that in turn will probe acceleration mechanisms and thereby test the particle accelerators. Magnetic fields can lead to polarised emission. And therefore, polarisation measurements will help understand magnetic field structure surrounding the astronomical sources.

Lorentz invariance is one of the treasured symmetries in the Standard Model of particle physics and cosmology. But certain particle physics and gravity models have Lorentz invariance violation built into them. Gamma rays can be used to probe these models in many ways (Coleman & Glashow, 1999; Ellis et al., 2000) One of the ways is to measure vacuum birefringence, or modification of the dispersion relation of light due to Lorentz violating terms in the underlying Lagrangian. Thus, putting constraints on these terms puts constraints on Lorentz violation. This modified dispersion relation leads to a rotation of polarisation during propagation of the photons. INTEGRAL / IBIS observations of the polarisation from the prompt emission from the GRB041219A has put a strong limit on the cubic correction term to the standard dispersion relation (Laurent et al., 2011)limiting the LIV parameter to $< 1.110 \times 10^{-14}$, an improvement of 4 orders of magnitude over the previous limit. This limit is inversely proportional to the distance, which suggests that polarisation measurements of higher redshift GRBs can in principle improve the limits further.

In particular, polarised X-rays and gamma-rays from AGNs have the potential to reveal a lot of different aspects on AGN physics. AGNs are some of the most luminous yet mysterious astronomical objects in the universe. Their particle and radiative emissions are powered by a central supermassive black hole accreting matter. Part of the gravitational energy associated with accretion is converted into energy of particles such as cosmic rays and neutrinos and high energy radiation like X-rays and gamma-rays. Thus, these particles and radiation are messengers of the extreme astrophysical conditions in the core of active galaxies. Blazars are distant AGNs where the observer's line of sight is along the jet axis, i.e. the observer looks down into the jets. Various properties of the radiation from blazars like the overall inten-

sity, spectrum, variability have been studied with multiwavelength observations. However, polarisation particularly at high energies has received much less attention. However, with numerous X-ray and soft gamma-ray polarimeters at various stages of planning, design and operation and studies of optical / FIR polarisation properties of blazars underway, this is a perfect time to calculate high energy polarisation from blazars. High energy polarisation is a key ingredient in the multimessenger, multiwavelength understanding of blazars.

1.4 Radio Supernovae

Yet another piece in this gamma-ray - star formation connection are core collapse SNe. Core collapse SNe are result of death of massive stars. And hence, the core collapse SNe rate traces the massive star formation rate. In fact, they are in direct proportion to each other. Thus building up a statistically significant sample of core-collapse SNe constitutes an independent probe of the star formation rate. Core collapse SNe have been observed to emit radio. Over 50 of them have been discovered with the current generation of radio telescopes. However, with future generations of radio surveys that represent more than an order of magnitude improvement in sensitivity, it is possible to discover many more core collapse SNe. This discovery potential is explored in Lien et al. (2011). Radio has the capability to go deeper than optical in discovering supernovae. The large optical telescopes such as the Large Synoptic Survey Telescope (LSST) will detect a plethora of core-collapse supernovae out to redshift 1. However, it is estimated by Mannucci et al. (2007) that $\sim 60\%$ of core collapse supernovae maybe missed in optical surveys due to increased dust obscuration at high redshift. In our work in Lien et al. (2011) , it was shown that future generations of radio telescopes in survey mode such as SKA and its precursors will detect a large fraction of core-collapse SNe as predicted from the cosmic massive star-formation rate in Horiuchi et al. (2009a) out to redshift 5. Also, future radio telescope arrays could be trained with simultaneous or triggered with preceding optical detections at low redshift.

And using this knowledge about radio supernovae at low redshift, they could be used for independent discoveries at high redshift. Also, there is a potential shift in the detection strategies from mainly targeted PI driven searches to untargeted, synoptic surveys capable of detecting radio supernovae automatically.

The radio emission comes from the interaction of the wind with the circumstellar medium. So other simply building a sample, naturally, the radio emission is a probe of the models of the circumstellar medium and its various parts Chevalier (1982a,b).

About 25% of core-collapse SNe are Type 1bc Li et al. (2011a), which are related to long GRBs. According to our estimate with very conservative assumptions about fraction of radio emitting Ibc SNe, we expect SKA to make ~ 130 unbiased, untargeted detections, with ~ 20 connected with GRBs. Aside from these, exotic transients whose properties do not match those of known transient sources are yet another discovery pool.

A synoptic survey in radio wavelengths will be crucial in many fields of astrophysics, particularly for RSNe, but also for other transients. It will bring the first complete and unbiased RSN sample and systematically explore exotic radio transients. SKA will be capable of performing such an untargeted, possibly automated survey with its unprecedented sensitivity. Our knowledge of supernovae will thus be firmly extended into the radio and to high redshifts.

Chapter 2

Resonant Destruction of Lithium During Big Bang Nucleosynthesis

Abstract

[1] We explore a nuclear physics resolution to the discrepancy between the predicted standard big-bang nucleosynthesis (BBN) abundance of ^{7}Li and its observational determination in metal-poor stars. The theoretical ^{7}Li abundance is 3 - 4 times greater than the observational values, assuming the baryon-to-photon ratio, $\eta_{\rm wmap}$, determined by WMAP. The ^{7}Li problem could be resolved within the standard BBN picture if additional destruction of $A = 7$ isotopes occurs due to new nuclear reaction channels or upward corrections to existing channels. This could be achieved via missed resonant nuclear reactions, which is the possibility we consider here. We find some potential candidate resonances which can solve the lithium problem and specify their required resonant energies and widths. For example, a 1^- or 2^- excited state of ^{10}C sitting at approximately 15.0 MeV above its ground state with an effective width of order 10 keV could resolve the ^{7}Li problem; the existence of this excited state needs experimental verification. Other examples using known states include $^7{\rm Be} + t \rightarrow {}^{10}{\rm B}(18.80\ {\rm MeV})$, and $^7{\rm Be}{+}d \rightarrow {}^9{\rm B}(16.71\ {\rm MeV})$. For all of these states, a large channel radius ($a > 10$ fm) is needed to give sufficiently large widths. Experimental determination of these reaction strengths is needed to rule out or confirm these nuclear physics solutions to the lithium problem.

[1]This chapter is previously published in The Physical Review D as Chakraborty, N., Fields, B. D., & Olive, K. A. 2011, Phys. Rev. D, vol. 83 pp. 63006. This chapter matches the published version aside from superficial modifications to references.

2.1 Introduction

Primordial nucleosynthesis continues to stand as our earliest probe of the universe based on Standard Model physics. Accurate estimates of the primordial abundances of the light elements D, ^{4}He and ^{7}Li within standard Big Bang Nucleosynthesis (BBN) Cyburt et al. (2001); Coc et al. (2004a); Cyburt et al. (2003); Cyburt (2004b); Cyburt et al. (2008) are crucial for making comparisons with observational determinations and ultimately testing the theory. Primordial abundances are also a probe of the early universe physics Cyburt et al. (2005). Currently, the theoretical estimates of D and ^{4}He match the observational values within theoretical and observational uncertainties Cyburt et al. (2003, 2008) at the baryon-to-photon ratio determined by the 7-year WMAP data, $\eta_{\rm wmap} = 6.19 \pm 0.15 \times 10^{-10}$ Komatsu et al. (2011). In contrast, the theoretical primordial abundance of ^{7}Li does not match the observations.

At $\eta_{\rm wmap}$, the predicted BBN abundance of ^{7}Li is[2] Cyburt et al. (2008)

$$\left(\frac{^7\mathrm{Li}}{\mathrm{H}}\right)_{\rm BBN} = \left(5.12^{+0.71}_{-0.62}\right) \times 10^{-10}. \tag{2.1}$$

The observed ^{7}Li abundance is derived from observations of low-metallicity halo dwarf stars which show a plateauSpite & Spite (1982) in (elemental) lithium versus metallicity, with a small scatter consistent with observational uncertainties. An analysis Ryan et al. (2000) of field halo stars gives a plateau abundance of

$$\left(\frac{\mathrm{Li}}{\mathrm{H}}\right)_{\rm halo\star} = \left(1.23^{+0.34}_{-0.16}\right) \times 10^{-10}. \tag{2.2}$$

However, the lithium abundance in several globular clusters tends to be somewhat higher Bonifacio (2002); González Hernández et al. (2009), and a recent result found in González Hernández et al. (2009) gave ^{7}Li/H $= (2.34 \pm 0.05) \times 10^{-10}$. Thus the theoretically es-

[2]Note that the ^{7}Li abundance reported here differ slightly from that given in Cyburt et al. (2008), primarily due to the small shift in η as reported in Komatsu et al. (2011).

timated abundance of the isobar with mass 7 (^{7}Be+^{7}Li) is more than the observationally determined value by a factor of 2.2 - 4.2 Cyburt et al. (2008), at $\eta_{\rm wmap}$. Relative to the theoretical and observational uncertainties, this represents a deviation of 4.5-5.5 σ.

This significant discrepancy constitutes the "lithium problem" which could point to limitations in either the observations, our theoretical understanding of nucleosynthesis, or the post-BBN processing of lithium.

On the theoretical front, strategies which have emerged to approach the lithium problem broadly either address astrophysics or microphysics. On the astrophysical side, one might attempt to improve our understanding of lithium depletion mechanisms operative in stellar models Korn et al. (2006). This remains an important goal but is not our focus here.

The microphysical solutions to the lithium problem all in some way change the nuclear reactions for lithium production in order to reduce the primordial (or pre-Galactic) lithium abundance to observed levels. Some of these work within the Standard Model, focussing on nuclear physics, in particular the nuclear reactions involved in lithium production. One approach is to attempt to utilize the experimental uncertainties in the rates Coc et al. (2004a); Angulo et al. (2005); Cyburt et al. (2004); Boyd et al. (2010b). A second, related approach is the inclusion of new effects in the nuclear reaction database such as poorly understood resonance effects Cyburt & Pospelov (2012). Finally, it may happen that effects beyond the Standard Model are responsible for the observed lithium abundance. For example, the primordial lithium abundance can be reduced by cosmological variation of the fine structure constant associated with a variation in the deuterium binding energy Coc et al. (2007), or by the post-BBN destruction of lithium through the late decays of a massive particle in the early universe Cyburt et al. (2010).

In this paper, we remain within the Standard Model, examining the possible role of resonant reactions which may have been up to now neglected. The requisite reduction in the ^{7}Li abundance can be achieved by either an enhancement in the rate of destruction of ^{7}Li or its mirror nucleus ^{7}Be. This approach is more promising than the alternative of reducing

the production of ^{7}Be and ^{7}Li where the reactions are better understood experimentally and theoretically Cyburt (2004a); Cyburt & Davids (2008); Ando et al. (2006), whereas the experimental and especially the theoretical situation for $A = 8 - 11$ has made large strides but still allows for surprises at the levels of interest to us Pieper et al. (2002).

The use of resonant channels is an approach that has paid off in the past in the context of stellar nucleosynthesis. Fred Hoyle famously predicted a resonant energy level at 7.68 MeV in the ^{12}C compound nucleus which enhances the $^8\mathrm{Be} + \alpha \rightarrow {}^{12}\mathrm{C}$ reaction cross-section and allows the triple alpha reaction to proceed at relatively low densities Hoyle (1954). Recently, it was shown that there are promising resonant destruction mechanisms which can achieve the desired reduction of the total $A = 7$ isotopic abundance Cyburt & Pospelov (2012). This paper points to a resonant energy level at $(E, J^\pi) = (16.71\ \mathrm{MeV}, 5/2^+)$ in the ^{9}B compound nucleus which can increase the rate of the $^7\mathrm{Be(d,p)}\alpha\alpha$ and/or $^7\mathrm{Be}(d,\gamma)^9\mathrm{B}$ and thereby reduce the ^{7}Be abundance. Here, we take a more general approach and systematically search for all possible compound nuclei Tilley et al. (2004); Ajzenberg-Selove (1990) and potential resonant channels which may result in the destruction of ^{7}Be and/or ^{7}Li.

Because of the large discrepancy between the observed and BBN abundance of ^{7}Li, any nuclear solution to the lithium problem will require a significant modification to the existing rates. As we discuss in the semi-analytical estimate in section 2.2, any new rate or modification to an existing one, must be 2 - 3 times greater than the current dominant destruction channels namely, $^7\mathrm{Li}(p,\alpha)\alpha$ for ^{7}Li and $^7\mathrm{Be}(n,p)^7\mathrm{Li}$ for ^{7}Be. As discussed in Boyd et al. (2010b) and as we show semi-analytically in § 2.2, this is difficult to achieve with non-resonant reactions. Hence, we will concentrate on possible resonant reactions as potential solutions to the lithium problem. As we will show, there are interesting candidate resonant channels which may resolve the ^{7}Li problem. For example, there is a possibility of destroying ^{7}Be through a 1^- or 2^- ^{10}C excited state at approximately 15.0 MeV. The energy range between 6.5 and 16.5 MeV is currently very poorly mapped out and a state near the entrance energy for $^7\mathrm{Be} + {}^3\mathrm{He}$ could provide a solution if the effective width is of order 10

keV. We will also see that these reactions all require fortuitously favorable nuclear parameters, in the form of large channel radii, as also found by Cyburt and Pospelov Cyburt & Pospelov (2012) in the case of $^7\mathrm{Be} + d$. Even so, in the face of the more radical alternative of new fundamental particle physics, these more conventional solutions to the lithium problem beckon for experimental testing.

The paper is organized as follows: First, we lay down the required range of properties of any resonance to solve the lithium problem by means of a semi-analytic estimate inspired by Mukhanov (2004); Esmailzadeh et al. (1991) in § 2.2. Then, in § 2.3, we list experimentally identified resonances from the databases: TUNL [3] and NNDC [4], involving either the destruction of ^{7}Be or ^{7}Li. Finally, the solution space of resonant properties, wherein the lithium problem is partially or completely solved, is mapped for the most promising initial states involving either ^{7}Li or ^{7}Be, by including these rates in a numerical estimation of the ^{7}Li abundance. This exercise will delineate the effectiveness of experimentally studied or identified resonances as well as requirements of possible missed resonant energy levels in compound nuclei formed by these initial states. This is described in § 2.4. We note that in our analysis, the narrow resonance approximation is assumed which may not hold true in certain regions of this solution space. Our key results are pared down to a few resonant reactions described in § 2.5. A summary and conclusions are given in § 2.6.

2.2 Semi-analytical estimate of important reaction rates

Before we embark on a systemic survey of possible resonant enhancements of the destruction of $A = 7$ isotopes, it will be useful to estimate the degree to which the destruction rates must change in order to have an impact on the final ^{7}Li abundance. The net rate of production

[3] *http* : *//www.tunl.duke.edu/nucldata/*
[4] *http* : *//www.nndc.bnl.gov/*

of a nuclide i is given by the difference between the production from nuclides k and l and the destruction rates via nuclide j, i.e. for the reaction $i + j \rightarrow k + l$. This is expressed quantitatively by the rate equation Wagoner et al. (1967b) for abundance change

$$\frac{dn_i}{dt} = -3Hn_i + \sum_{jkl} n_k n_l \langle \sigma v \rangle_{kl} - n_i n_j \langle \sigma v \rangle_{ij}, \tag{2.3}$$

where n_i is the number density of nuclide i, H is the Hubble parameter, $\sum_{ij} n_i n_j \langle \sigma v \rangle_{ij}$ are the sum of contributions from all the forward reactions destroying nuclide i and $\sum_{kl} n_k n_l \langle \sigma v \rangle_{kl}$ are the reverse reactions producing it. $\langle \sigma \mathrm{v} \rangle$ is the thermally averaged cross-section of the reaction. The dilution of the density of these nuclides due to the expansion of the universe can be removed by re-expressing eq. (2.3) in terms of number densities relative to the baryon density $Y_i \equiv n_i / n_\mathrm{b}$, as,

$$\frac{dY_i}{dt} \quad = \quad n_\mathrm{b} \sum_{jkl} Y_k Y_l \langle \sigma v \rangle_{kl} - Y_i Y_j \langle \sigma v \rangle_{ij} \quad . \tag{2.4}$$

Using this general form, the net rate of ^{7}Be production can be approximated in terms of the thermally averaged cross-sections of its most important production and destruction channels as

$$\frac{dY_{^7\mathrm{Be}}}{dt} = n_\mathrm{b} \left(\langle \sigma v \rangle_{^3\mathrm{He}\alpha} Y_{^3\mathrm{He}} Y_\alpha - \langle \sigma v \rangle_{^7\mathrm{Ben}} Y_{^7\mathrm{Be}} Y_n \right) \quad . \tag{2.5}$$

Here, the reverse reaction rates of these production and destruction channels are neglected, as they are much smaller than the forward rates at the lithium synthesis temperature. A similar equation can be written down for ^{7}Li. When quasi-static equilibrium is reached, the destruction and production rates are equal. In this case, approximate values for new rates, which can effectively destroy either isobar, can be obtained analytically.

At temperatures T $\approx$ 0.04 MeV, both ^{7}Li and ^{7}Be are in equilibrium Mukhanov (2004)

which gives,

$$\langle\sigma v\rangle_{^3\mathrm{He}\alpha} Y_{^3\mathrm{He}} Y_\alpha = \langle\sigma v\rangle_{^7\mathrm{Ben}} Y_{^7\mathrm{Be}} Y_n \quad . \tag{2.6}$$

Consider a new, inelastic ^{7}Be destruction channel $^7\mathrm{Be} + X \to Y + Z$, involving projectile X. This reaction will add to the right hand side of eq. (2.6) and shift the equilibrium abundance of ^{7}Be to a new value as follows,

$$Y^{\mathrm{new}}_{^7\mathrm{Be}} \approx \frac{\langle\sigma \mathrm{v}\rangle_{^3\mathrm{He}\alpha} Y_\alpha Y_{^3\mathrm{He}}}{\langle\sigma \mathrm{v}\rangle_{^7\mathrm{Ben}} Y_\mathrm{n} + \langle\sigma v\rangle_{^7\mathrm{BeX}} Y_X} \approx \frac{1}{1 \; + \; \frac{\langle\sigma v\rangle_{^7\mathrm{BeX}} Y_X}{\langle\sigma v\rangle_{^7\mathrm{Ben}} Y_n}} \; Y^{\mathrm{old}}_{^7\mathrm{Be}} \quad . \tag{2.7}$$

If the new reaction is to be important in solving the lithium problem, it must reduce the ^{7}Be abundance by a factor of $Y^{\mathrm{new}}_{^7\mathrm{Be}}/Y^{\mathrm{old}}_{^7\mathrm{Be}} \sim 3 - 4$. This in turn demands via eq. (2.7) that $\langle\sigma v\rangle_{^7\mathrm{BeX}} Y_X / \langle\sigma v\rangle_{^7\mathrm{Ben}} Y_n \sim 2 - 3$, i.e., the rate for the new reaction exceeds that of the usual $n - p$ interconversion reaction rate. A similar estimate can be made for ^{7}Li.

This reasoning would exclude non-resonant rates as they would be required to have unphysically large astrophysical S-factors in the range of order $10^5 - 10^9$ keV - barn depending on the channel. Thus we would expect that only resonant reactions can produce the requisite high rates. Possible resonant reactions are listed in the next section, whose key properties of resonance strength, Γ_{eff} and energy, $\mathrm{E_{res}}$, lie in appropriate ranges capable of achieving the required destruction of mass 7.

Finally, we turn to ^{7}Li destruction reactions, $^7\mathrm{Li} + X \to Y + Z$. Recall that at the WMAP value of η, mass 7 is made predominantly as ^{7}Be, with direct ^{7}Li production about an order of magnitude smaller. This suggests that enhancing direct ^{7}Li destruction will only modestly affect the final mass-7 abundance; we will see that this expectation is largely correct.[5]

With these pointers, the list in the next section is reduced and numerical analysis of the

[5]A subtle point is that normally, the mass-7 abundance is most sensitive to rate $^7\mathrm{Be}(n,p)^7\mathrm{Li}$ Smith et al. (1993). Of course, this reaction leaves the mass-7 abundance unchanged, but the lower Coulomb barrier for ^{7}Li leaves it vulnerable to the $^7\mathrm{Li}(p,\alpha)^4\mathrm{He}$ reaction, which is extremely effective in removing ^{7}Li. Thus, for a new, resonant ^{7}Li destruction reaction to be important, it must successfully compete with the very large $^7\mathrm{Li}(p,\alpha)^4\mathrm{He}$ rate, and even then the mass-7 destruction "bottleneck" remains the $^7\mathrm{Be}(n,p)^7\mathrm{Li}$ rate that limits ^{7}Li appearance. Thus we would not expect direct ^{7}Li destruction to be effective. We will examine ^{7}Li destruction below, and confirm these expectations.

remaining promising rates is done.

2.3 Systematic Search for Resonances

In this section we describe a systematic search for nuclear resonances which could affect primordial lithium production. We first begin with general considerations, then catalog the candidate resonances. We briefly review the basic physics of resonant reactions to establish notation and highlight the key physical ingredients.

2.3.1 General Considerations

Energetically, the net process $^7\mathrm{Be} + A \to B + D$ must have $Q + E_{\rm init} \geq 0$, where the initial kinetic energy $E_{\rm init} \simeq T \lesssim 40$ keV is small at the epoch of $A = 7$ formation. Thus we in practice require exothermic reactions, $Q > 0$. Moreover, inelastic reactions with large Q will yield final state particles with large kinetic energies. Such final states thus have larger phase space than those with small Q and in that sense should be favored.

Consider now a process $^7\mathrm{Be} + X \to C^* \to Y + Z$ which destroys ^{7}Be via a resonant compound state; a similar expression can be written for ^{7}Li destruction. In the entrance channel $^7\mathrm{Be} + X \to C^*$ the energy released in producing the compound state is $Q_C = \Delta(^7\mathrm{Be}) + \Delta(X) - \Delta(C^{\rm g.s.})$, where $\Delta(A) = m - Am_{\rm u}$ is the mass defect. If an excited state C^* in the compound nucleus lies at energy $E_{\rm ex}$, then the difference

$$E_{\rm res} \equiv E_{\rm ex} - Q_C \tag{2.8}$$

determines the effectiveness of the resonance. We can expect resonant production of C^* if $E_{\rm res} \lesssim T$. In an ordinary ("superthreshold") resonance we then have $E_{\rm res} > 0$, while a subthreshold resonance has $E_{\rm res} < 0$.

Once formed, the excited C^* level can decay via some set of channels. The cross section

for $^7\mathrm{Be} + X \to C^* \to Y + Z$ is given by the Breit-Wigner expression

$$\sigma(E) = \frac{\pi\omega}{2\mu E} \frac{\Gamma_{\mathrm{init}}\Gamma_{\mathrm{fin}}}{(E - E_{\mathrm{res}})^2 + (\Gamma_{\mathrm{tot}}/2)^2} \tag{2.9}$$

where E is the center-of-mass kinetic energy in the initial state, μ is the reduced mass and

$$\omega = \frac{2J_{C^*} + 1}{(2J_X + 1)(2J_7 + 1)} \tag{2.10}$$

is a statistical factor accounting for angular momentum. The width of the initial state (entrance channel) is Γ_{init}, and the width of the final state (exit channel) is Γ_{fin}.

One decay channel which must always be available is the entrance channel itself. Obviously such an elastic reaction is useless from our point of view. Rather, we are interested in inelastic reactions in which the initial ^{7}Be (or ^{7}Li) is transformed to something else. In some cases, an inelastic strong decay is possible where the final state particles $Y + Z$ are both nuclei. Note that it is possible to produce a final-state nucleus in an excited state, e.g., $C^* \to Y^* + Z$, in which case the energy release Q'_C is offset by the Y^* excitation energy. This possibility increases the chances of finding energetically allowable final states. Indeed, such a possibility has been suggested in connection with the $^7\mathrm{Be} + d \to {}^9\mathrm{B}^* \to {}^8\mathrm{Be}^* + p$ process Cyburt & Pospelov (2012).

Regardless of the availability of a strong inelastic channel, an electromagnetic transition $C^* \to C^{(*)} + \gamma$ to a lower level is always possible. However, these often have small widths and thus a small branching ratio $\Gamma_{\mathrm{fin}}/\Gamma_{\mathrm{tot}}$. Thus for electromagnetic decays to be important, a strong inelastic decay must not be available, and the rest of the reaction cross section needs to be large to compensate the small branching; as seen in eq. (2.9), this implies that Γ_{init} be large.

Note that in all charged-particle reactions, the Coulomb barrier is crucially important and is implicitly encoded via the usual exponential Gamow factor in the reaction widths of both initial and final charged-particle states. However, if the reaction has a high Q, the final

state kinetic energy will be large and thus there will not be significant final-state Coulomb supression; this again favors final states with large Q. In addition, if the entrance or exit channel has orbital angular momentum $L > 0$, there is additional exponential suppression, so that $L > 0$ states are disfavored for our purposes.

With these requirements in mind, we will systematically search for resonant reactions which could ameliorate or solve the lithium problem. We begin by identifying possible processes which are

1. *new* resonances not yet included in the BBN code;

2. 2-body to 2-body processes, since 3-body rates are generally very small in BBN due to phase space suppression as well as the relatively low particle densities and short timescales;

3. experimentally allowed – in practice this means we seek unidentified states in poorly studied regimes;

4. *narrow* resonances having $\Gamma_{\rm tot} \lesssim T$, which is around $\Gamma_{\rm tot} < 40$ keV but we will also consider somewhat larger widths to be conservatively generous.

5. relatively low-lying resonances with $E_{\rm res} \lesssim few \times T \sim 100 - 300$ keV, which are thermally accessible; here again we err on the side of a generous range.

Once we have identified all possible candidate resonances, we will then assess their viability as solutions to the lithium problem based on available nuclear data.

2.3.2 List of Candidate Resonances

As described above, we will explore the resonant destruction channels of both ^{7}Li and ^{7}Be. Some of the potential resonances which might be able to reduce the mass 7 abundance to the observed value were recently considered in Cyburt & Pospelov (2012). This analysis eliminates several candidate resonances, leaving as genuine solutions only the resonance

related to the ^{7}Be$(d,\gamma)^9$B and ^{7}Be$(d,p)\alpha\alpha$ reactions and associated with the 16.71 MeV level in the ^{9}B compound nucleus. Here, we make an exhaustive list of possible promising resonances that may be important to either ^{7}Be or ^{7}Li destruction channels. In order to do so systematically and account for all possible resonances that may be of importance, we study the energy levels in all possible compound nuclei that may be formed in destroying ^{7}Be or ^{7}Li, making extensive use of databases at TUNL and the NNDC [6].

The available 2-body destruction channels ^7A+X may be classified by $X = n, p, d, t, ^3$He, α, and γ. Consequently, the compound nuclei that can be formed starting from mass 7 have mass numbers ranging from $A = 8$ to $A = 11$, and the ones of particular interest are ^{8}Li, ^{8}Be, ^{8}B, ^{9}Be, ^{9}B, ^{10}Be, ^{10}B, ^{10}C, ^{11}B and ^{11}C. All relevant, resonant energy levels in these compound nuclei that may provide paths for reduction of mass-7 abundance are listed in Tables 2.1 – 2.10.

There are quantum mechanical and kinematic restrictions to our selection of candidates. The candidate resonant reactions must obey selection rules. The partial widths for a channel, which may be viewed as probability currents of emission of the particle in that channel through the nuclear surface, are given as

$$\Gamma_L(E) = 2\ ka\ P_L(E,a)\gamma^2(a) \tag{2.11}$$

where a is the channel radius and E is the projectile energy. Here k is the wavenumber of the colliding particles in the centre-of-mass frame and γ^2 is the reduced width, which depends on the overlap between the wavefunctions inside and outside the nuclear surface, beyond which the nuclear forces are unimportant. The reduced width, γ^2 is independent of energy and has a statistical upper limit called the Wigner limit given by Teichmann & Wigner (1952)

$$\gamma^2 \leq \frac{3\hbar^2}{2\mu a^2}, \tag{2.12}$$

[6] *http://www.tunl.duke.edu/nucldata/*,*http://www.nndc.bnl.gov/*

The pre-factor of $\frac{3}{2}$ is under the assumption that the nucleus is uniform and can change to within a factor of order unity if this assumption changes. The Wigner limit depends sensitively on the channel radius and thus varies with the nuclei involved. For the nuclei of our interest, typical values of γ^2 range from a few hundred keVs to a few MeVs.

In eq. (2.11), $P_L(E, a)$ is the Coulomb penetration probability for angular momentum L and is a strong and somewhat complicated function of E and a. Thus, while the Wigner limit sets a theoretical limit on the reduced width, the upper limit on the full width, $\Gamma_L(E)$, depends on the values of $P_L(E, a)$ and is sensitive to the details of the resonant channel being considered. In light of this complexity, our strategy is as follows. We evaluate the $\Gamma_L(E)$ needed to make a substantial impact on the lithium problem. Then for the cases of highest interest, we will compare our results with the theoretical limit set by the Coulomb suppressed Wigner limit for those specific cases.

We also limit our consideration to two body initial states, with resonance energies $E_{\rm res} \leq$ 650 keV. The high resonance energy limit ensures that all possible resonances which may influence the final ^{7}Li abundance are taken into account, though many of the channels with such high resonance energies will inevitably be eliminated. Excited final states have also been considered in making this list. Different excited states of final state products are marked as separate entries in the table, since each one has its own spin and therefore a different angular momentum barrier. And thereby the significance of each excited state in destroying mass 7 is varied. Also, we usually eliminate the reactions with a negative Q-value except for the $^7{\rm Li}(d,p)^8{\rm Li}$, $^7{\rm Be}(d,^3{\rm He})^6{\rm Li}$, $^7{\rm Be}(d,p)^8{\rm Be}^*$ (16.922 MeV) and $^7{\rm Li}(^3{\rm He},p)^9{\rm Be}^*$ (11.283 MeV) as they are only marginally endothermic.

For a number of the reactions listed in these tables, 1-10, the total spin of the initial state reactants is equal to that of the compound nucleus, which is equal to the total spin of the products, with $L = 0$. However, for many reactions, angular momentum is required in the initial and/or final state, which decreases the penetration probability and thereby the width for that particular channel. In fact for some of these reactions, parity conservation

demands higher angular momentum which worsens this effect. However, we do not reject any channel based on the angular momentum suppression of its width in these tables. Later we will shortlist those resonant channels which are not very suppressed and indeed potentially effective in destroying mass 7.

The reactions of interest are listed in increasing order of the mass of the compound nuclei formed. The particular resonant energy levels of interest $E_{\rm ex}$ and their spins are listed in the table. In general, different initial states involving ^{7}Li and ^{7}Be can form these energy levels and so all these relevant initial states are listed. For each one, the various final product states for an inelastic reaction are enumerated. Again, each of the final state products can also be formed in an excited state. These excited states must have lower energy than the initial state energies for the reaction to be exothermic. In addition spin and parity must be conserved. Enforcing these, the minimum final state angular momenta $L_{\rm fin}$ are evaluated from the spin of the resonant energy level and are listed in the tables. The total widths of the energy levels are listed whenever available. The partial widths of the different channels including the elastic one, out of each energy level are also listed.

We adopt the narrow resonance approximation to evaluate the effect of these resonances and either retain or dismiss them as potential solutions to the lithium problem. Some of the partial widths or limits on them are high enough that they easily qualify to be broad resonances. This implies that the narrow resonance formula used to see their effect is not precise, but still gives a rough idea of whether the resonance is ineffective or not.

Our expression for thermonuclear rates in the narrow resonance approximation is explained in detail in Appendix A.1, and is given by

$$\langle \sigma v \rangle \;\; = \;\; \omega \; \Gamma_{\rm eff} \left(\frac{2\pi}{\mu T} \right)^{3/2} e^{-|E_{\rm res}|/T} \; f\left(2E_{\rm res}/\Gamma_{\rm tot}\right) \tag{2.13}$$

This rate is controlled by two parameters specific to the compound nuclear state: $E_{\rm res}$ and $\Gamma_{\rm eff}$. Here $E_{\rm res}$ is given in eq. (2.8), and measures the offset from the entrance channel and

the compound state. The resonance strength is quantified via

$$\Gamma_{\rm eff} = \frac{\Gamma_{\rm init}\Gamma_{\rm fin}}{\Gamma_{\rm tot}} \tag{2.14}$$

with $\Gamma_{\rm init}$ and $\Gamma_{\rm fin}$ being the entrance and exit widths of a particular reaction, and $\Gamma_{\rm tot}$ the sum of the widths of all possible channels. Of these widths, the smaller of $\Gamma_{\rm init}$ and $\Gamma_{\rm fin}$ along with $\Gamma_{\rm tot}$ are listed in the table above. The resonance strength, $\Gamma_{\rm eff} \approx \Gamma_{\rm init}$, if $\Gamma_{\rm fin}$ dominates the total width, and vice versa. If $\Gamma_{\rm init}$ and $\Gamma_{\rm fin}$ are the dominant partial widths and they are comparable to each other, then the strength is even higher.

As discussed in Appendix A.1, our narrow resonance rate in eq. (2.13) improves on the form of the usual expression for narrow resonance in two ways: (a) it extends to the subthresold domain; and (b) it introduces the factor f which accounts for a finite $E_{\rm res}/\Gamma_{\rm tot}$ ratio.

It is important to make a systematic and comprehensive search for all possible experimentally identified resonances capable of removing this discrepancy. In addition, it is possible that resonances and indeed energy levels themselves were missed, especially at the higher energies, where uncertainties are greater. Therefore it is useful to map the parameter space where the lithium discrepancy is removed to apriori lay down our expectations of such missed resonances. This can be done by looking at interesting initial states involving ^{7}Li and ^{7}Be, and abundant projectiles $p, n, d, t, {}^3$He, α, and parametrizing the effect of inelastic channels on the mass-7 abundance. This is described in § 2.4.

2.4 Narrow resonance solution space

In order to study the effect of resonances in different compound nuclei on the abundance of mass 7, our strategy is to specify the reaction rate for possible resonances, and then run the BBN code to find the mass-7 abundance in the presence of these resonances. In particular, for reactions involving light projectile X, we are interested in considering the general effect

of states ${}^7A+X \to C^*$, including those associated with known energy levels in the compound nucleus, as well as possible overlooked states.

We assume that the narrow resonance approximation holds true at least as a rough guide. If the reaction pathway is specified, i.e., all of the nuclei ${}^7A+X \to C^* \to Y+Z$ are identified, then the reduced mass μ, reverse ratio and the Q-value are uniquely determined. In this case, the thermally averaged cross-section is given by eq. (2.13), with two free parameters: the product $\omega\Gamma_{\rm eff}$ and the resonance energy, $E_{\rm res}$. Because the state C^* is unspecified, so is its spin J_*. On the other hand, we do know the spins of the initial state particles, and thus ω is specified up to a factor $2J_*+1$ (eq. 2.10). For this reason, the $\omega\Gamma_{\rm eff}$ dependence reduces to $(2J_*+1)\Gamma_{\rm eff}$, which we explicitly indicate in all of our plots.

In a few cases we will be interested in one specific final quantum state, e.g., ${}^7{\rm Be}(t,{}^3{\rm He}){}^7{\rm Li}$; when the final state is specified, the reaction can be completely determined, including the effect of the reverse rates. However, in most situations we are interested in the possibility of an overlooked excited state in the compound nucleus, and thus in unknown final states. In this scenario we thus have only a "generic" inelastic exit channel. Consequently, for such plots we cannot evaluate the reverse reaction rate (which is in all interesting cases small) and so we set the reverse ratio to zero.

The resonant rates are included in the BBN code, individually for compound nuclei with an interesting initial state. The plots below show contours of constant, reduced mass-7 abundances. A general feature of all the plots, is the near linear relation between $\log\Gamma_{\rm eff}$ and $E_{\rm res}$ in the region of larger, positive values of $\Gamma_{\rm eff}$ and $E_{\rm res}$. This can seen quantitatively as follows. The thermal rate is integrated over time or equivalently temperature to give the final abundance of mass 7 or ^{7}Li as it exists. Now assuming that the thermal rate operates at an effective temperature, $T_{\rm Li}$, at which ^{7}Li production peaks, a given value for this effective $\langle\sigma v\rangle$ will give a fixed abundance. This implies,

$$\delta Y_7/Y_7 \sim \langle\sigma v\rangle_{\rm peak} \sim \Gamma_{\rm eff}\ e^{-E_{\rm res}/T_{\rm Li}} \sim \ \text{constant} \tag{2.15}$$

This gives a feel for the linear relation in the plot.

2.4.1 A = 8 Compound Nucleus

Compound Nucleus, J^π, E_{ex}	Initial State	L_{init}	L_{fin}	E_{res}	Γ_{tot}	Exit Channels	Exit Channel Width
^{8}Li, 3^+, 2.255 MeV (Included)	$^7\mathrm{Li}+n$	1	1 1	222.71 keV	33 ± 6 keV	γ(ground state) n (elastic) ≈100%	$7.0 \pm 3.0 \times 10^{-2}$ eV 33 ± 6 keV
^{8}Be, 2^+, 16.922 MeV	$^7\mathrm{Li}+p$	1	2 1 2 1	-333.1 keV	74.0 ± 0.4 keV	γ(ground state) γ(3.04 MeV) $\alpha \approx 100\%$ p (elastic)	$8.4 \pm 1.4 \times 10^{-2}$ eV $< 2.80 \pm 0.18$ eV ≈ 74.0 keV unknown
^{8}Be, 1^+, 17.640 MeV	$^7\mathrm{Li}+p$	1	1 1 2 1 1 1	384.9 keV	10.7 keV	γ(ground state) γ(3.04 MeV) γ(3.04 MeV) γ(16.63 MeV) γ(16.92 MeV) p (elastic) 98.8%	16.7 eV 6.7 ± 1.3 eV 0.12 ± 0.05 eV $(3.2 \pm 0.3) \times 10^{-2}$ eV $(1.3 \pm 0.3) \times 10^{-3}$ eV 10.57 keV
^{8}Be, 2^-, 18.91 MeV (Included)	$^7\mathrm{Be}+n$	0	1 1 0 2 0	10.3 keV	122 keV*	γ(16.922 MeV) γ (16.626 MeV) p $p + {}^7\mathrm{Li}^*$ (0.4776 MeV) n (elastic)	$9.9 \pm 4.3 \times 10^{-2}$ eV 0.17 ± 0.07 eV < 105.1 keV* < 105.1 keV* 16.65 keV*
^{8}Be, 3^+, 19.07 MeV (Included)	$^7\mathrm{Be}+n$	1	1 3 1 1	170.3 keV	270 ± 20 keV	p ≈ 100% $p + {}^7\mathrm{Li}^*$ (0.4776 MeV) γ(3.03 MeV) n (elastic)	< 270 keV < 270 keV 10.5 eV unknown
^{8}Be, 3^+, 19.235 MeV (Included)	$^7\mathrm{Be}+n$	1	1 1 1	335.3 keV	227 ± 16 keV	p ≈ 50% γ(3.03 MeV) n (elastic) ≈ 50%	≈ 113.5 keV 10.5 eV ≈ 113.5 keV
^{8}Be, 1^-, 19.40 MeV	$^7\mathrm{Be}+n$	0	0 0 0 1	500.3 keV	645 keV	p $p + {}^7\mathrm{Li}^*$ (0.4776 MeV) n (elastic) α	unknown unknown unknown unknown
$^8\mathrm{B}^{g.s.}$, 2^+, 0 MeV	$^7\mathrm{Be}+p$	1	1 0	-0.1375 MeV	unknown	p (elastic) EC→ ^{8}Be	unknown 8.5×10^{-19} eV
^{8}B, 1^+, 0.7695 MeV (Included)	$^7\mathrm{Be}+p$	1	1 1	630 ±3 keV	35.7 ± 0.6 keV	γ (ground state) p (elastic) 100%	25.2 ± 1.1 meV 35.7 ± 0.6 keV

Table 2.1: This table lists the potential resonances in ^{8}Li, ^{8}Be and ^{8}B which may achieve required destruction of mass 7. These are all allowed by selection rules and includes some resonances already accounted for in determining the current theoretical ^{7}Li abundance indicated as (Included). The entrance and exit channels along with their partial and total widths (Γ_{tot}), minimum angular momenta (L_{init}, L_{fin}) as well as resonance energies are listed wherever experimental data are available. The starred widths are a result of fits from R-matrix analysis. The list includes final products in ground and excited states with the latter marked with a star in the superscript.

As seen in Table 2.1, the only resonance energy level of interest in the ^{8}Li compound nucleus at 2.255 MeV is already accounted for in the $^7\mathrm{Li}+n$ reaction. In the ^{8}Be compound nucleus, there are six levels of relevance for destroying either ^{7}Li or ^{7}Be at 16.922, 17.64, 18.91, 19.07, 19.24 and 19.40 MeV within our limit on E_{res}. The 16.922 MeV level is more

than 300 keV below threshold and has a maximum total width of only 74 keV. Therefore, it is expected to have a weak effect. The 17.64 MeV level has typically low photon widths ($\approx$ 20 eV) and a total width of 10.7 keV. But this state's decay is dominated by the elastic channel which makes this channel uninteresting.

The energy level diagram for ^{8}Be [7](Tilley et al., 2004) shows the initial state, $^7\mathrm{Be} + n$ at an entrance energy of $E = 18.8997$ MeV bringing the 18.91, 19.07, 19.235 and 19.40 MeV levels into play. From among these the effect of the 18.91, 19.07 and 19.235 MeV resonances are already accounted for in the well known $^7\mathrm{Be}(n,p)^7\mathrm{Li}$ reaction Cyburt (2004a). The (18.91 MeV, 2^-), resonance with $L_{\mathrm{init}} = 0$ is the dominant contributor Coc et al. (2004b); Adahchour & Descouvemont (2003). Being a broad resonance with a total width of $\approx$ 122 keV, the Breit-Wigner form is not used and instead an R-matrix fit to the data Cyburt (2004a), is used to evaluate the contribution of the resonant rate. The remaining level at 19.40 should also contribute to this reaction through ground and excited states. Only the 19.40 MeV channel can have an α exit channel due to parity considerations. And this resonance, despite a high resonance energy of $\approx$ 500 keV, can in principle be important due to its large total width of 645 keV, if the proton branching ratio is high.

Figure 2.1 shows the ^{7}Li abundance in the $(\Gamma_{\mathrm{eff}}, E_{\mathrm{res}})$ plane for the $^7\mathrm{Be}(n,p)^7\mathrm{Li}$ reaction. Contours for $^7\mathrm{Li/H} \times 10^{10} = 1.23$, 2.0, 3.0, 4.0, and 5.0 (as labelled) are plotted as functions of the effective width and resonant energy. Below $\approx \ (2J_* + 1)40 = 120$ keV, we expect our results based on the narrow resonance approximation to be quite accurate. As one can see from this figure, to bring the ^{7}Li abundance down close to observed values, one would require a very low resonance energy (of order $\pm$30 keV) with a relatively large effective width. Unfortunately, the 19.40 MeV level of ^{8}Be corresponds to $E_{\mathrm{res}} = 500$ keV as shown by the vertical dashed line and does not make any real impact on the ^{7}Li abundance.

Figure 2.2 shows the effect of a ^{8}B resonance with ^{7}Be and p in the initial state, plotted in the $(\Gamma_{\mathrm{eff}}, E_{\mathrm{res}})$ plane with contours of constant mass 7 abundances. According to Fig. 2.2

[7] $http://www.tunl.duke.edu/nucldata/figures/08figs/08\_04\_2004.gif$.

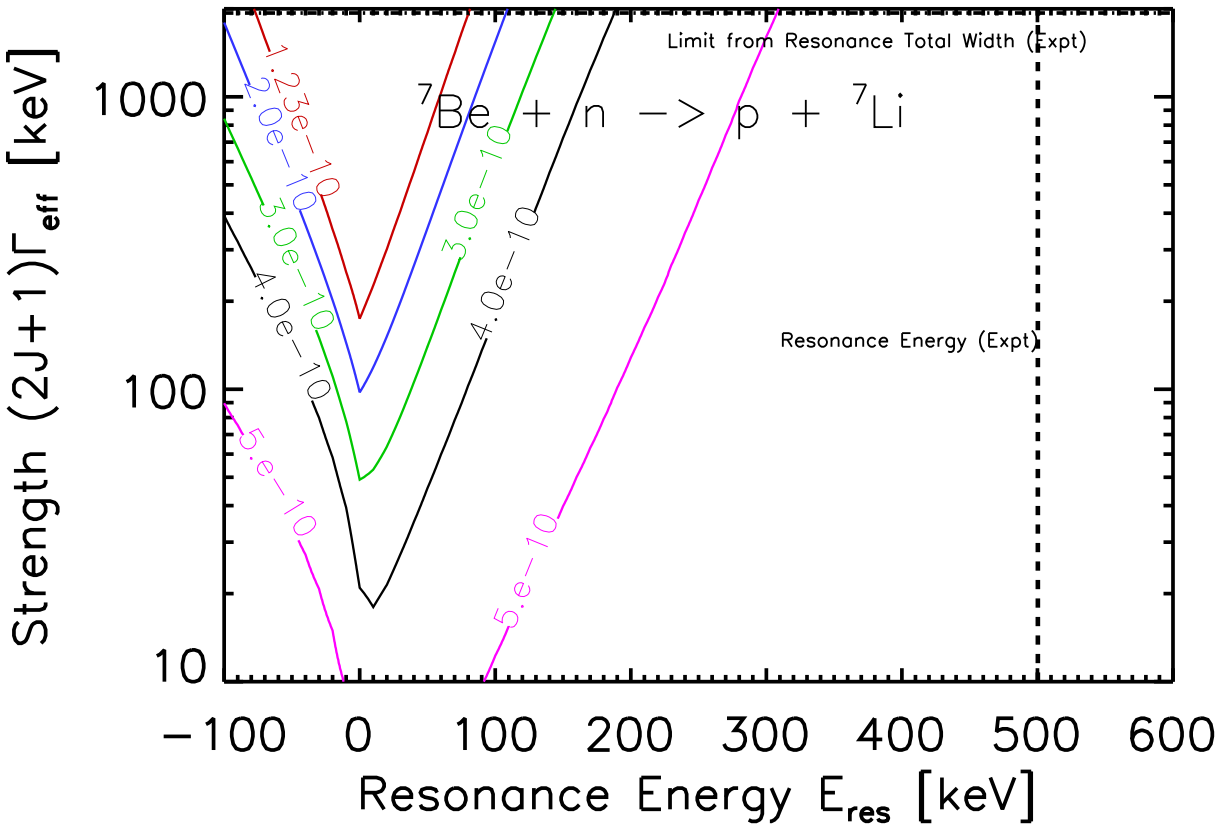

Figure 2.1: The effect of resonances in the ^{8}Be compound nucleus involving initial states ^{7}Be+n. It shows the range of values for the product of the resonant state spin degeneracy and resonance strength, $(2J+1)\Gamma_{\rm eff}$, versus the resonance energy. Contours indicate where the lithium abundance is reduced to ^{7}Li/H $= 1.23\times10^{-10}$ (red), 2.0×10^{-10} (blue), 3.0×10^{-10} (green) 4.0×10^{-10} (black) and 5.0×10^{-10} (magenta). Normal resonances have $E_{\rm res} > 0$, while subthreshold resonances lie in the $E_{\rm res} < 0$. The horizontal dot-dashed black line is the experimental value of the strength of the resonance corresponding to the 19.40 MeV energy level. The vertical dashed black line shows the position of $E_{\rm res}$ for the same state.

for resonance energies of a few 10's of keV's, resonance strength of a few meV is sufficient to attain the observational value of mass 7. However, from the energy level diagram for ^{8}B, [8](Tilley et al., 2004), the closest resonant energy level, $E_{\rm ex}$ is at 0.7695 MeV [9](Tilley et al., 2004), whose effect is already included via the $^7\mathrm{Be}(p,\gamma)^8\mathrm{B}$ reaction. The experimental value of resonance energy is 632 keV which is off the scale in this figure. The only other close energy level to the $^7\mathrm{Be}+p$ entrance channel is at -0.1375 MeV which means that the ground state is a sub-threshold state. This is not the usual resonant reaction, since the ground state doesn't have a width in the sense we refer to a width for the other reactions. But at these energies, the astrophysical S-factor is ≈ 10 eV-barn which is very small and will yield a low cross-section. This too is off scale in the figure and verifies that the $^7\mathrm{Be}(p,\gamma)^8\mathrm{B}$ reaction does not yield an important destruction channel.

2.4.2 A = 9 Compound Nucleus

The energy level diagram for ^{9}Be, [10](Tilley et al., 2004) shows energy levels of interest at 16.671, 16.9752 and 17.298 MeV; these appear in Table 2.2. The $^7\mathrm{Li}+d$ entrance channel sits at 16.6959 MeV. The lowest lying resonant state is at 16.671 MeV and is a sub-threshold state with $E_{\rm res} = -24.9$ keV which lies within the total width of 41 keV. This resonance is thus obviously tantalizing–it is well-tuned energetically and involves an abundant, stable projectile. The ^{7}Li abundance contours for the ^{9}Be resonance states are shown in Fig. 2.3. Perhaps disappointingly, the figure shows that the effect on primordial mass 7 is minor. This illustrates the inability of direct ^{7}Li destruction channels to reduce the mass-7 abundance, as explained in §2.2. Given the overall difficulty of this channel, it is clear that the other possible resonant energy levels (16.9752 MeV and 17.298 MeV) also fail to substantially reduce the mass-7 abundance.

The ^{9}B compound nucleus is relevant for studying the effect of the $^7\mathrm{Be}(d,p)2\alpha$ and its

[8] $http://www.tunl.duke.edu/nucldata/figures/08figs/08_05_2004.gif$.
[9] $http://www.tunl.duke.edu/nucldata/figures/08figs/08_05_2004.gif$.
[10] $http://www.tunl.duke.edu/nucldata/figures/09figs/09_04_2004.gif$.

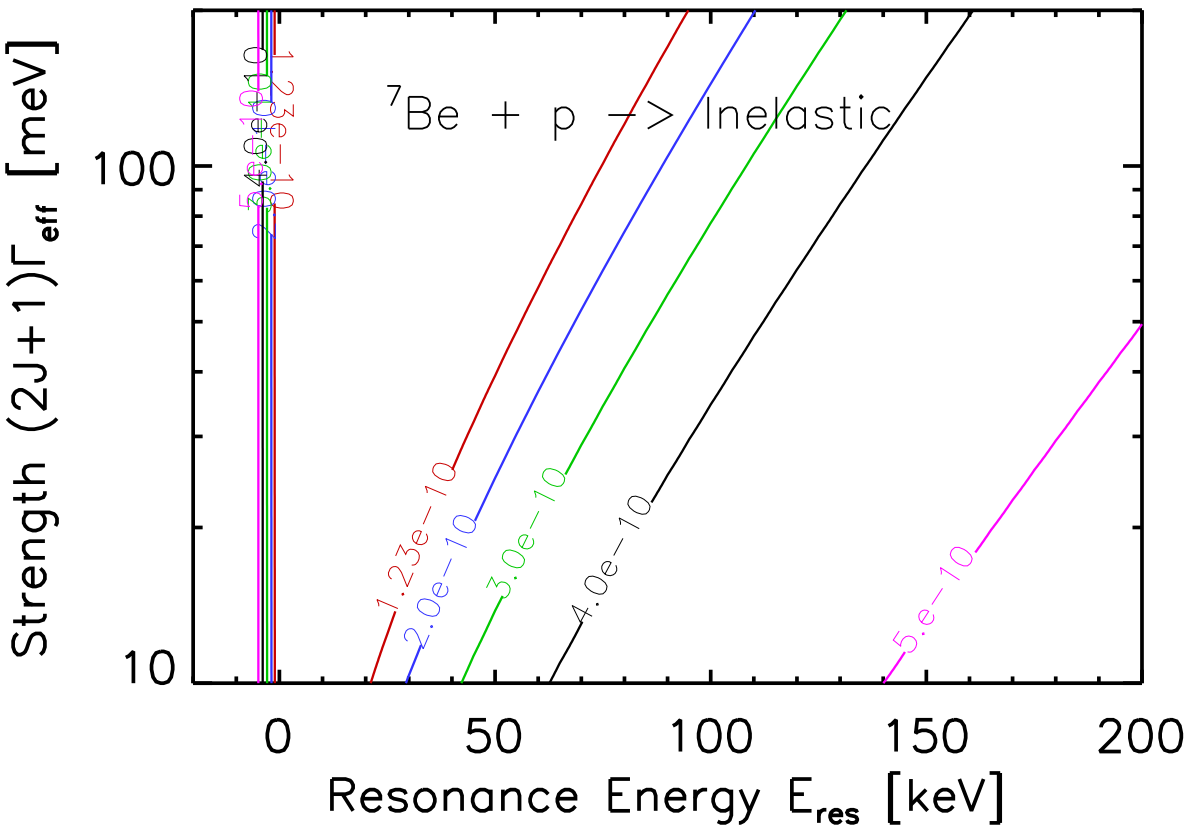

Figure 2.2: As in Fig. 2.1 for the resonances in the ^{8}B compound nucleus involving initial states ^{7}Be+p.

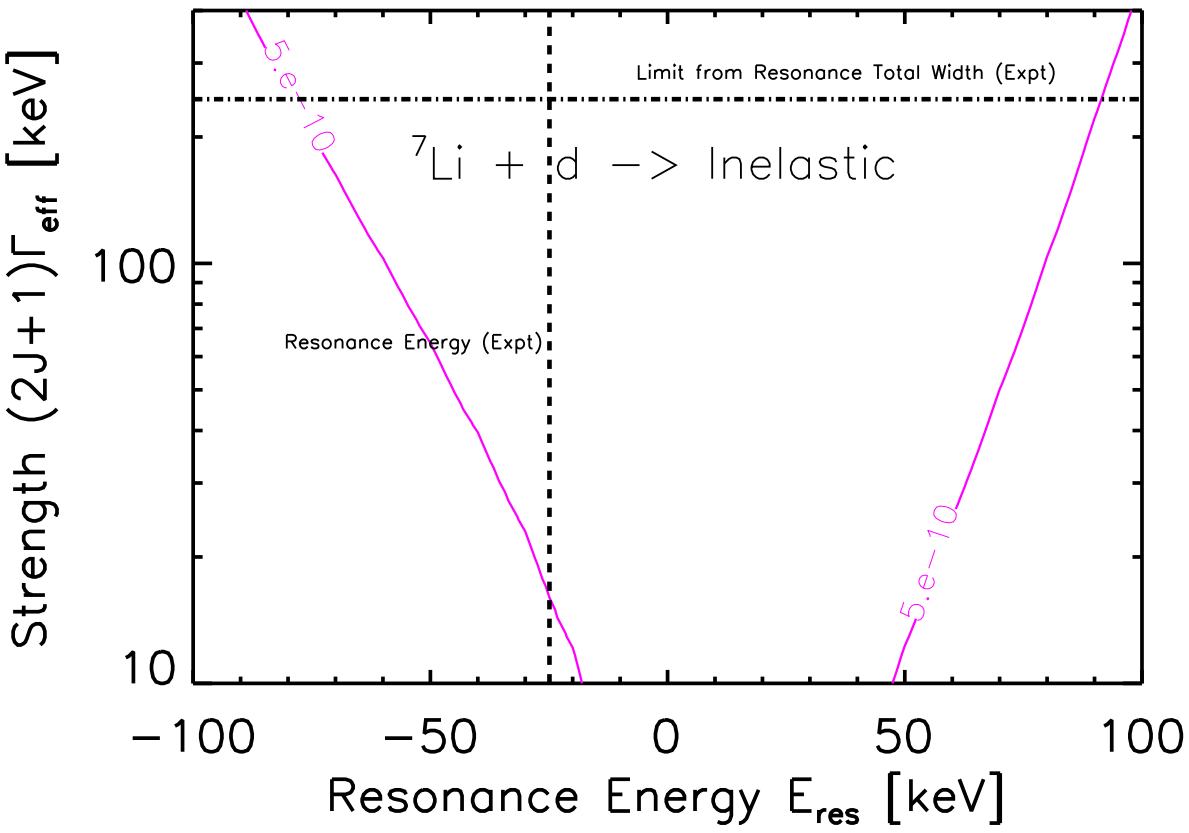

Figure 2.3: As in Fig. 2.1 for the resonances in the ^{9}Be compound nucleus.

Compound Nucleus, J^π, E_{ex}	Initial State	L_{init}	L_{fin}	E_{res}	Γ_{tot}	Exit Channels	Exit Channel Width
^{9}Be, $(5/2^+)$, 16.671 MeV	$^7\mathrm{Li}+d$	1	unknown	-24.9 keV	41 ± 4 keV	γ	unknown
			2			$n+{}^8$Be	unknown
			0			$n+{}^8\mathrm{Be}^*$ (3.03 MeV)	unknown
			2			$n+{}^8\mathrm{Be}^*$ (11.35 MeV)	unknown
			0			p	unknown
			1			α	unknown
			1			d (elastic)	unknown
^{9}Be, $1/2^-$, 16.9752 MeV	$^7\mathrm{Li}+d$	0	1	279.3 keV	389 ± 10 eV	γ (ground state)	16.9 ± 1.0 eV
			1			γ (1.68 MeV)	1.99 ± 0.15 eV
			2			γ (2.43 MeV)	0.56 ± 0.12 eV
			1			γ (2.78 MeV)	2.2 ± 0.7 eV
			unknown			γ (Unknown level TUNL)	< 0.8 eV
			1			γ (4.70 MeV)	2.2 ± 0.3 eV
			1			p	12^{+12}_{-6} eV
			1			n	< 288 eV
			1			$n+{}^8\mathrm{Be}^*$ (3.03 MeV)	< 288 eV
			3			$n+{}^8\mathrm{Be}^*$ (11.35 MeV)	< 288 eV
			2			α	< 241 eV
			0			d (elastic)	62 ± 10 eV
^{9}Be, $(5/2)^-$, 17.298 MeV (Included)	$^7\mathrm{Li}+d$	0	unknown	602.1 keV	200 keV	γ (ground state)	unknown
			1			p	194.4 keV
			3			$n+{}^8$Be	unknown
			1			$n+{}^8\mathrm{Be}^*$ (3.03 MeV)	unknown
			1			$n+{}^8\mathrm{Be}^*$ (11.35 MeV)	unknown
			2			α	unknown
			0			d (elastic)	unknown

Table 2.2: As in Table 2.1 listing the potential resonances in ^{9}Be.

Compound Nucleus, J^π, E_{ex}	Initial State	L_{init}	L_{fin}	E_{res}	Γ_{tot}	Exit Channels	Exit Channel Width
^{9}B, $(5/2^+)$, 16.71 MeV	$^7\mathrm{Be}+d$	1	2	219.9 keV	unknown	$p+{}^8$Be	unknown
			0			$p+{}^8\mathrm{Be}^*$ (3.03 MeV)	unknown
			2			$p+{}^8\mathrm{Be}^*$ (11.35 MeV)	unknown
			0			$p+{}^8\mathrm{Be}^*$ (16.626 MeV)	unknown
			0			$p+{}^8\mathrm{Be}^*$ (16.922 MeV)	unknown
			2			^{3}He	unknown
			1			$\alpha+{}^5$Li	unknown
			3			$\alpha+{}^5\mathrm{Li}^*$ (1.49 MeV)	unknown
			1			d (elastic)	unknown
^{9}B, $(1/2^-)$, 17.076 MeV	$^7\mathrm{Be}+d$	0	1	585.9 keV	22 keV	$p+{}^8$Be	unknown
			1			$p+{}^8\mathrm{Be}^*$ (3.03 MeV)	unknown
			3			$p+{}^8\mathrm{Be}^*$ (11.35 MeV)	unknown
			1			$p+{}^8\mathrm{Be}^*$ (16.626 MeV)	unknown
			1			^{3}He	unknown
			2			$\alpha+{}^5$Li	unknown
			0			$\alpha+{}^5\mathrm{Li}^*$ (1.49 MeV)	unknown
			0			d (elastic)	unknown

Table 2.3: As in Table 2.1 listing the potential resonances in ^{9}B.

competitors such as $^7\mathrm{Be}(d,{}^3\mathrm{He})^6\mathrm{Li}$ and $^7\mathrm{Be}(d,\alpha)^5\mathrm{Li}$. As seen in Table 2.3, the only two levels of interest here are the 16.71 and 17.076 MeV levels. The 16.71 MeV level corresponds to a resonance energy of 220 keV as shown by the vertical dashed line in Fig. 2.4 [11](Tilley et al., 2004). The widths are unknown experimentally. The approximate narrow resonance

[11] $http://www.tunl.duke.edu/nucldata/figures/09figs/09\_05\_2004.gif$.

limit on the resonance width which is shown by the horizontal solid line is around 40 keV. The p exit channel leads to the $^7\mathrm{Be}(d,p)^8\mathrm{Be}^*$ reaction through the excited state at 16.63 MeV in ^{8}Be. This should eventually lead to formation of alpha particles. Fig. 2.4 shows the effect of the 16.71 MeV resonance on the mass-7 abundance as a function of the resonance strength and energy under the narrow resonance approximation. From the plot, we see that the ^{7}Li abundance is reduced by 50% for $(2J+1)\Gamma_{\mathrm{eff}} = 240$ keV. This state has $J = 5/2$ and therefore, a value $\Gamma_{\mathrm{eff}} = 40$ keV or more will have substantial impact on the problem. Furthermore, as $\Gamma_L \geq \Gamma_{\mathrm{eff}}$, we require $\Gamma_L \gtrsim 40$ keV. This result confirms the conclusion of Cyburt & Pospelov (2012). Later in § 2.5 we will see how this compares with theoretical limits. As the decay widths are largely unknown, experimental data on the width are needed.

The state at 17.076 MeV corresponds to a resonant energy of $E_{\mathrm{res}} = 586$ keV and is beyond the scale shown in Fig. 2.4. A solution using this state is very unlikely.

2.4.3 A = 10 Compound Nucleus

Table 2.4 shows that the ^{10}Be compound nucleus has energy levels at 17.12 and 17.79 MeV [12](Tilley et al., 2004) which are close to the initial state $^7\mathrm{Li} + t$ at 17.2509 MeV. The former is far below threshold and does not contribute to ^{7}Li destruction. The 17.79 MeV level is around 540 keV above the entrance energy and its spin and parity are unknown. The total width [13](Tilley et al., 2004) is $\Gamma_{\mathrm{tot}} = 112$ keV which implies a small overlap with the entry channel which renders this resonance insignificant despite having a number of n exit channels with both ground state and excited states of ^{9}Be. As seen in Fig. 2.5, the effect of $^7\mathrm{Li} + t$ is small for the interesting region of parameter space.

The ^{10}B compound nucleus has energy levels at 18.2, 18.43, 18.80 and 19.29 MeV, which we investigate. The 18.2 MeV level is uncertain experimentally [14](Tilley et al., 2004) as indicated in Table 2.5, and hence ideal for parametrizing. There is a ^{3}He entrance channel a

[12] $http://www.tunl.duke.edu/nucldata/figures/10figs/10\_04\_2004.gif$.
[13] $http://www.tunl.duke.edu/nucldata/figures/10figs/10\_04\_2004.gif$.
[14] $http://www.tunl.duke.edu/nucldata/figures/10figs/10\_05\_2004.gif$.

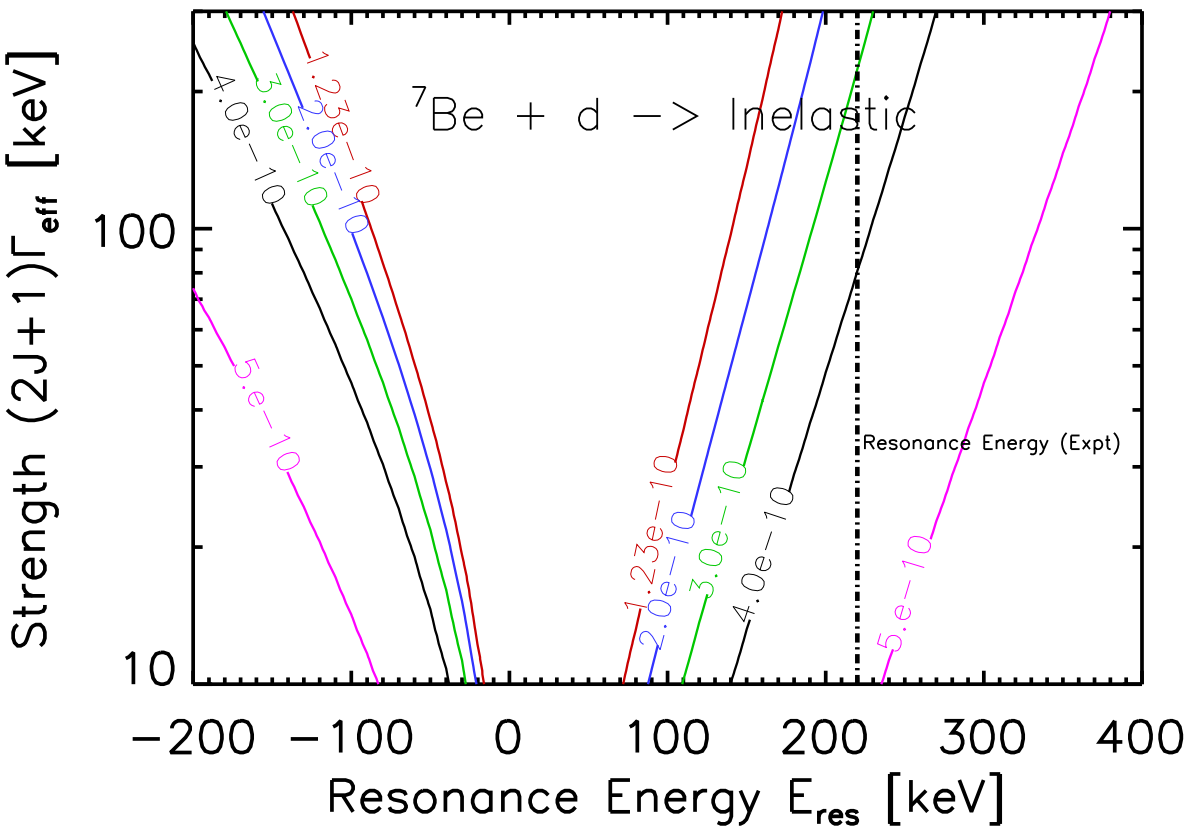

Figure 2.4: As in Fig. 2.1 for the resonances in the ^{9}B compound nucleus. The vertical dashed line at 220 keV indicates the experimental central value of the resonance energy of the 16.71 MeV level.

Compound Nucleus, J^π, E_{ex}	Initial State	L_{init}	L_{fin}	E_{res}	Γ_{tot}	Exit Channels	Exit Channel Width
^{10}Be,	$^7\mathrm{Li} + t$	0	0	-130.9 keV	≈ 150 keV	$n + {}^9\mathrm{Be}$	unknown
(2^-), 17.12 MeV			1			$n + {}^9\mathrm{Be}^*$ (1.684 MeV)	unknown
			0			$n + {}^9\mathrm{Be}^*$ (2.4294 MeV)	unknown
			2			$n + {}^9\mathrm{Be}^*$ (2.78 MeV)	unknown
			1			$n + {}^9\mathrm{Be}^*$ (3.049 MeV)	unknown
			1			$n + {}^9\mathrm{Be}^*$ (4.704 MeV)	unknown
			0			$n + {}^9\mathrm{Be}^*$ (5.59 MeV)	unknown
			2			$n + {}^9\mathrm{Be}^*$ (6.38 MeV)	unknown
			3			$n + {}^9\mathrm{Be}^*$ (6.76 MeV)	unknown
			0			$n + {}^9\mathrm{Be}^*$ (7.94 MeV)	unknown
			0			t (elastic)	unknown
^{10}Be,	$^7\mathrm{Li} + t$	unknown	unknown	539.1 keV	112 ± 35 keV	γ	$3 + 2$ eV
unknown, 17.79 MeV			unknown			$n + {}^9\mathrm{Be}$	< 77 keV
			unknown			$n + {}^9\mathrm{Be}^*$ (1.684 MeV)	< 77 keV
			unknown			$n + {}^9\mathrm{Be}^*$ (2.4294 MeV)	< 77 keV
			unknown			$n + {}^9\mathrm{Be}^*$ (2.78 MeV)	< 77 keV
			unknown			$n + {}^9\mathrm{Be}^*$ (3.049 MeV)	< 77 keV
			unknown			$n + {}^9\mathrm{Be}^*$ (4.704 MeV)	< 77 keV
			unknown			$n + {}^9\mathrm{Be}^*$ (5.59 MeV)	< 77 keV
			unknown			$n + {}^9\mathrm{Be}^*$ (6.38 MeV)	< 77 keV
			unknown			$n + {}^9\mathrm{Be}^*$ (6.76 MeV)	< 77 keV
			unknown			$n + {}^9\mathrm{Be}^*$ (7.94 MeV)	< 77 keV
			unknown			t (elastic)	78 keV

Table 2.4: As in Table 2.1 listing the potential resonant reactions in ^{10}Be.

Compound Nucleus, J^π, E_{ex}	Initial State	L_{init}	L_{fin}	E_{res}	Γ_{tot}	Exit Channels	Exit Channel Width
^{10}B,	$^7\mathrm{Li} + {}^3\mathrm{He}$	unknown	unknown	411.7 keV	1500 ± 300 keV	$p + {}^9\mathrm{Be}$	unknown
unknown, (18.2 MeV)			unknown			$p + {}^9\mathrm{Be}^*$ (1.684 MeV)	unknown
			unknown			$p + {}^9\mathrm{Be}^*$ (2.4294 MeV)	unknown
			unknown			$p + {}^9\mathrm{Be}^*$ (2.78 MeV)	unknown
			unknown			$p + {}^9\mathrm{Be}^*$ (3.049 MeV)	unknown
			unknown			$p + {}^9\mathrm{Be}^*$ (4.704 MeV)	unknown
			unknown			$p + {}^9\mathrm{Be}^*$ (5.59 MeV)	unknown
			unknown			$p + {}^9\mathrm{Be}^*$ (6.38 MeV)	unknown
			unknown			$p + {}^9\mathrm{Be}^*$ (6.76 MeV)	unknown
			unknown			$p + {}^9\mathrm{Be}^*$ (7.94 MeV)	unknown
			unknown			$p + {}^9\mathrm{Be}^*$ (11.283 MeV)	unknown
			unknown			$n + {}^9\mathrm{B}$	unknown
			unknown			$n + {}^9\mathrm{B}^*$ (1.6 MeV)	unknown
			unknown			$n + {}^9\mathrm{B}^*$ (2.361 MeV)	unknown
			unknown			$n + {}^9\mathrm{B}^*$ (2.75 MeV)	unknown
			unknown			$n + {}^9\mathrm{B}^*$ (2.788 MeV)	unknown
			unknown			$n + {}^9\mathrm{B}^*$ (4.3 MeV)	unknown
			unknown			$n + {}^9\mathrm{B}^*$ (6.97 MeV)	unknown
			unknown			$d + {}^8\mathrm{Be}$	unknown
			unknown			$d + {}^8\mathrm{Be}^*$ (3.03 MeV)	unknown
			unknown			$d + {}^8\mathrm{Be}^*$ (11.35 MeV)	unknown
			unknown			t	unknown
			unknown			$\alpha + {}^6\mathrm{Li}$	unknown
			unknown			$\alpha + {}^6\mathrm{Li}^*$ (2.186 MeV)	unknown
			unknown			$\alpha + {}^6\mathrm{Li}^*$ (3.563 MeV)	unknown
			unknown			$\alpha + {}^6\mathrm{Li}^*$ (4.31 MeV)	unknown
			unknown			$\alpha + {}^6\mathrm{Li}^*$ (5.37 MeV)	unknown
			unknown			^{3}He (elastic)	unknown

Table 2.5: As in Table 2.1 listing the ground and excited final states for the 18.2 MeV energy level in ^{10}B.

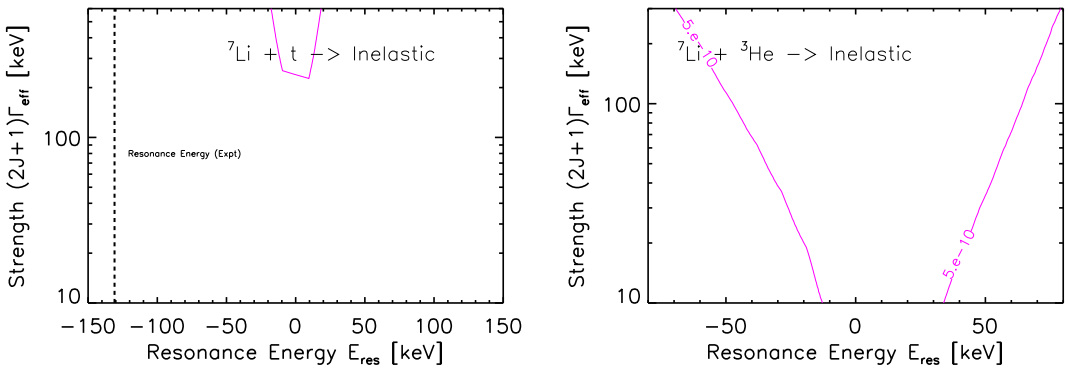

Figure 2.5: As in Fig. 2.1 for the resonances in the ^{10}Be compound nucleus involving the initial state ^{7}Li+t (*left*), and in the ^{10}B compound nucleus involving the initial state ^{7}Li+^{3}He. (*right*).

Compound Nucleus, $J^{\pi}, E_{\rm ex}$	Initial State	$L_{\rm init}$	$L_{\rm fin}$	$E_{\rm res}$	$\Gamma_{\rm tot}$	Exit Channels	Exit Channel Width
^{10}B,	^{7}Li + ^{3}He	0	unknown	641.7 keV	340 keV	γ(ground state)	$\geq$ 3 eV
2^{-}, 18.43 MeV			unknown			γ (4.77 MeV)	$\geq$ 17eV
			0			$n + {}^{9}$B	unknown
			unknown			$n + {}^{9}$B* (1.6 MeV)	unknown
			0			$n + {}^{9}$B* (2.361 MeV)	unknown
			2			$n + {}^{9}$B* (2.75 MeV)	unknown
			1			$n + {}^{9}$B* (2.788 MeV)	unknown
			unknown			$n + {}^{9}$B* (4.3 MeV)	unknown
			2			$n + {}^{9}$B* (6.97 MeV)	unknown
			0			p + ^{9}Be	unknown
			1			$p + {}^{9}$Be* (1.684 MeV)	unknown
			0			$p + {}^{9}$Be* (2.4294 MeV)	unknown
			2			$p + {}^{9}$Be* (2.78 MeV)	unknown
			1			$p + {}^{9}$Be* (3.049 MeV)	unknown
			1			$p + {}^{9}$Be* (4.704 MeV)	unknown
			0			$p + {}^{9}$Be* (5.59 MeV)	unknown
			2			$p + {}^{9}$Be* (6.38 MeV)	unknown
			3			$p + {}^{9}$Be* (6.76 MeV)	unknown
			0			$p + {}^{9}$Be* (7.94 MeV)	unknown
			2			$p + {}^{9}$Be* (11.283 MeV)	unknown
			0			$p + {}^{9}$Be* (11.81 MeV)	unknown
			1			$d + {}^{8}$Be	unknown
			1			$d + {}^{8}$Be* (3.03 MeV)	unknown
			1			$d + {}^{8}$Be* (11.35 MeV)	unknown
			1			$\alpha + {}^{6}$Li	unknown
			1			$\alpha + {}^{6}$Li* (2.186 MeV)	unknown
			1			$\alpha + {}^{6}$Li* (4.31 MeV)	unknown
			1			$\alpha + {}^{6}$Li* (5.37 MeV)	unknown
			1			$\alpha + {}^{6}$Li* (5.65 MeV)	unknown
			0			^{3}He (elastic)	unknown

Table 2.6: As in Table 2.1 listing the ground and excited final state channels for the 18.43 MeV energy level in ^{10}B for the ^{7}Li + ^{3}He initial state.

little over 400 keV below this level. The current total experimental width is 1.5 MeV which is very large and the branching ratios are unknown. The current uncertainty in the $E_{\rm res}$ is 200

Compound Nucleus, J^π, E_{ex}	Initial State	L_{init}	L_{fin}	E_{res}	Γ_{tot}	Exit Channels	Exit Channel Width
^{10}B,	$^7\mathrm{Be}+t$	0	unknown	-239.1 keV	340 keV	γ(ground state)	≥ 3 eV
2^-, 18.43 MeV			unknown			γ (4.77 MeV)	≥ 17 eV
			0			$n+{}^9$B	unknown
			unknown			$n+{}^9\mathrm{B}^*$ (1.6 MeV)	unknown
			0			$n+{}^9\mathrm{B}^*$ (2.361 MeV)	unknown
			2			$n+{}^9\mathrm{B}^*$ (2.75 MeV)	unknown
			1			$n+{}^9\mathrm{B}^*$ (2.788 MeV)	unknown
			unknown			$n+{}^9\mathrm{B}^*$ (4.3 MeV)	unknown
			2			$n+{}^9\mathrm{B}^*$ (6.97 MeV)	unknown
			0			p + ^{9}Be	unknown
			1			$p+{}^9\mathrm{Be}^*$ (1.684 MeV)	unknown
			0			$p+{}^9\mathrm{Be}^*$ (2.4294 MeV)	unknown
			2			$p+{}^9\mathrm{Be}^*$ (2.78 MeV)	unknown
			1			$p+{}^9\mathrm{Be}^*$ (3.049 MeV)	unknown
			1			$p+{}^9\mathrm{Be}^*$ (4.704 MeV)	unknown
			0			$p+{}^9\mathrm{Be}^*$ (5.59 MeV)	unknown
			2			$p+{}^9\mathrm{Be}^*$ (6.38 MeV)	unknown
			3			$p+{}^9\mathrm{Be}^*$ (6.76 MeV)	unknown
			0			$p+{}^9\mathrm{Be}^*$ (7.94 MeV)	unknown
			2			$p+{}^9\mathrm{Be}^*$ (11.283 MeV)	unknown
			0			$p+{}^9\mathrm{Be}^*$ (11.81 MeV)	unknown
			1			$d+{}^8$Be	unknown
			1			$d+{}^8\mathrm{Be}^*$ (3.03 MeV)	unknown
			1			$d+{}^8\mathrm{Be}^*$ (11.35 MeV)	unknown
			1			$\alpha+{}^6$Li	unknown
			1			$\alpha+{}^6\mathrm{Li}^*$ (2.186 MeV)	unknown
			1			$\alpha+{}^6\mathrm{Li}^*$ (4.31 MeV)	unknown
			1			$\alpha+{}^6\mathrm{Li}^*$ (5.37 MeV)	unknown
			1			$\alpha+{}^6\mathrm{Li}^*$ (5.65 MeV)	unknown
			0			t (elastic)	unknown

Table 2.7: As in Table 2.1 listing the ground and excited final state channels for the 18.43 MeV energy level in ^{10}B for the $^7\mathrm{Be}+t$ initial state.

keV. However, according to the plot in Fig. 2.5, even a 200 keV reduction in E_{res} would not be sufficient to cause any appreciable destruction of ^{7}Li as this reaction has negligible effect on the mass-7 abundance. This is another illustration of the fact that reactions involving direct destruction of ^{7}Li are unimportant.

The 18.43 MeV level is better understood Yan et al. (2002) and with a resonance energy of $\sim$ 640 keV for the $^7\mathrm{Li}+{}^3$He initial state (Table 2.6) and a total width of 340 keV has a lower entrance probability and therefore is likely to be ineffective. This is evident from Fig. 2.5. This level is also a sub-threshold resonance for the $^7\mathrm{Be}+t$ state (Table 2.7), with resonance energy, $E_{res} = -239.1$ keV. This is far below threshold rendering it ineffective.

Staying with $^7\mathrm{Be}+t$, the closest energy level above the entrance energy of 18.669 MeV is the 18.80 MeV (2^+) level (Table 2.8), which corresponds to a resonance energy of $\approx$ 130 keV

Compound Nucleus, J^π, E_{ex}	Initial State	L_{init}	L_{fin}	E_{res}	Γ_{tot}	Exit Channels	Exit Channel Width
^{10}B,	$^7\mathrm{Be}+t$	1	unknown	130.9 keV	<600 keV	γ (0.72 MeV)	≥ 20 eV
2^+, 18.80 MeV			unknown			γ (3.59 MeV)	≥ 20 eV
			1			$n+{}^9$B	unknown
			unknown			$n+{}^9\mathrm{B}^*$ (1.6 MeV)	unknown
			1			$n+{}^9\mathrm{B}^*$ (2.361 MeV)	unknown
			1			$n+{}^9\mathrm{B}^*$ (2.75 MeV)	unknown
			0			$n+{}^9\mathrm{B}^*$ (2.788 MeV)	unknown
			unknown			$n+{}^9\mathrm{B}^*$ (4.3 MeV)	unknown
			1			$n+{}^9\mathrm{B}^*$ (6.97 MeV)	unknown
			1			$p+{}^9$Be	unknown
			2			$p+{}^9\mathrm{Be}^*$ (1.684 MeV)	unknown
			1			$p+{}^9\mathrm{Be}^*$ (2.4294 MeV)	unknown
			1			$p+{}^9\mathrm{Be}^*$ (2.78 MeV)	unknown
			0			$p+{}^9\mathrm{Be}^*$ (3.049 MeV)	unknown
			0			$p+{}^9\mathrm{Be}^*$ (4.704 MeV)	unknown
			1			$p+{}^9\mathrm{Be}^*$ (5.59 MeV)	unknown
			1			$p+{}^9\mathrm{Be}^*$ (6.38 MeV)	unknown
			2			$p+{}^9\mathrm{Be}^*$ (6.76 MeV)	unknown
			1			$p+{}^9\mathrm{Be}^*$ (7.94 MeV)	unknown
			1			$p+{}^9\mathrm{Be}^*$ (11.283 MeV)	unknown
			1			$p+{}^9\mathrm{Be}^*$ (11.81 MeV)	unknown
			2			$d+{}^8$Be	unknown
			0			$d+{}^8\mathrm{Be}^*$ (3.03 MeV)	unknown
			2			$d+{}^8\mathrm{Be}^*$ (11.35 MeV)	unknown
			1			$^3\mathrm{He}+{}^7$Li	unknown
			1			$^3\mathrm{He}+{}^7\mathrm{Li}^*$(0.47761 MeV)	unknown
			2			$\alpha+{}^6$Li	unknown
			2			$\alpha+{}^6\mathrm{Li}^*$ (2.186 MeV)	unknown
			2			$\alpha+{}^6\mathrm{Li}^*$ (3.56 MeV)	unknown
			0			$\alpha+{}^6\mathrm{Li}^*$ (4.31 MeV)	unknown
			0			$\alpha+{}^6\mathrm{Li}^*$ (5.37 MeV)	unknown
			2			$\alpha+{}^6\mathrm{Li}^*$ (5.65 MeV)	unknown
			1			t (elastic)	unknown

Table 2.8: As in Table 2.1 listing the ground and excited final state channels for the 18.80 MeV energy level in ^{10}B for the $^7\mathrm{Be}+t$ initial state.

[15](Tilley et al., 2004). The exit channel widths for p and ^{3}He are unknown experimentally and thus, this is a candidate for parametrization. There is a weak upper limit on $\Gamma_{tot} < 600$ keV [16](Tilley et al., 2004), which for $J_* = 2$ is off scale in Figs. 2.6 and 2.7. The contour plot in Fig. 2.6 show that for a central value of resonance energy of ≈ 130 keV shown by the vertical dashed line, resonance strength of just under 1 MeV is required which is very high. Also, parity requirements force $L = 1$, which will cause suppression of this channel. We note that there is no quoted uncertainty for this energy level and neighboring levels have typical uncertainties of 100-200 keV. Therefore it may be possible (within 1-2σ) that the state lies at an energy of 100 keV lower and would energetically, have a chance at solving the ^{7}Li

[15] $http://www.tunl.duke.edu/nucldata/figures/10figs/10\_05\_2004.gif$.
[16] $http://www.tunl.duke.edu/nucldata/figures/10figs/10\_05\_2004.gif$.

Compound Nucleus, J^π, E_{ex}	Initial State	L_{init}	L_{fin}	E_{res}	Γ_{tot}	Exit Channels	Exit Channel Width
^{10}B, 2^-, 19.29 MeV	$^7\mathrm{Be}+t$	0	unknown	620.9 keV	190 ± 20 keV	γ	unknown
			0			$n + {}^9\mathrm{B}$	unknown
			unknown			$n + {}^9\mathrm{B}^*$ (1.6 MeV)	unknown
			0			$n + {}^9\mathrm{B}^*$ (2.361 MeV)	unknown
			2			$n + {}^9\mathrm{B}^*$ (2.75 MeV)	unknown
			1			$n + {}^9\mathrm{B}^*$ (2.788 MeV)	unknown
			unknown			$n + {}^9\mathrm{B}^*$ (4.3 MeV)	unknown
			0			p + ^{9}Be	unknown
			1			$p + {}^9\mathrm{Be}^*$ (1.684 MeV)	unknown
			0			$p + {}^9\mathrm{Be}^*$ (2.4294 MeV)	unknown
			2			$p + {}^9\mathrm{Be}^*$ (2.78 MeV)	unknown
			1			$p + {}^9\mathrm{Be}^*$ (3.049 MeV)	unknown
			1			$p + {}^9\mathrm{Be}^*$ (4.704 MeV)	unknown
			0			$p + {}^9\mathrm{Be}^*$ (5.59 MeV)	unknown
			2			$p + {}^9\mathrm{Be}^*$ (6.38 MeV)	unknown
			3			$p + {}^9\mathrm{Be}^*$ (6.76 MeV)	unknown
			0			$p + {}^9\mathrm{Be}^*$ (7.94 MeV)	unknown
			2			$p + {}^9\mathrm{Be}^*$ (11.283 MeV)	unknown
			0			$p + {}^9\mathrm{Be}^*$ (11.81 MeV)	unknown
			1			$d + {}^8\mathrm{Be}$	unknown
			1			$d + {}^8\mathrm{Be}^*$ (3.03 MeV)	unknown
			3			$d + {}^8\mathrm{Be}^*$ (11.35 MeV)	unknown
			0			^{3}He	unknown
			1			$\alpha + {}^6\mathrm{Li}$	unknown
			1			$\alpha + {}^6\mathrm{Li}^*$ (2.186 MeV)	unknown
			1			$\alpha + {}^6\mathrm{Li}^*$ (4.31 MeV)	unknown
			1			$\alpha + {}^6\mathrm{Li}^*$ (5.37 MeV)	unknown
			1			$\alpha + {}^6\mathrm{Li}^*$ (5.65 MeV)	unknown
			0			t (elastic)	unknown

Table 2.9: As in Table 2.1 listing the ground and excited final state channels for the 19.29 MeV energy level in ^{10}B for the $^7\mathrm{Be} + t$ initial state.

problem. This is true for the p exit channel.

The ^{3}He exit channel may also reduce mass 7, through the formation of the ^{7}Li which is much easier to destroy. This is reflected in Fig. 2.7, which shows that at resonance energies of ≤ 100 keV, a strength of a few 100 keV, but less than 600 keV may be sufficient to achieve comparable destruction of ^{7}Be as the 16.71 MeV resonance. The caveat is that for such values of strengths, the narrow resonance approximation does not hold true and this may lead to a reduced effect. Nevertheless, this is yet another case deserving a detailed comparison with the theoretical limits which will follow in § 2.5. Once again, definitive conclusions can be drawn only based on experimental data.

The 19.29 MeV level (Table 2.9) is energetically harder to access and with a total width of only 190 keV, it is unlikely to be of significance, despite being less studied.

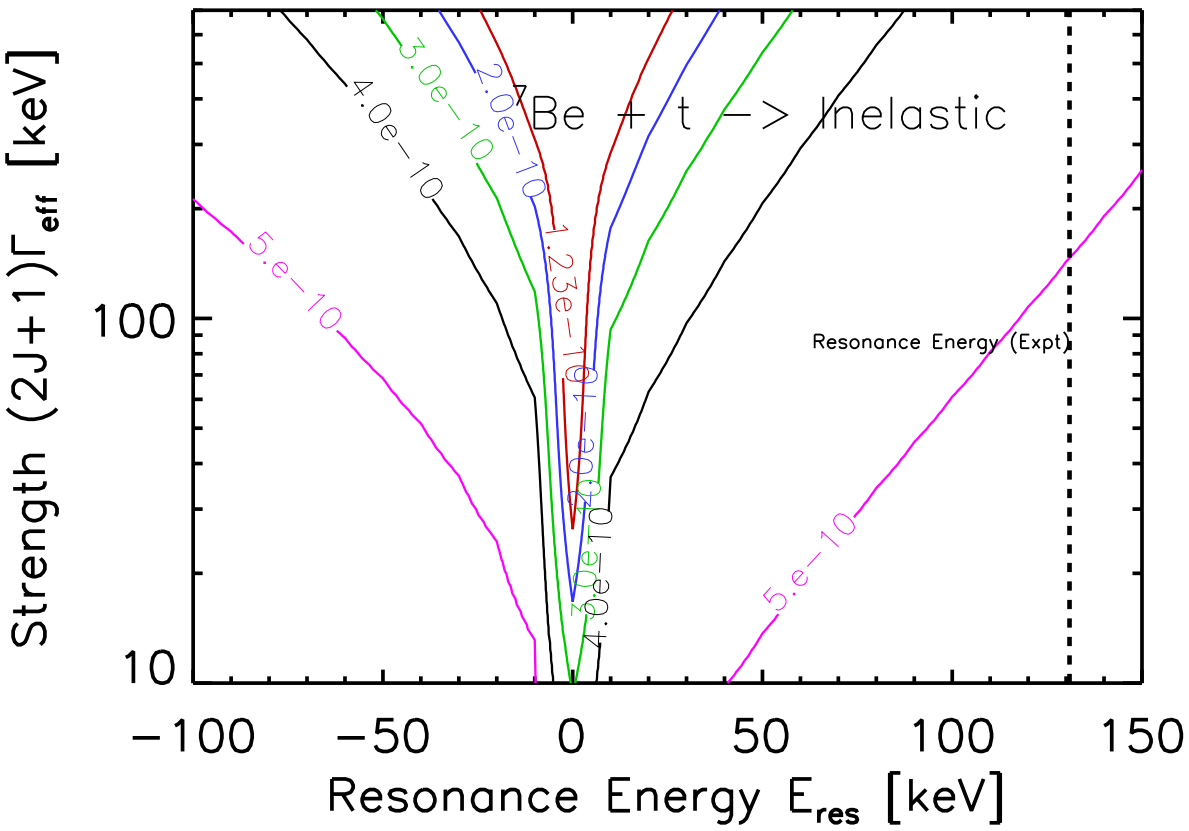

Figure 2.6: As in Fig. 2.1 for the resonances in the ^{10}B compound nucleus involving initial states ^{7}Be+t.

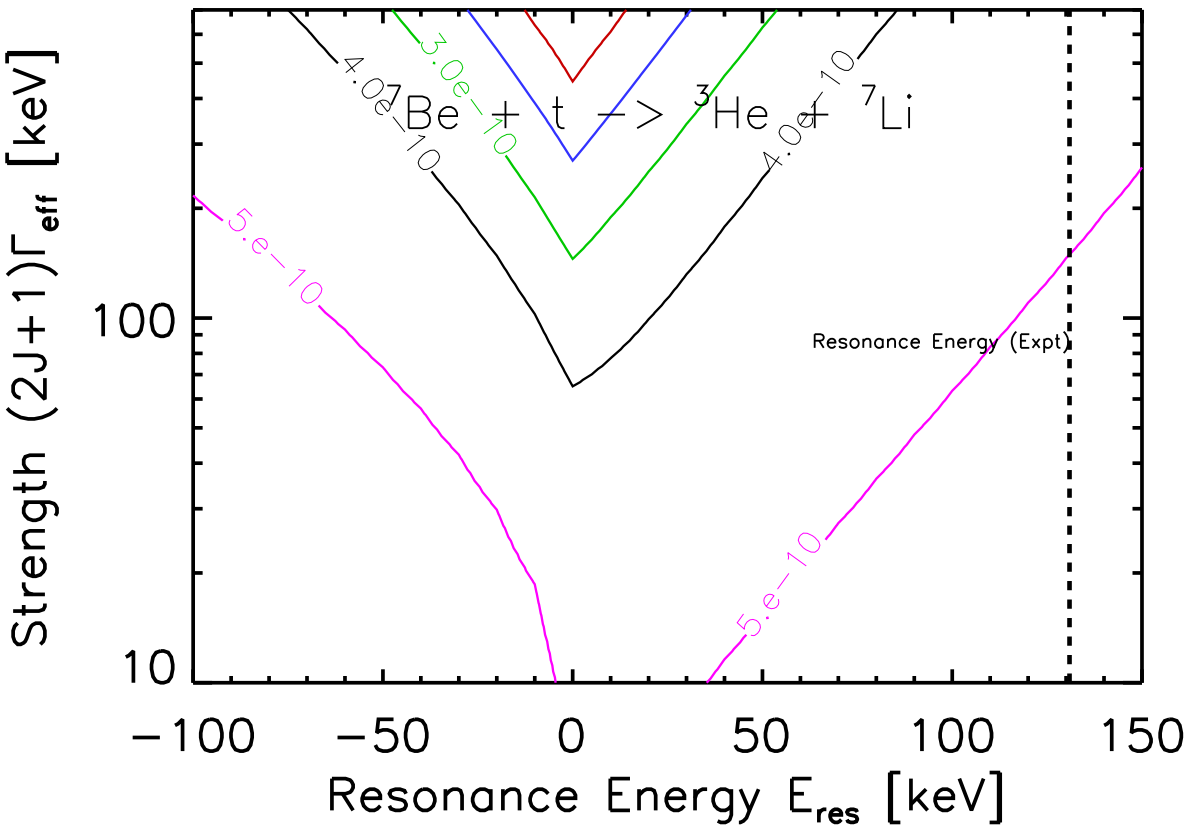

Figure 2.7: As in Fig. 2.1 for the resonances in the reaction ^{7}Be(t,^{3}He)^{7}Li.

Compound Nucleus, J^π, E_{ex}	Initial State	L_{init}	L_{fin}	E_{res}	Γ_{tot}	Exit Channels	Exit Channel Width
^{10}C, unknown	^{7}Be + ^{3}He	unknown	unknown unknown	unknown ($Q = 15.003$ MeV)	unknown	p α ^{3}He (elastic)	unknown unknown unknown
^{11}B, $(3/2^-)$, 8.56 MeV	^{7}Li + α	0	1 1 1 1 1	-103.7 keV	1.346 eV	γ (ground state) γ (2.125 MeV) γ (4.445 MeV) γ (5.020 MeV) α (elastic)	0.53 ± 0.05 eV 0.28 ± 0.03 eV $(4.7 \pm 1.1) \times 10^{-2}$ eV $(8.5 \pm 1.2) \times 10^{-2}$ eV Unknown
^{11}B, $(5/2^-)$, 8.92 MeV (Included)	^{7}Li + α	2	1 2 1 1	256.3 keV	4.37 ± 0.02 eV	γ (ground state) γ (ground state) γ (4.445 MeV) α (elastic)	4.10 ± 0.20 eV $(5.0 \pm 3.6) \times 10^{-2}$ eV 0.22 ± 0.02 eV Unknown
^{11}B, $7/2^+$, 9.19 MeV	^{7}Li + α	3	1 2 0 1	526.3 keV	$1.9^{+1.5}_{-1.1}$ eV	γ (ground state) γ (4.445 MeV) γ (6.743 MeV) α (elastic)	$(2.7 \pm 1.2) \times 10^{-3}$eV 0.25 ± 0.09 eV $(3.8 \pm 1.3) \times 10^{-2}$ eV Unknown
^{11}B, $5/2^+$, 9.271 MeV	^{7}Li + α	1	1 0 0 1 1	606.3 keV	4 keV	γ (ground state) γ (4.445 MeV) γ (6.743 MeV) γ (6.792 MeV) α (elastic)	0.212 eV 0.802 eV 0.137 eV < 0.007 eV ≈ 4 keV
^{11}C, $3/2^+$, 7.4997 MeV	^{7}Be + α	1	1 0 1	-43.3 keV	0.0105 eV	γ (ground state) γ (2.0 MeV) α(elastic)	Unknown Unknown Unknown
^{11}C, $(3/2^-)$, 8.10 MeV	^{7}Be + α	0	1 1 0	557 keV	11 ± 7 eV	γ (ground state) γ (2.0 MeV) α(elastic)	0.26 ± 0.06 eV $(9.1 \pm 2.3) \times 10^{-2}$ eV Unknown

Table 2.10: As in Table 2.1 listing resonances in ^{10}C, ^{11}B and ^{11}C.

The ^{10}C nucleus [17](Ajzenberg-Selove, 1990) appearing in Table 2.10 shows large uncertainties and experimental gaps at higher energy levels which may be relevant to entrance channels involving ^{7}Be. Reactions involving the $^7\mathrm{Be} + {}^3\mathrm{He}$ initial state could contribute in destroying ^{7}Be if there exists a resonance in the parameter space shown in the Fig. 2.8. These reactions win over those involving the $^7\mathrm{Be} + t$ state, because ^{3}He is substantially more abundant than t, but are worse off due to a higher Coulomb barrier. The entrance energy for ^{7}Be + ^{3}He is 15.0 MeV. As one can see from the figure, a 1^- or 2^- state with a resonance energy of either -10 keV or 40 keV corresponding to energy levels of 14.99 and 15.04 MeV respectively with a strength as high as a few 10's of keVs is what it will take to solve the lithium problem with this initial state. Thus, any ^{10}C resonance near these energies which may have been missed by experiment may be interesting as a solution to the lithium problem; we return to this issue in more detail in § 2.5.

[17] $http://www.tunl.duke.edu/nucldata/figures/11figs/11\_06\_1990.gif$.

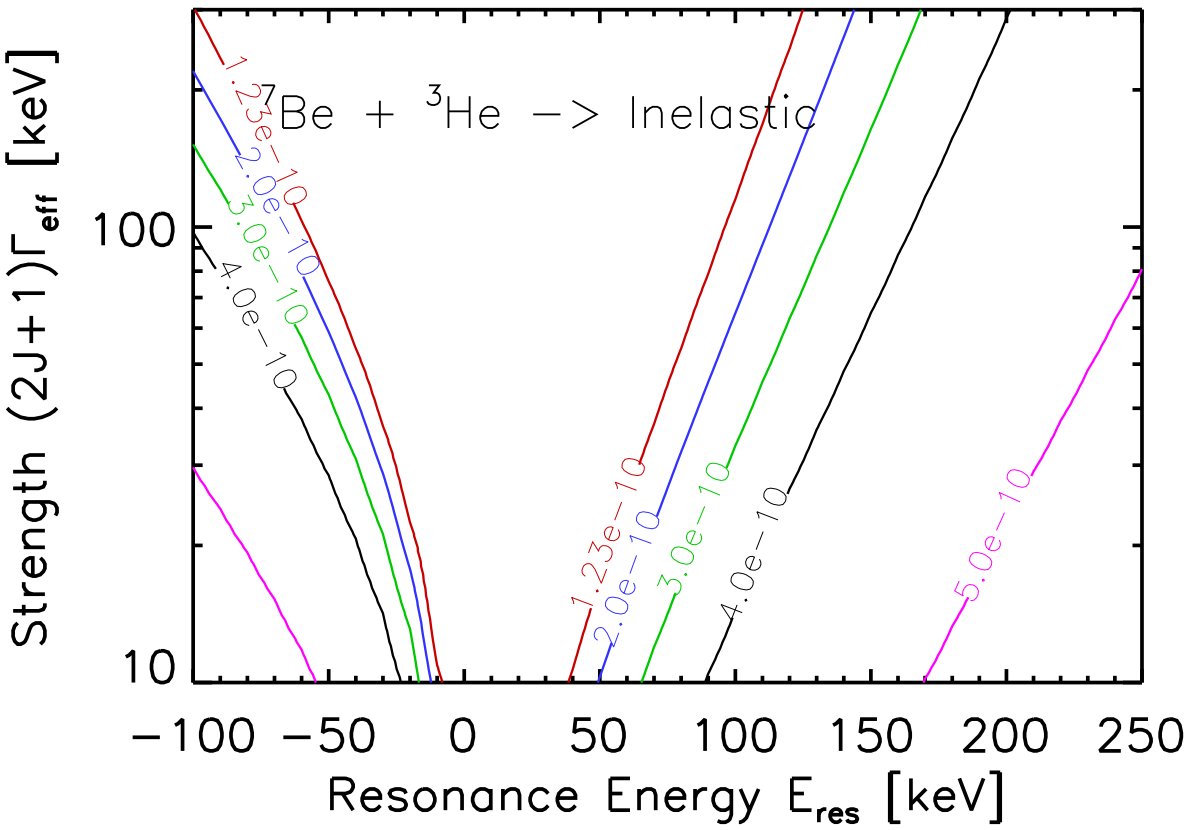

Figure 2.8: As in Fig. 2.1 for the resonances in ^{10}C involving initial state ^{7}Be + ^{3}He

2.4.4 A = 11 Compound Nucleus

For ^{11}B [18](Ajzenberg-Selove, 1990), Table 2.10 shows that the entrance channel, ^{7}Li+α is at 8.6637 MeV which is 103.7 keV above the resonant energy level at 8.560 MeV and $\approx$ 260 keV below the resonant energy level at 8.92 MeV. Parity demands angular momentum to be 0. Both states are at relatively large $|E_{\rm res}|$ and are not capable of making a sizable impact on the ^{7}Li abundance. Table 2.10 further lists states 9.19 MeV (which requires $L = 3$ and has a total width of < 2 eV) and 9.271 MeV (whose decay is dominated by the elastic channel)

[18] *http* : *//www.tunl.duke.edu/nucldata/figures/*11*figs/*11_05_1990.*gif*.

which have progressively larger resonant energies and are unlikely to provide a solution.

For ^{11}C [19](Ajzenberg-Selove, 1990), the entrance channel, ^{7}Be$+\alpha$ is at 7.543 MeV which is 43 keV above the resonant energy level at 8.560 MeV and 557 keV below the resonant energy level at 8.10 MeV.

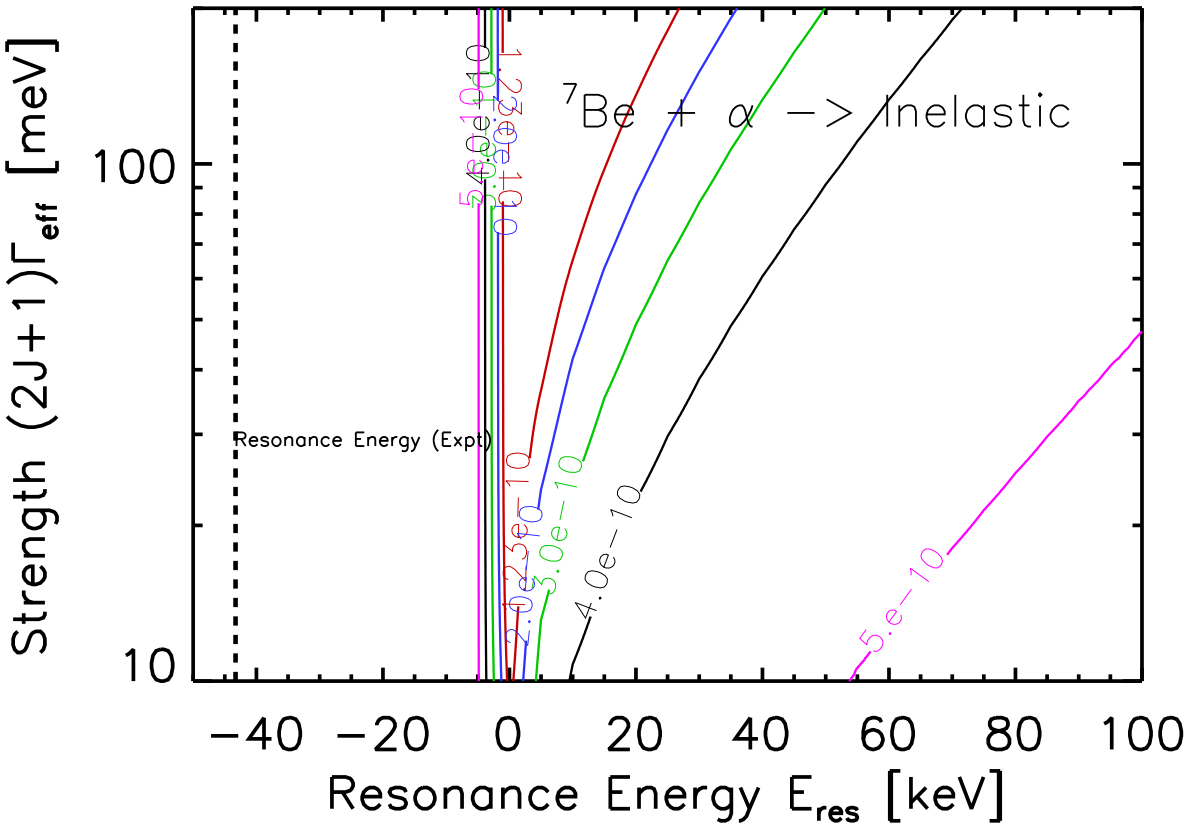

Figure 2.9: As in Fig. 2.1 for the resonances in ^{11}C involving initial states ^{7}Be+α.

As seen in Fig. 2.9, we find that the sub-threshold resonance in the ^{11}C nucleus, produces a very insignificant effect on ^{7}Be in agreement with the claim in Cyburt & Pospelov (2012). The super-threshold resonance states are also too far away at resonance energies, 557 keV

[19] $http://www.tunl.duke.edu/nucldata/figures/11figs/11\_06\_1990.gif$.

and 260 keV for $^7\mathrm{Be}(\alpha,\gamma)^{11}\mathrm{C}$ and $^7\mathrm{Li}(\alpha,\gamma)^{11}\mathrm{B}$ respectively.

However, Fig. 2.9 shows that the presence of a (missed) resonance at resonance energies of few tens of keV 's, requires a very meagre strength of the order of tens of meV 's to destroy mass 7 substantially. Strengths of this order are typical of electromagnetic channels. It is difficult to assess the probability that a ^{11}C state at 7.55 MeV has been overlooked.

2.5 Reduced List of Candidate Resonances

Having systematically identified all possible known resonant energy levels which could affect BBN, we find most of these levels are ruled out immediately as promising solutions, based on their measured locations, strengths, and widths. As expected, the existing electromagnetic channels are too weak to cause significant depletion of lithium owing to their small widths.

From amongst the various hadronic channels listed in the tables above, we have seen that all channels are unimportant except three which are summarized in table 7.1. The $^7\mathrm{Be}+d$ channels involving the 16.71 MeV resonance in ^{9}B, the $^7\mathrm{Be}+t$ channels involving the 18.80 MeV resonance in ^{10}B and $^7\mathrm{Be}+{}^3\mathrm{He}$ channels. These are ones where a more detailed theoretical calculation of widths is required to decide whether they may be important or not. For each reaction, the Wigner limit, eq. (2.12), to the reduced width γ^2 imposes a bound on Γ_L via eq. (2.11). Specifically, the penetration factor, $P_L(E,a)$, must be estimated to see if the required strengths according to Figs. 2.4, 2.6 2.7, and 2.8 to solve the problem are at all attainable. The penetration factor is given by

$$P_L(E,a) = \frac{1}{G_L^2(E,a) + F_L^2(E,a)} \tag{2.16}$$

where $G_L(E,a)$ and $F_L(E,a)$ are Coulomb wavefunctions.

We note that the Coulomb barrier penetration factor decreases as the energy of the projectile and/or the channel radius, a, increases. For a narrow resonance, the relevant projectile energy is $E \approx E_{\mathrm{res}}$, which is set by nuclear experiments (where available) and

their uncertainties. The channel radius corresponds to the boundary between the compound nucleus in the resonant state and the outgoing / incoming particles. Therefore, the channel radius depends on the properties of the compound state and the particles into which it decays.

Consider the case of ^{7}Be$+d$, which has resonance energy, $E_{\rm res} = 220 \pm 100$ keV and initial angular momentum, $L_{init} = 1$. A naive choice for the channel radius is the "hard-sphere" approximation,

$$a_{12} = 1.45\ (A_1^{1/3} + A_2^{1/3}) \text{fm} \tag{2.17}$$

which gives $a_{27} = 4.6$ fm. Using the Coulomb functions, Γ_1 is of order a few keVs. The corresponding strength, $\Gamma_{\rm eff}$ should be essentially the same and we further gain a factor of 6 from the spin of this state. This suggests by using figure 2.4, that this resonance should fall short of the width required to solve or even ameliorate the problem.

However, reactions involving light nuclides including $A = 7$ are found to have channel radii exceed the hard-sphere approximation Cyburt & Pospelov (2012). We thus consider larger radii and find that for values higher than around 10 fm, we get a width which has the potential to change the ^{7}Li abundance noticeably. The Wigner limit

$$a^2 = \frac{3\hbar^2}{2\ \mu\ E_{\rm res}} \tag{2.18}$$

gives a larger radius, $a_{27} = 13.5$ fm, which gives one a better chance of solving the problem. This is consistent with the conclusions drawn by Cyburt & Pospelov (2012).

For the $^7\text{Be} + t$ initial state, the 18.80 MeV state of ^{10}B has a resonance energy $E = 0.131$ MeV and $L_{init} = 1$. There is no experimental error bar on the resonance energy. The hard sphere approximation gives $a_{37} = 4.9$ fm. This gives a width, Γ_1, which is less than a tenth of a keV, and is orders of magnitude lower than what is needed. In the spirit of what we did in the earlier case, using eq. (2.18) gives a channel radius, $a_{37} = 15$ fm improving

the situation by almost 2 orders of magnitude in Γ_1. If, in addition to increasing a_{37}, the resonance energy were to be higher by 100 keV, then Γ_1 could be large enough to change the ^{7}Li abundance noticeably.

The $^7\mathrm{Be}+^3\mathrm{He}$ initial state will have ^{10}C as the compound state. The structure of the ^{10}C nucleus is not well studied experimentally [20](Ajzenberg-Selove, 1990) nor theoretically. In particular, we are unaware of any published data on ^{10}C states near the $^7\mathrm{Be}+^3\mathrm{He}$ entrance energy, i.e., states at or near $E_{\mathrm{ex}}(^{10}\mathrm{C}) \approx Q(^7\mathrm{Be}+^3\mathrm{He}) = 15.003$ MeV. To our knowledge, there has not been any search for narrow states in this region. The potential exit channels of importance are $^9\mathrm{B}+p$ and $^6\mathrm{Be}+\alpha$. Because $J^\pi(^3\mathrm{He}) = 1/2^+$ $J^\pi(^7\mathrm{Be}) = 3/2^-$, to have $L_{\mathrm{init}} = 0$ and thus no entrance angular momentum barrier would require the ^{10}C state to have

$$J^\pi = (1 \text{ or } 2)^- \tag{2.19}$$

Because $J^\pi(^9\mathrm{B}) = 3/2^-$, the entrance channel spin and parity required to give $L_{\mathrm{init}} = 0$ will also allow $L_{\mathrm{fin}} = 0$ for the $^9\mathrm{B}+p$. On the other hand, in the final state $^6\mathrm{Be}+\alpha$ both ^{6}Be and ^{4}He have $J^\pi = 0^+$. Thus if the putative ^{10}C state has $J^\pi = 1^-$, this forces the $^6\mathrm{Be}+\alpha$ final state to have $L_{\mathrm{fin}} = 1$, and thus this channel will be suppressed by an angular momentum barrier relative to $^9\mathrm{B}+p$.

Using eq. (2.17), we again get $a_{37} = 4.9$ fm. Taking $L_{init} = 0$ and $E = 0.2$ MeV, Γ_0 is about 10^{-3} keV and is extremely small. However, the penetration factor is highly sensitive to the channel radius and a relatively small increase in a increases the width by orders of magnitude. Increasing the energy does reduce the penetration barrier, but a higher width is required due to thermal suppression. In order to get a sizable width, which is required to solve the problem according to figure 2.8, a_{37}must be $\gtrsim 30$ fm. At this energy, this radius is somewhat larger than what is afforded by Eq. 2.18.

[20] $http://www.tunl.duke.edu/nucldata/figures/11figs/11\_06\_1990.gif$.

Compound Nucleus, J^π, E_{ex}	Initial State	L_{init}	L_{fin}	E_{res}	Γ_{tot}	Exit Channels	Exit Channel Width
^{9}B, $(5/2^+)$, 16.71 MeV	$^7\mathrm{Be}+d$	1	0	219.9 keV	unknown	$p+{}^8\mathrm{Be}^*$ (16.63 MeV)	unknown
			1			$\alpha+{}^5$Li	unknown
^{10}B, 2^+, 18.80 MeV	$^7\mathrm{Be}+t$	1	1	130.9 keV	<600 keV	$p+{}^9\mathrm{Be}^*$ (11.81 MeV)	unknown
			1			^{3}He	unknown
			2			α	unknown
^{10}C, unknown	$^7\mathrm{Be}+{}^3\mathrm{He}$	unknown	unknown	unknown	unknown	p	unknown
			unknown	($Q=15.003$ MeV)		α	unknown
						^{3}He (elastic)	unknown

Table 2.11: This table lists surviving candidate resonances.

2.6 Discussion and Conclusions

The lithium problem was foreshadowed before precision cosmic microwave background data, was cast in stark light by the first-year WMAP results, and has only worsened since. While astrophysical solutions are not ruled out, they are increasingly constrained. Thus, a serious and thorough evaluation of all possible nuclear physics aspects of primordial lithium production is urgent in order to determine whether the lithium problem truly points to new fundamental physics.

Reactions involving the primordial *production* of mass-7, and its lower-mass progenitor nuclides, are very well studied experimentally and theoretically, and leave no room for surprises at the level needed to solve the lithium problem Cyburt & Pospelov (2012); Boyd et al. (2010b); Cyburt et al. (2003). Lithium *destruction* reactions are less well-determined. While the dominant destruction channels $^7\mathrm{Be}(n,p)^7\mathrm{Li}$ and $^7\mathrm{Li}(p,\alpha)\alpha$ have been extensively studied, in contrast, the subdominant destruction channels are less well-constrained.

We therefore have exhaustively cataloged possible resonant, mass-7 destruction channels. As evidenced by the large size of Tables 2.1–2.10, the number of potentially interesting compound states is quite large. However, it is evident that the basic conservation laws such as angular momentum and parity coupled with the requirement of resonant reactions to be 2–3 times the $^7\mathrm{Be}(n,p)^7\mathrm{Li}$ rate prove to be extremely restrictive on the options for a resonant solution to the lithium problem, and reduces the possibilities dramatically.

Given existing nuclear data, there are several choices for experimentally identified nuclear

resonances which come close to removing the discrepancy between the lithium WMAP+BBN predictions and observations as tabulated in § 2.5. The 16.71 MeV level in ^{9}B compound nucleus, and the 18.80 MeV level in the ^{10}B compound nucleus are two such candidates. It is possible, however, that resonant effects have been neglected in reactions passing through states which have been entirely missed. In all of the plots above, we have illustrated the needed positions and strengths of such states, if they exist. One possibility involving the compound state ^{10}C is poorly studied experimentally, especially at higher energy states close to the Q-value for $^{7}\mathrm{Be} + {}^{3}\mathrm{He}$.

Any of these resonances (or a combination) could offer a partial or complete solution to the lithium problem, but in each case, we find that large channel radii ($a > 10$ fm) are needed in order that the reaction widths are large enough. We confirm the results of Cyburt and Pospelov Cyburt & Pospelov (2012) in this regard concerning $^{7}\mathrm{Be} + d$, and we also find similar channel radii are needed for $^{7}\mathrm{Be} + t$, while larger radii are required for $^{7}\mathrm{Be} + {}^{3}\mathrm{He}$. Obviously, nature need not be so kind (or mischievous!) in providing such fortuitious fine-tuning. But given the alternative of new physics solutions to the lithium problem, it is important that all conventional approaches be exhausted.

Thus, based on our analysis, quantum mechanics could allow resonant properties that can remove or substantially reduce the lithium discrepancy. An experimental effort to measure the properties of these resonances, however can conclusively rule out these resonances as solutions. If all possible resonances are measured and found to be unimportant for BBN, this together with other recent work Boyd et al. (2010b), will remove any chance of a "nuclear solution" to the lithium problem, and substantially increase the possibility of a new physics solution. Thus, regardless of the outcome, experimental probes of the states we have highlighted will complete the firm empirical foundation of the nuclear physics of BBN and will make a crucial contribution to our understanding of the early universe.

We are pleased to acknowledge useful and stimulating conversations with Robert Wiringa, Livius Trache, Shalom Shlomo, Maxim Pospelov, Richard Cyburt, and Robert Charity. The

work of KAO was supported in part by DOE grant DE–FG02–94ER–40823 at the University of Minnesota.

Chapter 3

Inverse-Compton Emission from Star-forming Galaxies

Abstract

[1] *Fermi* has resolved several star-forming galaxies, but the vast majority of the star-forming universe is unresolved, and thus contributes to the extragalactic gamma ray background (EGB). Here, we calculate the contribution from star-forming galaxies to the EGB in the *Fermi* range from 100 MeV to 100 GeV, due to inverse-Compton (IC) scattering of the interstellar photon field by cosmic-ray electrons. We first construct one-zone models for individual star-forming galaxies assuming supernovae power the acceleration of cosmic rays. We develop templates for both normal and starburst galaxies, accounting for differences in the cosmic-ray electron propagation and in the interstellar radiation fields. For both types of star-forming galaxies, the same IC interactions leading to gamma rays also substantially contribute to the energy loss of the high-energy cosmic-ray electrons. Consequently, a galaxy's IC emission is determined by the relative importance of IC losses in the cosmic-ray electron energy budget ("partial calorimetry"). We calculate the cosmological contribution of star-forming galaxies to the EGB, using our templates and the cosmic star-formation rate distribution. For all of our models, we find the IC EGB contribution is almost an order of magnitude less than the peak of the emission due to cosmic-ray ion interactions (mostly pionic $p_{\rm cr}p_{\rm ism} \rightarrow \pi^0 \rightarrow \gamma\gamma$); even at the highest *Fermi* energies, IC is subdominant. The flatter IC spectrum increases the high-energy signal of the pionic+IC sum, bringing it closer to the EGB spectral index observed by *Fermi*. Partial calorimetry ensures that the overall

[1]This chapter matches the version which has been submitted to Astrophysical Journal, and posted version on arxiv.org numbered on arXiv:1206.0770 and is co-authored with Brian Fields.

IC signal is relatively well-constrained, with only uncertainties in the amplitude and spectral shape for plausible model choices. We conclude with a brief discussion on how the pionic spectral feature and other methods can be used to measure the star-forming component of the EGB.

3.1 Introduction

The window to the high-energy (> 30 MeV) gamma-ray cosmos has been open now for four decades, with measurements of the diffuse emission by COS-B, (Caraveo et al., 1980; Mayer-Hasselwander et al., 1980; Lebrun et al., 1982), OSO-3 satellite (Kraushaar et al., 1972) followed by the second Small Astronomy Satellite (SAS-2)(Fichtel et al., 1975) and the Energetic Gamma Ray Experiment Telescope (EGRET) (Hunter et al., 1997; Sreekumar et al., 1998). SAS-2 was the first to reveal a diffuse, extra-Galactic gamma ray background (EGB). More recently, the advent of the *Fermi* Gamma-Ray Space Telescope has substantially sharpened our observational view of the EGB. With better energy and angular resolution and much higher sensitivity than EGRET, *Fermi* has resolved many more gamma-ray point sources and better determined the diffuse background and its energy dependence. The EGB data are consistent with a power law of spectral index 2.41 ± 0.05 for energies > 100 MeV (Abdo et al., 2010k).

The origin(s) of the EGB remains an open question. Contributions from active galaxies (e.g., Strong et al., 1976a; Abdo et al., 2009; Stecker & Venters, 2011; Abazajian et al., 2011) and star-forming galaxies (e.g., Strong et al., 1976b; Bignami et al., 1979; Pavlidou & Fields, 2002; Fields et al., 2010; Stecker & Venters, 2011; Makiya et al., 2011) are "guaranteed" in the sense that these known, resolved extragalactic source classes must have *unresolved* counterparts that will contribute to the EGB. Other possible EGB sources include truly diffuse emission such as dark matter annihilation (Ando et al., 2007), interactions from cosmic rays accelerated in structure formation shocks (e.g., Loeb & Waxman, 2000; Miniati,

2002), unresolved ordinary and millisecond pulsars (Faucher-Giguère & Loeb, 2010; Geringer-Sameth & Koushiappas, 2012), and even Solar-System emission from cosmic-ray interactions with Oort cloud bodies (Moskalenko & Porter, 2009).

One of *Fermi's* major achievements has been to establish external star-forming galaxies as a new class of gamma-ray sources. These detections give a global view of the gamma-ray output as a result of star formation, complementary to the local gamma-ray images within the Milky Way. *Fermi* has discovered γ-rays from "normal" galaxies undergoing quiescent star formation, but only detected our very nearest neighbors, as anticipated (Pavlidou & Fields, 2001). The Large Magellanic Cloud (LMC; Abdo et al., 2010i) has even spatially resolved, and the SMC (Abdo et al., 2010d) and M31(Abdo et al., 2010f) have also been detected. Other normal star-forming galaxies in the Local Group (including M33) have not yet been seen (Abdo et al., 2010f; Lenain & Walter, 2011). Beyond the Local Group, *Fermi* has detected starbursts galaxies characterised by very high star-formation rates, as anticipated by Torres et al. (2004). *Fermi* has detected the starbursts M82 and NGC 253 (Abdo et al., 2010a) which had been detected at TeV energies by VERITAS (VERITAS Collaboration et al., 2009) and HESS (Acero et al., 2009) respectively. In addition *Fermi* has also detected the starbursts NGC 1068 and NGC 4945 (Nolan et al., 2012b).

The *Fermi* star-forming galaxies offer a qualitatively new probe of cosmic rays; they also inform and calibrate efforts such as ours to understand the EGB contribution from the vast bulk of the star-forming universe that remains *unresolved*. The LMC is the best resolved individual system, and there the energy spectrum is consistent with pionic, while the spatial distribution can be used to study cosmic-ray propagation (Murphy et al., 2012). More broadly, the ensemble of all *Fermi* star-forming galaxies encodes information about global cosmic-ray energetics and interaction mechanisms (Persic & Rephaeli, 2010; Lacki et al., 2011; Persic & Rephaeli, 2012). In particular, *Fermi* reveals a strong correlation between gamma-ray luminosity L_γ and supernova rate (or equivalently star-formation rate ψ). This is expected if supernovae provide the engines of cosmic-ray acceleration. Remarkably, all

star-forming galaxies detected to date can be well-fit with a single power law $L_\gamma \propto \psi^{1.4\pm0.3}$ (e.g., Abdo et al., 2010f).

The main mechanism of gamma ray production in normal star-forming galaxies is anticipated to be the same that dominates Milky Way diffuse gamma rays: pionic emission $p_{\rm cr}p_{\rm ism} \rightarrow pp\pi^0 \rightarrow \gamma\gamma$, arising from interactions between cosmic-ray hadrons (ions) and interstellar gas (Stecker & Venters, 2011; Abdo et al., 2009; Fields et al., 2010; Strong et al., 2010). This mechanism is likely responsible for the non-linear relation between the luminosity of *Fermi* galaxies and their star-formation rate. Namely, the observed correlation is consistent with a picture (Pavlidou & Fields, 2001; Fields et al., 2010; Persic & Rephaeli, 2011) in which the cosmic-ray proton flux is controlled by the supernova rate, the total number of targets is set by the galaxy's gas mass, and the gas and star-formation are linked by the Schmidt-Kennicutt relation (Kennicutt, 1998).

Here, we examine the cosmological contribution of star-forming galaxies by the inverse-Compton (IC) scattering $e_{\rm cr}\gamma_{\rm is} \rightarrow e\gamma$ of cosmic-ray electrons on the interstellar radiation field (ISRF). In order to do so, we construct a one-zone model of star-forming galaxies. We normalize the IC emission (per unit star formation) in our model differently for normal and for starburst galaxies. For normal galaxies we match to the Milky Way IC emission as computed in GALPROP (Strong et al., 2010), while for starburst galaxies we set the template matching M82 star formation rate and cosmic ray propagation consistent with multiwavelength data just as other authors do (eg., Stecker & Venters, 2011; Lacki et al., 2012; Paglione & Abrahams, 2012).

The IC gamma rays are produced by upscattering of interstellar radiation by high-energy cosmic-ray electrons (Felten & Morrison, 1963; Felten, 1965; Brecher & Morrison, 1967). Inverse-Compton scattering also represents an important energy loss mechanism for these electrons; the other important losses are bremsstrahlung and synchrotron. The relative importance of these losses depends on the cosmic-ray energy and on interstellar radiation and matter densities. Where inverse Compton losses dominate, the energy injected into

cosmic-ray electrons is ultimately re-emitted as IC gamma-ray photons. This equality of energy loss and energy output is known as calorimetry, and was first described in the context of high-energy electrons by Felten (1965) and Voelk (1989) and explored in detail for diffuse high-energy gamma rays by cosmic rays by Pohl (1994) and by Strong et al. (2010). If the other losses are negligible then we have perfect calorimetry. But realistically, other losses compete, and so the gamma-ray energy output is reduced by the IC fraction of the energy losses by the cosmic rays.

In contrast to the loss-dominated propgations of cosmic-ray electrons, cosmic-ray hadrons (mainly protons, as well as other ions) in the Milky Way suffer losses dominated by escape. The pionic emission from normal star-forming galaxies is thus not calorimetric; however, in the dense central regions of starburst galaxies, proton inelastic interactions can dominate losses and lead to calorimetry (Lacki et al., 2010; H. E. S. S. Collaboration et al., 2012). In the Milky Way, pionic emission dominates the total Galactic gamma-ray output (luminosity), exceeding IC emission by factors of up to ~ 5 in GALPROP calculations (Strong et al., 2010). Our analysis will show that the inverse-Compton component from star-forming galaxies over cosmological volumes is nearly an order of magnitude lower than the peak of the pionic component.

The paper is organised as follows. Section 3.2 gives an order-of-magnitude estimate of the inverse Compton EGB contribution by star-forming galaxies, and serves as an overview to our paper. We first build a template for the IC emission from individual star-forming galaxies, treating normal and starburst systems separately. We start with the various components of the background interstellar photon field §3.3. These interstellar photons serve as scattering targets for the cosmic ray electrons, whose propagation is explained in §3.4. For the highest energy background photons and electrons, the scattering occurs in the Klein-Nishina regime, which affects the emergent spectrum and is detailed in §3.5.1. Our one-zone model for the inverse-Compton luminosity from a single galaxy is presented in §3.5.2. In §3.6, the total intensity over cosmological volumes is calculated and compared with the pionic component.

Section 3.7 discusses the implications of our results.

3.2 Order-of-Magnitude Expectations

An order-of-magnitude estimate of our final result will help frame key physical issues and astrophysical inputs. Our goal is to find the EGB contribution from inverse Compton scattering in star-forming galaxies throughout the observable universe. We thus calcualte the gamma-ray specific intensity, I_E, at energy E. For photons up to at least $\lesssim 30$ GeV, the universe is optically thin;[2] thus, the intensity is simply given by the line-of-sight integral

$$I_E \approx \frac{c}{4\pi} \int_{\rm los} d\ell \; \mathcal{L}_\gamma \approx \frac{\mathcal{L}_\gamma d_{\rm H}}{4\pi} \tag{3.1}$$

where $\mathcal{L}_\gamma$ is the luminosity density or cosmic volume emissivity of the galaxies, and $d_{\rm H} = c/H_0 = 3000h^{-1}$ Mpc is the Hubble length. The cosmic luminosity density of a distribution of IC-emitting, star-forming galaxies can be expressed as a product of the luminosity function, $dn_{\rm gal}/dL_\gamma$ and the luminosity of each individual galaxy, L_γ:

$$\mathcal{L}_\gamma = \int L_\gamma \; \frac{dn_{\rm gal}}{dL_\gamma}(L_\gamma) \; dL_\gamma = \langle n L_\gamma \rangle \approx n_{\rm gal} L_E \tag{3.2}$$

where L_E is the luminosity of an average galaxy at energy E.

Within a single galaxy, the gamma-ray luminosity is an integral

$$L_\gamma(E_{\rm em}) \;\; = \;\; \int q_{\rm ic} \; dV_e \tag{3.3}$$

over the volume in which cosmic-ray electrons propagate. Here the inverse-Compton volume emissivity $q_{\rm ic}$ depends on the product of the targets and projectile densities, and the interaction cross section. The density of targets is simply the number density of the interstellar

[2]We negelect the interactions with the extragalactic background light, leaing to pair production $\gamma\gamma \to e^+e^-$; these effects could be important above ~ 100 GeV (e.g., Salamon & Stecker, 1998; Abdo et al., 2010e; Stecker et al., 2012).

photons, $n_{\rm isrf}$. The projectiles are cosmic-ray electrons, with flux density $\phi_{\rm e}$. The cross section is that for inverse Compton scattering, $d\sigma_{\rm ic}/dE_{\rm em}$. Therefore, the emissivity for a single galaxy is given as,

$$q_{\rm ic} \;=\; \left\langle \phi_e \frac{d\sigma_{\rm ic}}{dE_{\rm em}} n_{\rm isrf} \right\rangle \tag{3.4}$$

with the angle brackets indicating averaging over the cosmic-ray and background photon energies.

We will assume that cosmic-ray acceleration is powered by supernova explosions. Indeed, the cosmic-ray/supernova link historically has been better established for cosmic ray electrons than for hadrons, thanks to radio (e.g., Webber et al., 1980; Strong et al., 2011; Bringmann et al., 2012) and X-ray synchrotron (Uchiyama et al., 2007; Helder et al., 2009, e.g.,) measurements. More recently *Fermi*-LAT (Völk et al., 1996; Ahlers et al., 2009) measurements of pionic gamma rays provided the most direct evidence for supernova acceleration of protons and other ions. Consequently, a galaxy's cosmic-ray injection rate is proportional to its supernova rate, $q_{\rm cr} \propto R_{\rm SN}$. And because the supernova rate itself traces the galactic star-formation rate ψ, we conclude that $q_{\rm cr} \propto \psi$.

Cosmic-ray electron propagation is dominated by energy losses in the form of inverse Compton, bremsstrahlung and synchrotron processes. Each contributes to a total energy loss rate $b_{\rm tot} = |dE_{\rm e}/dt|$. The IC loss rate is proportional to the background photon energy density: $b_{\rm ic} \propto U_{\rm isrf} \propto n_{\rm isrf}$. The cosmic-ray flux $\phi_{\rm e}$ is inversely proportional to the total energy loss rate, $b_{\rm tot}$ $\phi_{\rm e} \propto (q_{\rm e}/\ b_{\rm tot})$. Thus, IC emissivity, $q_{\rm ic}$ is *lower* than rate $q_{\rm e}$ of energy injection into cosmic-ray electrons, by the fraction $b_{\rm ic}/b_{\rm tot}$ of energy losses in IC, $q_{\rm ic} \propto (b_{\rm ic}/\ b_{\rm tot})q_{\rm e}$. This is the case of partial or fractional calorimetry where $q_{\rm ic}/q_e \propto b_{\rm ic}/b_{\rm tot}$: IC photons trace the portion of cosmic-ray energy lost via this mechanism (Pohl, 1994). Even the approximate validity of calorimetry is sufficient that the IC gamma ray luminosity is a fairly robust calculation.

Due to partial calorimetry, the IC volume emissivity is $q_{\rm ic} \propto q_e$, and integration over all of the supernovae acting as cosmic-ray accelerators gives the IC luminosity $L_E \propto R_{\rm SN} \propto \psi$. Physically, a fixed fraction of each supernova's energy goes into cosmic-ray electrons and ultimately into IC photons.

For normal star-forming galaxies, this scaling can then be compared to GALPROP estimates for the total Milky-Way IC luminosity (Strong et al., 2010), which determines the IC output per unit star-formation. We can then find the luminosity for any star-forming galaxy at a fiducial energy of $E = 1$ GeV as,

$$\begin{aligned} E^2\ L_E &= E^2\ L_{E,\rm MW} \left(\frac{\psi}{\psi_{\rm MW}} \right) \\ &\approx 10^{40}\ {\rm GeV}^2\ {\rm sec}^{-1}\ {\rm GeV}^{-1} \left(\frac{\psi}{1\ M_\odot\ {\rm yr}^{-1}} \right) \end{aligned} \tag{3.5}$$

where $\psi_{\rm MW}$ is the Milky-Way star-formation rate.

From eqns. (3.1) (3.2), and (3.5), we estimate the IC contribution to the EGB intensity at 1 GeV as

$$\begin{aligned} E^2\ I_E\big|_{\rm ic,1\,GeV} &\approx \frac{L_{E,\rm MW}\ n_{\rm gal}\ d_{\rm H}}{4\ \pi} \left(\frac{\psi}{\psi_{\rm MW}} \right) \approx \frac{L_{E,\rm MW}\ d_{\rm H}}{4\ \pi\ \psi_{\rm MW}} \dot{\rho}_\star(1) \\ &\approx 3 \times 10^{-8}\ {\rm GeV\ cm^2\ sec^{-1}\ sr^{-1}} \end{aligned} \tag{3.6}$$

where $\dot{\rho}_\star(1) = \psi n_{\rm gal} \approx 0.1\ {\rm M_\odot\ yr^{-1}\ Mpc^{-3}}$ is the cosmic star formation rate, evaluated at $z = 1$, near its peak (Horiuchi et al., 2009a). For comparison, the pionic model of Fields et al. (2010) gives an intensity $E^2\ I_E|_{\pi\to\gamma\gamma,1\,\rm GeV} \sim 3\times10^{-7}$ GeV cm^2 sec^{-1} sr^{-1}, with a factor ~ 2 uncertainty in normalisation. The EGB measured by *Fermi*-LAT is $E^2\ I_E|_{\rm obs,1\,GeV} = 6\times 10^{-7}$ GeV cm^2 sec^{-1} sr^{-1} (Abdo et al., 2010k). Thus, the pionic component alone dominates the overall amplitude from the star-forming galaxies, which is an important contribution to the total observed flux. Not evident from our estimate is that the shape of the star-forming spectrum improves upon addition of the IC component, as we will see in §3.6.

3.3 Targets: Interstellar Photon Fields

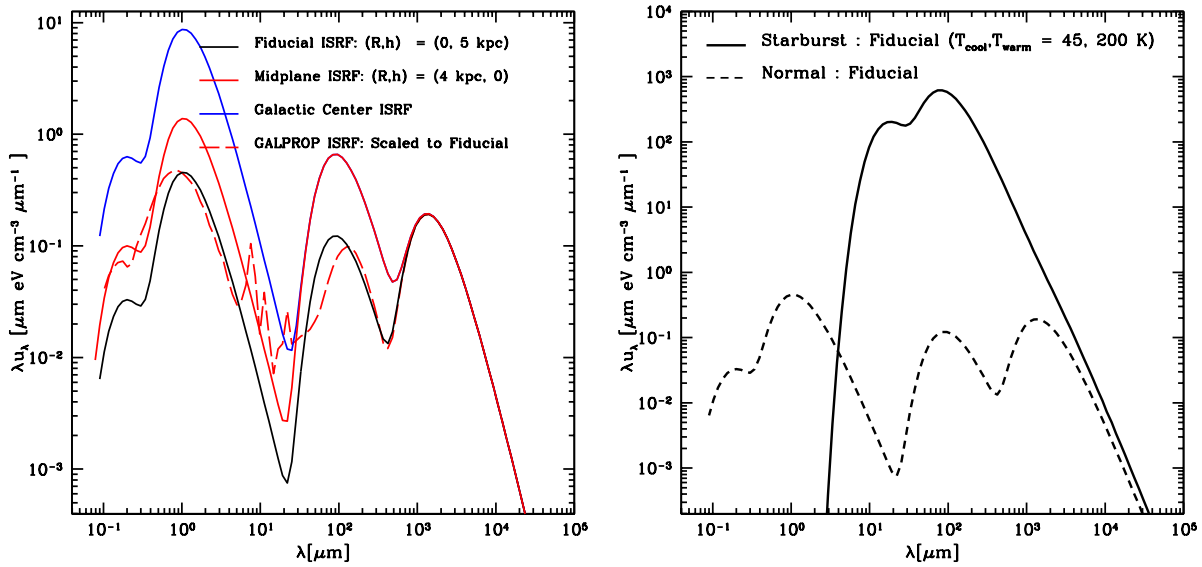

Figure 3.1: The interstellar photon field (ISRF) energy density, shown as a function of the wavelength for normal (left panel) and starburst galaxies (right panel). *(a) Left: Milky-Way template for normal galaxies* The model includes thermal components for starlight (optical), dust (IR) and the CMB as in Cirelli & Panci (2009). It includes another thermal component for the starlight in the UV. The black (fiducial), red and blue curves represent the curves for (R, h) = (0,5 kpc), (4 kpc,0) and (0,0) respectively. *(b) Right: M82 template for starburst galaxies.* The solid black curve is a model (de Cea del Pozo et al., 2009) for a starburst ISRF dominated by IR emission due to the dusty nuclei. It has two thermal components, a cool one at 45 K and a warm one at 200 K as in de Cea del Pozo et al. (2009). These correspond to IR luminosity of $10^{10.5} L_{\rm sol}$ and a core radius of 200 pc. It is compared with the fiducial ISRF of the Milky Way type normal galaxy shown in dashed black.

Cosmic-ray electrons in a galaxy will inverse-Compton upscatter ambient photons, which are commonly called the interstellar radiation field (ISRF). Each galaxy's ISRF is a rich function of both energy and geometry. We simplify this complex reality by treating a galaxy as a single zone for the purposes of cosmic-ray propagation and gamma-ray emission. Thus, our ISRF is meant to give a sort of effective volume average of the radiation field encountered by cosmic-ray electrons. A galaxy's ISRF will evolve with redshift, and so for our single-galaxy templates we must also create a prescription for how the different ISRF component evolve with z.

Our choice of ISRF for normal galaxies follows those of models for the Milky Way, which we adjust at other cosmic epochs via scaling arguments. These scalings use the cosmic star-formation rate $\dot{\rho}_\star(z)$, whose change with redshift we characterize by the dimensionless function

$$S(z) \equiv \frac{\dot{\rho}_\star(z)}{\dot{\rho}_\star(0)} \tag{3.7}$$

where today $S(0) = 1$.

For the ISRF at the present day (redshift $z = 0$), we adopt but extend the model proposed by Cirelli & Panci (2009), which consists of three thermal components corresponding to the infra-red (or dust), optical, and the Cosmic Microwave Background (CMB). To this we add a fourth thermal component for the UV. Our goal is to build a simple model that can reproduce the inverse Compton luminosity of the Milky Way according to Strong et al. (2010); their calculation is based on a far more detailed, spatially-dependent ISRF as implemented in the GALPROP code (Strong et al., 2000; Porter et al., 2008). The strengths of the UV, IR and the optical relative to the CMB decreases with Galactocentric radial distance R and also with height h above the Galactic plane. This is seen in Fig. 3.1.

We may express the ISRF specific energy density $du_{\rm isrf}/d\epsilon = \epsilon\, dn_{\rm isrf}/d\epsilon$ as

$$\lambda \frac{du_{\rm isrf}}{d\lambda} = \epsilon \frac{du_{\rm isrf}}{d\epsilon} \quad = \quad \sum_{i=1}^{4} f_{\rm i}\ \frac{1}{\pi^2} \frac{\epsilon^4}{\exp(\epsilon/T_{\rm i}) - 1} \tag{3.8}$$

a sum of Planck terms, with dimensionless weights $f_{\rm i}$ for the different background components: $i =$ UV, optical, IR and the CMB. The UV and optical component are from starlight, and the IR comes from starlight reprocessed by dust. Our model, as seen in the Fig. 3.1 thus includes the effect of the major components in the GALPROP ISRF, which dominate the energy density. For the IR, we tried a non-thermal model that includes effect of both scattering and absorption by dust particles, but the effects on our gamma ray luminosity model are insignificant. Therefore, we retain the thermal model for IR. We also verified that including the optical-IR transition where the non-thermal lines appear has negligible effect

on the final gamma ray luminosity.

Figure 3.1 shows the ISRF at different locations in the Galaxy. The optical and dust components are taken from Cirelli & Panci (2009). We add another thermal component for the UV. The black, red and blue curves correspond to the positions $(R, h) = (0, 5)$, (4,0) and (0,0) kpc. The peaks due to starlight and IR change with position in the Galaxy, while the CMB contribution peaked at $\lambda \approx 1000$ microns remains the same. At the Galactic centre, the energy densities of these latter components are greater than the CMB, with optical photons dominating. Above the Galactic plane, the CMB becomes comparable in energy density and eventually dominates at very large h.

Table 3.1 lists the temperatures of the various ISRF components along with their relative weights at zero redshift, $f_{\rm i}(0)$ for the normal galaxies. We chose as a fiducial model the relative strengths for regions corresponding to $10^\circ < |b| < 20^\circ$ and $0^\circ < l < 360^\circ$, corresponding to the '10-20' model of Cirelli & Panci (2009). This is for the position $(R, h) = (0, 5)$ Kpc represented by the black curve in Fig. 3.1. The UV component at this position is scaled from that in the Galactic Centre, (Porter et al., 2008) in the same proportion as the optical component in these positions. This choice of model, with the overall normalisation adjusted, reproduces the Milky Way IC luminosity as a function of energy from Strong et al. (2010).

The ISRF in starburst nuclei is dominated by the IR peak, which renders other components relatively unimportant. Our one zone ISRF template is based on the two-component model of de Cea del Pozo et al. (2009). The starburst ISRF is dominated by a thermal peak corresponding to a temperature, $T = 45$ K, according to de Cea del Pozo et al. (2009). The energy density is related to the IR luminosity, L from the nucleus of radius R as, $U_{\rm isrf} = L/2\pi R^2 c$ (Lacki et al., 2010). Picking a normalisation based on the energy density $U_{\rm isrf} \approx 1100$ eV cm^{-3}, set by luminosity, $L = 10^{10.5} L_\odot$, and radius, R = 200 pc, we get the green curve in the right panel of Fig. 3.1. However, according to de Cea del Pozo et al. (2009), the dust emission fits better with an additional warm component with temperature of 200 K. This is our fiducial model. The choice of the fiducial ISRF is displayed in solid

black in the right panel of Fig. 3.1. It is also summarised in the table 3.1. And we pick the overall normalisations $f_i(0)$ in order match the same energy density as for the one component case.

Table 3.1: ISRF Parameters for normal galaxies

Milky Way	UV	Optical	IR	CMB
Fiducial : $f_{\rm i}(z=0)$	8.4×10^{-17}	8.9×10^{-13}	1.3×10^{-5}	1
Galactic Centre $f_{\rm i}(z=0)$	1.6×10^{-15}	1.7×10^{-11}	7×10^{-5}	1
$T(z=0)$ [K]	1.8×10^{4}	3.5×10^{3}	41	2.73

Table 3.2: ISRF Parameters for starburst galaxies

Starburst M82 type	UV	Optical	IR (cool)	IR (warm)	CMB
Fiducial : $f_{\rm i}(z=0)$	3.2×10^{-15}	0.0	4.22×10^{-2}	3.61×10^{-5}	1
$T(z=0)$ [K]	1.8×10^{4}	3.5×10^{3}	45	200	2.73

Because we are interested in inverse Compton emission from star-forming galaxies over all of cosmic history, we must specify the cosmic evolution of the ISRF. This will depend on which stars contribute to starlight and dust scattered light. The detailed present-day Milky-Way model in Strong et al. (2000) uses the stellar luminosity functions from Wainscoat et al. (1992). The UV and IR components derive from short-lived massive stars, and the resulting starlight density will be proportional to the star-formation rate. Thus, we adopt the scalings

$$\begin{aligned} f_2(z) &= f_{\rm UV}(z) = f_{\rm UV}(0)\ S(z), \\ f_3(z) &= f_{\rm IR}(z) = f_{\rm IR}(0)\ S(z) \end{aligned} \tag{3.9}$$

The optical component is less trivial and evolves differently for different stellar populations. Massive supernova progenitors, as well as AGB progenitors, are short-lived compared to $\gtrsim$ 1Gyr timescales for cosmic star formation. Consequently, the optical radiation density of these stars would scale as

$$f_2(z) = f_{\rm op}(z) = f_{\rm op}(0)\ S(z) \quad , \tag{3.10}$$

in step with the UV and IR scaling. For reasonable initial mass functions and star-formation

histories, these stars should dominate the optical ISRF. But lower-mass main sequence stars and their red giant descendants have cosmologically long lifetimes; this means that their starlight density at any epoch would scale as the integrated star-formation rate. Therefore, their contribution to the optical component would scale as

$$f'_{\rm op}(z) = f_{\rm op}(0)\frac{\int_z^\infty dz|\frac{dt}{dz}|\ \dot{\rho}_\star}{\int_0^\infty dz|\frac{dt}{dz}|\ \dot{\rho}_\star} \quad , \tag{3.11}$$

This would give a lower optical component and decrease the IC intensity as we will see. We will adopt eq. (3.10) for our fiducial model, but we will explore the effects of using eq. (3.11); these cases will bracket the true evolution.

The redshift dependence of the CMB is precisely known and can be expressed entirely in terms of its temperature,

$$T_{\rm CMB}(z) = (1+z)\ T_{\rm CMB}(0) \tag{3.12}$$

with $f_4(0) = f_{\rm CMB}(0) = 1$. The CMB energy density thus grows rapidly as $U_{\rm cmb} \propto (1+z)^4$.

3.4 Projectiles: Cosmic-Ray Electron Source and Propagation

An electron with energy $E_{\rm e} = \gamma mc^2$ scattering off a background photon of energy ϵ yields an IC photo with energy $E_\gamma \sim \gamma^2\epsilon$. In order to produce gamma rays around the *Fermi* range $E_\gamma \sim 100$ MeV to ~ 300 GeV , electrons with energies of few GeV to few TeV are required, depending on the energy of initial un-scattered photon. These are the electrons of interest to us.

High-energy cosmic-ray electrons obey a complex transport equation (e.g., Strong & Moskalenko, 1998). This in general would include effects of diffusion, convection, escape, radiative losses, etc. However, our approach is to create the simplest one-zone model that

captures electron source spectrum and their most important losses.

We model cosmic-ray electron injection for normal galaxies via the source spectrum from the Plain Diffusion (PD) model of Strong et al. (2010). In this model, electrons are accelerated with a broken power-law injection spectrum having $q_e(E_\mathrm{e}) \propto E_\mathrm{e}^{-1.8}$ up to a break at $E_{e,\mathrm{break}} = 4$ GeV, and above this $q_e(E_\mathrm{e}) \propto E_\mathrm{e}^{-2.25}$. Electrons below $E_{e,\mathrm{break}}$ can produce inverse Compton gamma rays at the low end of the *Fermi* range, when upscattering optical and UV photons. Gamma rays at higher energies are produced by electrons above the break energy. Thus, it is important to include the injection break in our calculations. Including a cutoff at 2 TeV according to Strong et al. (2011), results in a rollover at high energies improving the agreement with the GALPROP model beyond 100 GeV.

For starburst galaxies the injected cosmic-ray electrons important for IC emission are difficult to constrain independently from gamma-ray emission, and thus are more uncertain. For starburst galaxies, we use M82 as a template, and thus scale the injected spectrum up from that of the Milky Way by the ratio $\psi_{\mathrm{M82}}/\psi_{\mathrm{MW}}$ of star-formation rates, using $\psi_{\mathrm{M82}} = \psi_8\ M_\odot\ yr^{-1}$ in accordance with the total IR luminosity Sanders et al. (2003) as used by Lacki et al. (2012). For our fiducial model we adpot an injection spectrum that is a single power law $q_e(E_\mathrm{e}) \propto E_\mathrm{e}^{-2.1}$, although other indices ranging from 2.0 to 2.4 are permissible (Paglione & Abrahams, 2012). The high-energy cutoff being less constrained (Lacki et al., 2012) we pick fiducial value of 2 TeV, same as the Milky Way. Our fiducial model is directly comparable with Paglione & Abrahams (2012).

Milky-Way cosmic-ray electrons experience an interstellar diffusion coefficient, $D_0 \sim 10^{28}\mathrm{cm}^2\mathrm{sec}^{-1}$ (Strong et al., 2010), so the diffusion length for electrons over the Compton loss time-scales is $\ell_{\mathrm{diff}} \sim 0.01 - 1$ kpc, depending on the energy. We thus see that electrons will not venture far from the Galaxy, but can range vertically outside the Galactic midplane. Hence, very few electrons will be lost to escape, in strong contrast to ions for which escape dominates (Pohl, 1994). We thus will ignore electron escape in our analysis.

However, since the electrons do propagate throughout and above the stellar and gaseous

disk, the electron population sees a wide variety of radiation fields. Our single choice is a crude approximation meant to represent a sort of average ISRF. As a result, the electron propagation equation takes the "thick target" form

$$\frac{\partial}{\partial t}\phi_e(E_e) = q_e(E_e) + \frac{\partial}{\partial E_e}\left[b(E_e)\phi_e(E_e)\right] \tag{3.13}$$

where $q_e(E_e)$ is the source term and $b(E_e) = |dE_e/dt|$ is the total rate of energy loss. The equilibrium (i.e., $\partial_t \phi_e = 0$ steady state) solution of the cosmic ray flux is

$$\phi_{\rm e}(E_{\rm e}) = \frac{1}{b(E_{\rm e})}\int_{E_{\rm e}} dE'_e\; q_e(E'_e) = \frac{q_e(>E_e)}{b(E_{\rm e})} \tag{3.14}$$

As usual in the thick-target limit, the electron flux is directly proportional to the energy-integrated injection rate $q_e(>E_e)$, and inversely proportional to the total energy loss rate. In general, the total energy loss rate of the electrons is given by sum of the inverse Compton, synchrotron, bremsstrahlung and ionisation losses,

$$b_{\rm tot}(E_{\rm e}) = b_{\rm ic}(E_{\rm e}) + b_{\rm sync}(E_{\rm e}) + b_{\rm brem}(E_{\rm e}) \quad ; \tag{3.15}$$

we now address each in turn. The ionisation loss is unimportant throughout the entire electron energy range of interest here.

The inverse Compton loss in the Thomson regime takes the simple form $b_{\rm ic}(E_{\rm e}) \stackrel{\rm Thoms}{=} \frac{4}{3}\sigma_{\rm T}\; c\; U_{\rm isrf}\left(\frac{E_{\rm e}}{m\; c^2}\right)^2$. However, the full Compton cross section takes the Klein-Nishina form described in more detail in §3.5.1. Corrections to the Thomson limit become important when $\Delta_\epsilon = 4\;\epsilon\gamma/m\;c^2 \gg 1$; in a starlight-dominated ISRF with $\epsilon \sim 1$ eV, this occurs for electrons with $\gamma \gg 10^5$. This energy regime is important for our calculation and therefore, we calculate the inverse Compton loss rate by combining the Klein-Nishina cross section

self-consistently with the (redshift-dependent) ISRF:

$$
\begin{aligned}
b_{\rm ic}(E_{\rm e}) &= \int_0^\infty d\epsilon\ \frac{dn_{\rm isrf}}{d\epsilon}(\epsilon) \int dE_{\rm em}\ (E_{\rm em}-\epsilon)\frac{d\sigma_{\rm ic}}{dE_{\rm em}} \\
&= 3\ \sigma_{\rm T}\ c\ \int_0^\infty d\epsilon\ \frac{dn_{\rm isrf}}{d\epsilon}(\epsilon)\ \epsilon\ \int_{(m\ c^2/2E_{\rm e})^2}^1 dq\ \frac{(4\ \left(\frac{E_{\rm e}}{m\ c^2}\right)^2-\Delta_\epsilon)q-1}{(1+\Delta_\epsilon q)^3} \\
&\quad \times\left(2q\ \ln(q)+(1+2q)(1-q)+\frac{1}{2}\frac{(\Delta_\epsilon q)^2}{1+\Delta_\epsilon q}(1-q)\right)
\end{aligned}
\tag{3.16}
$$

as in Cirelli & Panci (2009), where

$$
q=\frac{E_{\rm em}}{4\epsilon\gamma^2(1-E_{\rm em}/\gamma m\ c^2)}\quad . \tag{3.17}
$$

Note also that for the highest-energy electrons, inverse Compton losses become catastrophic, i.e., in each scattering event the fractional changes in the electron energy approach $\delta E_e/E_e \sim 1$ (e.g., Blumenthal & Gould, 1970). In this case the losses can no longer be treated as a smooth function $b_{\rm ic}(E_{\rm e})$ that averages over many scatterings each with $\delta E_e/E_e \ll 1$; we do not include these effects, which impact gamma-ray energies of $E_{\rm em} \gtrsim 1$ TeV.

The relative importance of the losses determines the propagated electron spectrum (Felten, 1965; Pohl, 1993). For our fiducial ISRF model, the bremsstrahlung, synchrotron and Compton losses are all important, depending on the part of the spectrum. The rates are given in the Appendix B.1. For electron energies lower than ~ 1 GeV, bremsstrahlung is dominant scaling as $b_{\rm brem} \propto E_e$, with Compton losses being comparable close to the break energy at $E_{\rm e} = 4$ GeV, scaling as $b_{\rm ic} \propto E_e^2$. Since, the electron injection spectral break and the bremsstrahlung–Compton transition are fairly close, instead of seeing two breaks corresponding to these two cosmic ray propagation regimes, only one is seen near the break energy as described in §3.4. For large E_e, inverse Compton losses drop off to a logarithmic energy dependence due to Klein-Nishina suppression, while synchrotron losses maintain $b_{\rm sync} \propto E_e^2$. Thus synchrotron losses dominate over Compton at TeV and higher energies.

The losses themselves evolve with redshift, through the dependences on interstellar den-

sities, i.e., the ISRF energy density $U_{\rm isrf}$, the interstellar magnetic energy density $U_{\rm mag} = B^2/8\pi$, and the number densities $n_{\rm ism}$ of interstellar particles. The magnetic field couples to all cosmic rays, for which the ions dominate the energy density. This coupling is likely responsible for the approximate equipartition of magnetic field and cosmic-ray energy densities observed in the local interstellar medium. We thus assume that the magnetic field energy density scales with the cosmic-ray ion flux, and in turn with the star-formation rate: $U_{\rm mag} \propto S(z)$. For our fiducial normal galaxy model, we use $B_0 = 4\ \mu$ G, to match the model of Strong et al. (2010), which is comparable with the typical value in Strong et al. (2011).

We take interstellar particle densities, which control bremsstrahlung losses, to scale as

$$n_{\rm i}(z) = n_{\rm i,0}(1+z)^3 \tag{3.18}$$

This can be viewed a consequence of the disk radius scaling with the cosmic scale factor $R_{\rm disk} \propto a \propto (1+z)^{-1}$ in the Fields et al. (2010) model, and to reflect proportionality between galaxy disk and dark halo sizes. The fiducial number densities of neutral and ionised hydrogen, i.e. $n_{\rm H\ II,0} = n_{\rm H\ I,0} = 0.06$ cm^{-3}. The helium content of ionised and neutral gas is also included, with $y_{\rm He} = 0.08$. These parameters are broadly consistent with values at intermediate heights h above the Galactic plane, as befits the volume average represented by our one-zone model. For reference, the values of $n_{\rm ism}$ and B used at the Galactic centre are much higher at $B_0 = 8.3\ \mu$G and $n_{\rm H\ II,0} = n_{\rm H\ I,0} = 0.12$ cm^{-3}.

For starburst galaxies, the magnetic fields and the interstellar densities are higher. The uncertainty attached with them are also higher compared to Milky Way type normal galaxies. The fiducial values for magnetic field chosen here is $B = 300\ \mu$G, although different values are possible depending on the radio observations of electrons and assumptions regarding the e/p injection ratio (Lacki et al., 2010; Paglione & Abrahams, 2012; Lacki et al., 2012). Changing B will change the importance of the IC relative to synchrotron and also pionic losses. The fiducial ISM density is $n_{\rm ism} = 600$ cm^{-3} is comparable to the mean densities

from observations of M82 (Weiß et al., 2001). These parameter values are in similar range as used by other groups such as Lacki et al. (2012); Paglione & Abrahams (2012). The redshift dependence of these parameters is chosen to be the same as for normal galaxies.

3.5 Inverse Compton Emission from Individual Star-Forming Galaxies

As seen in eq. (3.2), we first compute the luminosity of single galaxy and then average suitably over the luminosity function to get the luminosity density or cosmic volume emissivity. In this section, we address the former, focussing first on the IC emissivity *within* the volume of a single galaxy, then using this to compute the total luminosity from that galaxy.

3.5.1 Inverse Compton Emissivity of a Star-Forming Galaxy

The specific IC volume emissivity within a galaxy is the rate of producing gamma ray photons, $d\Gamma_{e^-\gamma\to e^-\gamma}/dE_{\rm em}$ per background photon, multiplied by the ISRF number density, $n_{\rm isrf}$

$$\frac{dq_\gamma}{dE_{\rm em}} = \frac{dN_\gamma}{dV dE_{\rm em} dt} = \int d\epsilon \frac{d\Gamma_{e^-\gamma\to e^-\gamma}}{dE_{\rm em}} \frac{dn_{\rm isrf}}{d\epsilon} \quad . \tag{3.19}$$

Here, the gamma ray rate per unit ISRF photon is a product of the cosmic ray flux and the IC cross section

$$\frac{d\Gamma_{e^-\gamma\to e^-\gamma}}{dE_{\rm em}} = \frac{d\sigma_{e^-\gamma\to e^-\gamma}}{dE_{\rm em}} \phi_{\rm e} \quad . \tag{3.20}$$

that in general takes the Klein-Nishina form. The full Klein-Nishina cross section is a complicated function of the energies involved. Moreover, the inverse Compton process produces anisotropic emission if either the cosmic-ray or ISRF populations depart from isotropy. While

the cosmic-ray electrons of interest are well-approximated as isotropic, in a real galaxy the photon field is certainly anisotropic as well as spatially-varying. These effects are included in GALPROP (Moskalenko & Strong, 2000), but we will ignore them in our simple one-zone galaxy model. In general, an anisotropic ISRF leads to an overall anisotropy in IC [3]. From figures 5(a) and 6(a) of Moskalenko & Strong (2000), the ISRF anisotropy is a $\sim 20\%$ effect in the regions of strong IC emission, i.e., within the diffusion length of a few kpc of the disk. Thus, this effect will not dominate our final error budget.

For the electron spectra we consider, the Thomson limit is a good approximation for CMB and IR photons, but fails for UV and some optical photons. Hence, we use the Klein-Nishina result via the prescription of Jones (1968) and Blumenthal & Gould (1970). This differential cross section is expressed as,

$$\frac{d\sigma}{dE_{\rm em}}(\epsilon, E_{\rm e}, q) = \frac{3}{4}\frac{\sigma_{\rm T}}{\epsilon\ \gamma^2}\left(2q\ \ln(q) + (1+2q)(1-q) + \frac{1}{2}\frac{(\Delta_\epsilon q)^2}{1+\Delta_\epsilon q}(1-q)\right)$$

where the electron Lorentz factor $\gamma = E_e/m_e$ and $\sigma_{\rm T}$ is the total Thomson scattering cross section and q appears in eq. (3.17). In the Thomson limit, the last term in the above equation become negligible.

The inverse Compton volume emissivity within a one-zone galaxy is thus

$$\frac{dq_\gamma}{dE_{\rm em}} = \int d\epsilon \frac{d\Gamma_{e^-\gamma\to e^-\gamma}}{dE_{\rm em}}\frac{dn_{\rm isrf}}{d\epsilon} = \int d\epsilon \frac{dn_{\rm isrf}}{d\epsilon}\int dE_e \phi_e(E_e)\frac{d\sigma_{e^-\gamma\to e^-\gamma}}{dE_{\rm em}} \qquad (3.21)$$

We evaluate the emissivity numerically, by using the ISRF, cosmic ray flux density, and the cross section mentioned above, §3.3 and §3.4. That ISRF density $n_{\rm isrf}$ is the same as in the inverse Compton energy loss equation eq. (3.19), so that we calculate the two self-consistently.

[3] In principle, therefore, a galaxy's IC emission is anisotropic and depends on the galaxy orientation! Of course, the EGB signal will average over many galaxies and thus over all orientations.

It is suggestive to recast the emissivity in eq. (3.21) in the form

$$\frac{dq_\gamma}{dE_{\rm em}} = U_{\rm isrf} \frac{\int d\epsilon \frac{dn_{\rm isrf}}{d\epsilon} \epsilon \left(\frac{1}{\epsilon} \frac{d\Gamma(\epsilon, E_{\rm em})}{dE_{\rm em}} \right)}{\int d\epsilon \frac{dn_{\rm isrf}}{d\epsilon} \epsilon} \equiv U_{\rm isrf} \left\langle \frac{1}{\epsilon} \frac{d\Gamma(\epsilon, E_{\rm em})}{dE_{\rm em}} \right\rangle = U_{\rm isrf} \left\langle \frac{1}{\epsilon} \frac{q_{\rm e}(> E_e)}{b} \frac{d\sigma}{dE_{\rm em}} \right\rangle \tag{3.22}$$

We see that the emissivity can be understood as an effective average over the ISRF energy density distribution. Here, the differential and total ISRF energy densities are $u_{\rm isrf} = \epsilon \; dn_{\rm isrf}/d\epsilon$ and $U_{\rm isrf} = \int d\epsilon \; u_{\rm isrf}$ respectively. We see that the amplitude of the gamma-ray emissivity, q_γ scales as

$$q_\gamma \sim \frac{U_{\rm isrf}}{b} q_e \sim \frac{b_{\rm ic}}{b} q_e$$

and in the Compton dominated regime simply as $q_{\rm e}$ and is independent of the ISRF energy density, $U_{\rm isrf}$. This is a statement of calorimetry. Of course, the gamma-ray spectral shape *does* remain sensitive to the ISRF even in the case of perfect calorimetry.

In reality, synchrotron and bremsstrahlung compete with inverse Compton losses at different energies, as seen in §3.4. In the Thomson regime, the ratio of synchrotron to inverse-Compton losses

$$\frac{b_{\rm sync}}{b_{\rm ic}} \stackrel{\rm Thomps}{\longrightarrow} \frac{U_{\rm B}}{U_{\rm isrf}} = 0.4 \left(\frac{1.1 \text{ eV cm}^{-3}}{U_{\rm isrf}} \right) \left(\frac{B}{4\mu\text{G}} \right)^2 , \tag{3.23}$$

is energy-independent; here the numerical factors are for normal galaxies. For our fiducial magnetic field value, this ratio is not far from unity and hence, the shape does not change much for different parameters describing the ISRF and the magnetic field. On the other hand, for $E_e \gtrsim 1$ TeV, the IC losses are in the Klein-Nishina limit and grow only logarithmically in energy; then the synchrotron losses dominate In this case, we have $q_\gamma \sim (U_{\rm isrf}/U_{\rm mag}) q_e$. Thus, for high-energy cosmic-ray electrons, the calorimetric approximation increasingly breaks down.

For starbursts, the syncrotron-to-IC ratio (eq. 3.23) is $b_{\rm sync}/b_{\rm ic} \simeq 6$ in our fiducial model. Thus, synchrotron losses dominate IC for all electron energies for such high magnetic fields. This decrease in emissivity due to synchrotron losses is partially compensated by the in-

creased star formation rate in starbursts.

The competition among losses depends on the way the interstellar densities evolve with redshift. Short-lived, massive stars dominate most of the ISRF except possibly for some of the optical range, and so the energy density scales with the star-formation rate $U_{\rm isrf} \propto S(z)$. Due to cosmic-ray ion equipartition, we take $U_{\rm mag} \propto S(z)$ as well, and thus the $U_{\rm isrf}/U_{\rm mag}$ ratio doesn't change dramatically throughout the cosmic history. Similarly, we also include a strong evolution $n_{\rm ism} \propto (1+z)^3$ evolution to the interstellar particle density, which increases rapidly towards $z \sim 1$, roughly in step with the cosmic star-formation rate. Thus, the inverse-Compton/bremsstrahlung ratio of energy losses remains roughly constant as well out to $z \sim 1$. The net result is that the spectral shape of inverse Compton emission does not evolve dramatically with redshift in our model.

3.5.2 Total Inverse-Compton Luminosity from a Single Galaxy

As seen in §3.2, knowing the specific inverse Compton emissivity $dq_\gamma/dE_{\rm em}$ within a single star-forming galaxy, we can calculate the specific IC luminosity of the galaxy. Namely,

$$L_\gamma(E_{\rm em}) = \frac{dN_{\gamma,ic}}{dt\, dE_{\rm em}} \quad = \quad \int \frac{dq_\gamma}{dE_{\rm em}} dV_{\rm ISM} \tag{3.24}$$

and we have seen that $q_\gamma \propto (b_{\rm ic}/b_{\rm tot}) q_e$. Following Fields et al. (2010), we take supernovae as the engines of cosmic-ray acceleration. Thus we scale the electron injection rate with the supernova rate, i.e., we have $L_\gamma \sim \int q_e\, dV_{\rm ISM} \propto R_{\rm SN} \propto \psi$. This linear proportionality captures the main dependence of IC emission on star-formation rate.

The single-galaxy IC luminosity takes the separable form

$$L_\gamma(\psi, z) = \frac{\psi}{\psi_{\rm gal}} L_{\rm gal}(z) \tag{3.25}$$

where we have suppressed the energy dependence for clarity. Here we explicity display the dominant sensitivity to star-formation, via the overall linear proportionality to the star-

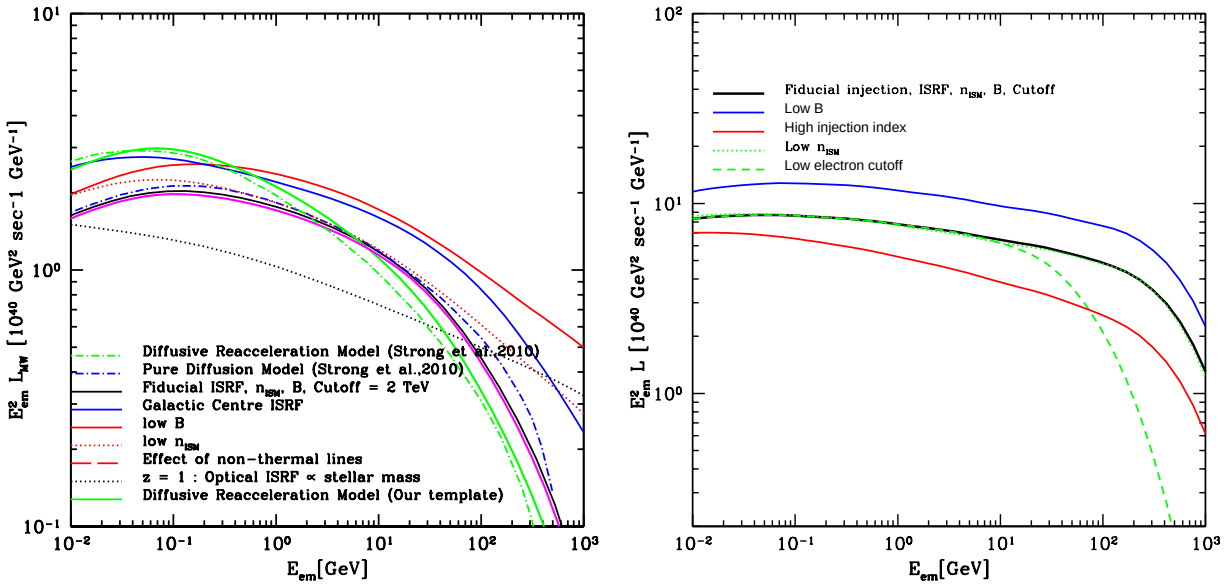

Figure 3.2: The inverse-Compton gamma-ray luminosity spectrum for our single-galaxy templates. *(a) Left: Milky-Way template for normal galaxies.* The solid black curve represents our fiducial model, with an ISM density $n_{\rm H\ I,0} = n_{\rm H\ II,0} = 0.06$ cm^{-3}, magnetic field $B_0 = 4\ \mu$G with a cutoff in the cosmic ray spectrum at 2 TeV. This is for the ISRF consistent with $(R, h) = (0, 5)$ kpc. This model is designed to provide a good fit to the GALPROP Plain Diffusion model of Strong et al. (2010, dot-dashed blue curve). The solid red curve shows the effect of reducing B to 2 μ G. The dotted red curve is for $n_{\rm H\ I,0} = n_{\rm H\ II,0} = 0.03$ cm^{-3}. The red dashed is includes the effect of non-thermal lines in the ISRF. The solid blue shows the single galaxy template for the Galactic Centre, with $n_{\rm H\ I,0} = n_{\rm H\ II,0} = 0.12$ cm^{-3}, and $B_0 = 8.3\ \mu$G. Comparison of the Diffusive reacceleration case with GALPROP with our one-zone template that fits it is shown in green. The black dotted curve shows effect of the modifying the optical component of the ISRF to include effect of finite lifetime of stars. *(b) Right: M82 template for starburst galaxies.* The fiducial curve for M82 type starburst is shown in black with $n_{\rm H\ I,0} = n_{\rm H\ II,0} = 300$ cm^{-3}, $B = 300\ \mu$G, and a cutoff at 2 TeV. And the ISRF is shown by the thick black curve in Fig. 3.1. And the magenta curve here corresponds to the ISRF with higher IR temperature also shown in magenta. Variations in B, n, and spectral index are shown by the blue, green and red curves respectively.

formation rate. The Milky-Way model $L_{\rm MW}(z)$ is for a galaxy with the present-day Milky-Way star-formation rate, but allowing for redshift evolution of the interstellar matter and radiation densities. Starbursts follow similar scalings, but are tied to M82.

Figure 3.2(a) shows our IC luminosity models for $z = 0$ for normal galaxies, along with that of Strong et al. (2010). Our fiducial model described in §3.3, §3.4 and §3.5.1 is represented by the solid black curve. The main feature of the inverse Compton $E_{\rm em}^2 L_{\rm MW}$ spectrum is that it has a broad maximum corresponding to the break in the electron injection spectrum at $E_{e,\rm break} = 4$ GeV. In our the fiducial model, the optical component dominates the ISRF, and thus we expect the injection peak to correspond to an IC peak at $E_{\rm em} \approx \gamma^2 \epsilon \approx 100$ MeV. This is close to what we find in our fiducial model, and is consistent with the GALPROP results.

Our fiducial Milky Way model does a good job of reproducing the IC results of Strong et al. (2010), over most of the *Fermi* energy range. Thus, our results are equivalent to normalizing to the GALPROP luminosity for normal galaxies with the Milky Way's star formation rate. A fitting function for our fiducial IC model appears below in Table 3.3; the fit is good to better than 2% over the *Fermi* energy range. From this fit we see that at 1 GeV the logarithmic slope is around -0.1, so that $L_{\rm MW} \sim E_{\rm em}^{-2.1}$. This is considerably flatter than both the pionic spectrum and the observed EGB at these energies.

Fig. 3.2(a) presents other curves that illustrate the sensitivity of our model to the input parameters. The resulting trends can be understood in terms of the competition among the different electron energy losses in the electron propagation through to the resulting IC spectrum. For example, decreasing the gas density suppresses the bremsstrahlung losses relative to the total. This increases the ratio of $b_{\rm ic}/b_{\rm brem}$, which governs the IC spectral shape at lower energies. The result is a boost in the IC output at lower energies, which also shifts the IC peak towards lower energies. At high gamma-ray energies beyond $\sim few$ GeV, synchrotron losses dominate, and thus the ratio $b_{\rm ic}/b_{\rm sync}$ controls the spectrum; thus we find that reducing the magnetic field increases the luminosity.

The choice of ISRF is also important. Our fiducial model adopts an ISRF consistent with the GALPROP $(R, h) = (0, 5)$ kpc emission, as it best reproduces the IC luminosity of (Strong et al., 2010). If we change the ISRF to that of the Galactic centre, the IC signal is amplified, and the peak shifts to lower energies, as shown by the solid blue curve in Fig. 3.2(a). At the Galactic centre, the magnetic energy density is increased by a factor of 4 relative to the fiducial case, but the photon energy density goes up by more than a factor of 10. So both the fractions, $b_{\rm ic}/b$ and $b_{\rm sync}/b$ are higher, but so is $b_{\rm ic}/b_{\rm sync}$. And so the peak occurs at a lower energy, but has a greater amplitude. We included the effect of non-thermal lines in the ISRF, using the GALPROP spectral form. We find that there is only a minor effect on the galactic luminosity as shown by the red dashed curve in Fig. 3.2(a).

Finally, we show the effect of different redshift evolution of the optical ISRF component. Namely, the blue dotted curve in Fig. 3.2(a) shows the results if the optical component is dominated by long-lived stars. In this model the luminosity scales with stellar mass rather than star-formation rate: $L_\gamma \propto L_{\rm bg} \propto M_\star$. Compared to our fiducial case, the ISRF shape is still similar (same red stars), but the redshift history of $L_\gamma(z) \propto M_\star(z)$ is different because $\rho_\star(z)$ builds up more slowly than $\dot{\rho}_\star(z)$. We see from Fig. 3.2(a) that fixing our single galaxy template to $z = 1$ at the peak of star formation activity, reduces the galactic luminosity due to lower stellar mass.

Thus, there are several uncertainties in our simple model of the gamma ray spectrum for a single, Milky-Way like galaxy, such as choice of the average ISRF, the electron density, and the interstellar magnetic field. However, for reasonable interstellar models, these all lead to modest changes in the normalisation of the luminosity in the Fermi energy range, at most tens of percent.

Larger changes would be possible if one were to depart from the single galaxy template in Strong et al. (2010), which we try to reproduce and that is based on a wealth of Milky-Way data. Allowing oneself sufficient freedom, the inverse Compton EGB signal can be adjusted by changes, e.g., in the $U_{\rm isrf}/U_{\rm B}$ and $U_{\rm isrf}/n_{\rm ism}$ ratios that control the degree of

electron calorimetry. Of course, this would then drive the system away from the rough energy equipartition observed in the Milky Way. Even then, large increases in these ratios would only increase the completeness of electron calorimetry and would raise the IC signal by a factor $\lesssim 2$; on the other hand, large decreases in these ratios would spoil calorimetry and could substantially lower the IC luminosity. Thus, the cosmological prediction of the IC contribution of the star-forming galaxies to the EGB should be fairly robust, unless there are departures from the equipartition implicit in the Milky-Way-based normalization.

We turn now to the template for starbursts, which we based our models of M82. The starburst GeV gamma-ray emission shown Fig. 3.2(b) is characterised by the lack of a peak, because the underlying electron spectrum is a single power law lacking a break. The overall normalisation of the fiducial model shown by the black curve is essentially a result of the contest between the higher star formation rate and the lower fraction of IC losses as expressed by,

$$\frac{L_{\rm normal}}{L_{\rm SBG}} \approx \left(\frac{\psi_{\rm MW}}{\psi_{\rm M82}}\right)\left(\frac{U_{\rm isrf,MW}}{U_{\rm isrf,M82}}\right)\left(\frac{U_{\rm isrf,M82}+U_{\rm B,M82}}{U_{\rm isrf,MW}+U_{\rm B,MW}}\right) \tag{3.26}$$

, assuming the acceleration e/p ratio is the same for normals and starbursts. Equation 3.26 predicts that an M82-type starburst show have an IC luminosity that is a factor ~ 3.6 larger than our Milky-Way template, which is in agreement with the results show in Fig. 3.2(a) and (b). Moreover, the differences in the Fig. 3.2(b) curves for different M82 parameters can be understood in the same way as the same trends in B, $n_{\rm ism}$ and ISRF discussed above for the Milky-Way template.

The M82 template emission at GeV energies is a factor of few higher compared to the Milky Way template. However, the M82 emission is proportional to its star-formation rate, which is higher than that of the Milky Way by a factor ~ 8. Thus, emission per unit star formation $(L/\psi)_{\rm template}$ ratio is *lower* for M82 and thus for our starburst template. This ratio provides the proportionality constant in our scaling law $L = (L/\psi)_{\rm template}\psi$. In this sense

therefore, starbursts are less efficient IC emitters per unit star formation. The major sources of uncertainty for starbursts are the magnetic field strength, and the injection e/p ratio–if it is indeed different for starbursts as suggested by Lacki et al. (2012).

3.6 Results: Inverse Compton Contribution to the Extragalactic Background

Having established a one-zone galaxy template, and explored physically plausible variations in it, we proceed to compute the IC contribution to the EGB measured by *Fermi*-LAT from star-forming galaxies. This is given by the well-known expression

$$I_E = \frac{c}{4\pi} \int (1+z) \left| \frac{dt}{dz} \right| \mathcal{L}_\gamma[(1+z)E, z] \; dz \tag{3.27}$$

with $|dt/dz| = (1+z)^{-1} \left[(1+z)^3 \Omega_{\rm matter} + \Omega_\Lambda\right]^{-1/2} H_0^{-1}$. Here we assume a flat ΛCDM universe with $H_0 = 71$ km s^{-1} Mpc^{-1}, $\Omega_{\rm matter} = 0.3$, and $\Omega_\Lambda = 0.7$, following Fields et al. (2010).

The cosmic IC luminosity density (i.e,. cosmic volume emissivity) is given by substituting our single-galaxy luminosity of eq. (3.25) into the luminosity function of eq. (3.2). Because we have $L_{\rm ic} \propto \psi$, the IC emission of a star-forming galaxy traces its star-formation rate. Thus, the IC luminosity function $dn_{\rm gal}/dL_\gamma$ at each redshift is proportional to the luminosity function of *any* tracer of star formation at that redshift. We explicitly distinguish for both normal and starbursts over cosmic time. Suppressing the energy dependence for clarity, we have

$$\begin{aligned}
\mathcal{L}_\gamma(z) &= \int L_\gamma \, \frac{dn_{\rm gal}}{dL_\gamma} \, dL_\gamma \\
&= \frac{L_{\rm norm}(z) f_{\rm norm}(z)}{\psi_{\rm MW}} \int \psi_{\rm norm} \frac{dn_{\rm gal}}{dL_\gamma} \, dL_\gamma + \frac{L_{\rm sbg}(z)(1 - f_{\rm norm}(z))}{\psi_{\rm M82}} \int \psi_{\rm sbg} \frac{dn_{\rm gal}}{dL_\gamma} \, dL_\gamma \\
&= \frac{\dot\rho_{\star,{\rm norm}}(z)}{\psi_{\rm MW}} L_{\rm norm}(z) + \frac{\dot\rho_{\star,{\rm sbg}}(z)}{\psi_{\rm M82}} L_{\rm sbg}(z)
\end{aligned} \tag{3.28}$$

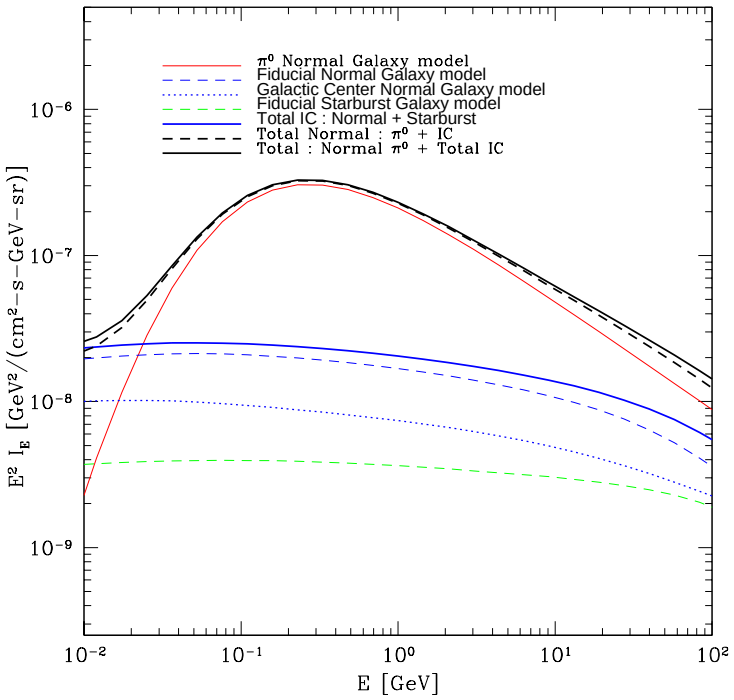

Figure 3.3: The inverse-Compton EGB intensity from star-forming galaxies as a function of energy. The solid blue curve represents our fiducial IC model summing contributions from normals and starbursts shown in dashed blue and green respectively using single galaxy models of each shown in Fig. 3.2 where interstellar densities evolve with redshift. The dotted blue curve is for an evolving single normal galaxy template with an ISRF corresponding to the Galactic centre model. The red curve shows the pionic signal from normal star-forming galaxies only as in Fields et al. (2010). The dashed black curve shows the total contribution from normal galaxies ignoring starbursts. The dashed green shows IC contribution of M82 type starbursts alone. It is a factor of a few less than that from normals. The solid black curve shows the sum total of normal pionic and total star forming IC.

where the $\dot{\rho}_\star = \langle \psi \, n_{\rm gal} \rangle = \int \psi \, dn_{\rm gal}/dL_\gamma \, dL_\gamma$ is the cosmic star-formation rate. Here $f_{\rm norm}(z)$ is the fraction of norml star-forming galaxies at redshift, and $1 - f_{\rm norm}(z)$ the starburst fraction. We calculate this as in (Fields et al., 2010), where starbursts are taken to be galaxies with a star-formation surface densities $\dot{\Sigma}_\star > 0.4 \; M_\odot \; yr^{-1} \, kpc^{-2}$ (Kennicutt, 1998); this gives $f_{\rm norm}(0) \approx 1$ at $z = 0$, declining as redshift increases, with $f_{\rm norm}(1) = 0.68$ at $z = 1$. Following Fields et al. (2010) we adopt the Horiuchi et al. (2009a) cosmic star-formation rate, and a Milky Way star-formation rate $\psi_{\rm MW} = 1.07 M_\odot/{\rm yr}$ (Robitaille & Whitney, 2010). For M82, we use $\psi_{\rm M82} = 8.0 M_\odot/{\rm yr}$, consistent with Sanders et al. (2003); Lacki et al. (2012).

The overall amplitude of the cosmic IC luminosity density is thus linearly proportional to the cosmic star-formation rate. Of course, the detailed spectral shape of the luminosity density reflects redshift dependence of the interstellar matter and radiation encoded in $L_{\rm MW}(z)$.

Figure 3.3 shows the IC contribution to the EGB for some choices of the Milky-Way spectrum $L_{\rm MW}$ and also the fiducial M82 template, $L_{\rm M82}$. We focus first on the results for the fiducial model, which appear as the solid black curve, and incorporate the full redshift-dependence of interstellar density encoded in $L_{\rm MW}(z)$. A fitting function for the fiducial model appears in Table 3.3, valid over the *Fermi* energy range. For comparison, Fig. 3.3 shows the pionic contribution in red. In our fiducial model, the IC contribution is about 10% of the pionic contribution at the ~ 300 MeV peak in $E^2 I$; growing to about 20% at 10 GeV. This is consistent with our expectations from the order-of magnitude calculations of §3.2.

The shape of the fiducial IC curve is rather smooth, and rather flat in $E^2 I$. This is because the spectrum it is a redshift-smeared version of the single-galaxy IC emission. This stands in contrast to the pionic curve that displays its characteristic peak and a steep $\sim E^{-s_p}$ dropoff at large energies, with $s_p = 2.75$ the propagated proton spectral index.

The bulk of the ficucial IC signal comes from redshifts at the peak of the EGB integrand in eq. (3.27). This occurs at $z_{\rm peak} \sim 1$. A comparison of the corresponding curves in Figs. 3.2

and 3.3 shows that the IC peak in the galaxy luminosity rest-frame energy $E_{\rm em} \simeq 100$ MeV is transformed into an EGB IC peak at $\simeq 40$ MeV. This translation in energy space is consistent with redshifting by a factor $1 + z_{\rm peak}$.

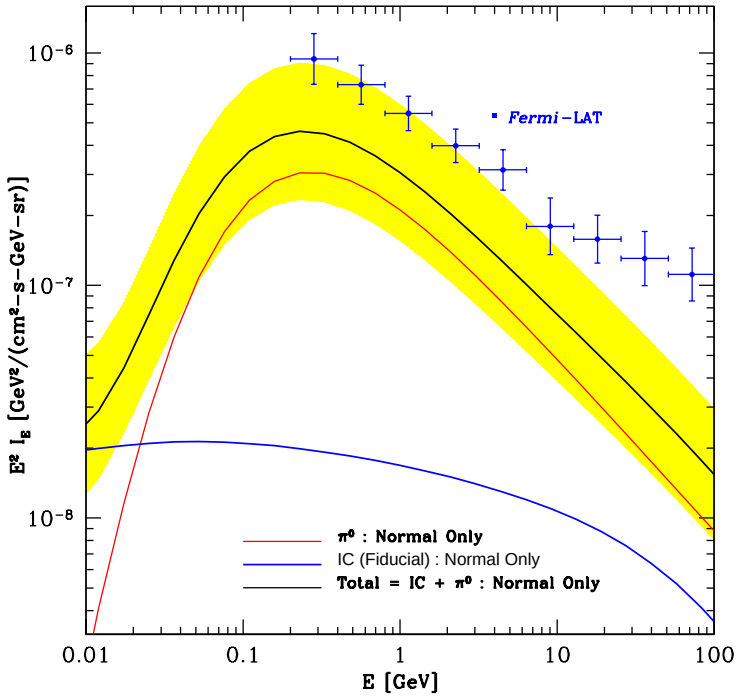

Figure 3.4: A summary of the star-forming galaxy contributions to the EGB intensity, shown as a function of energy. The blue points represent the *Fermi*-LAT data points (Abdo et al., 2010k). The solid red and blue curves show the gamma ray intensity due to pionic and fiducial IC components from star-forming galaxies as in Fig. 3.3. The solid black curve represents the sum of the two. The shaded yellow band gives our estimate of the uncertainty in the predicted total signal, which is dominated by systematic errors that are common to the IC and pionic components.

Our fiducial model sums the emission from normal and starburst galaxies; the contributions from each of these star-formation modes are shown separately in Fig. 3.4. The dashed blue curve shows the EGB signal from normal galaxies, which we see dominates the total IC contribution. The IC component from starbursts is shown in dashed green, and is lower than the normal galaxy contribution by a factor $\sim 2-4$. This suppression arises for two reasons. First, we found that the starburst photon output $(L/\psi)_{\rm template}$ per unit star formation is

lower than that of normal galaxies. In addition, the fraction of galaxies that are starbursts is small today, and while this fraction grows with redshift, it is still subdominant at $z \sim 1$ where the EGB contribution peaks.

The dashed black curve in figure 3.3 represents the total contribution of normal galaxies to the EGB, summing their pionic and IC contributions. Adding the starburst IC model leads to the solid dashed curve showing minor increase at the energies beyond 100 GeV. Now, this computation does not include contribution of pionic emission from starbursts, which has large uncertainties, (eg., Lacki et al., 2012; Paglione & Abrahams, 2012). Indeed, some have argued that pionic emission from starbursts makes a small contribution to the EGB (e.g., Stecker & Venters, 2011), some models predict starburst contributions should saturate the observe EGB (e.g., Lacki et al., 2012). It is worth mention that the uncertainties in the starburst IC contribution are smaller than in the pionic case, largely because the electron propagation is controlled by calorimetry in both the normal and starburst cases. Of course, the starburst IC contribution is still rather uncertain, particularly if the the e/p injection ratio in starbursts is much higher that observed in the Milky Way (Lacki et al., 2012; Paglione & Abrahams, 2012).

Figure 3.2 includes curves which illustrate the parameter sensitivy of our IC results. To give a sense of the effect of the adopted ISRF, we have computed the IC EGB resulting from an evolving ISRF whose spectral shape is appropriate for the Galactic centre. This model corresponds to the dotted blue curve in Fig. 3.2(a). Here again, the main result is that the curves are very similar. In detail, the Galactic centre has a slightly higher ratio $U_{\rm isrf}/U_{\rm mag}$ of starlight-to-magnetic energy density. Thus, electron energy losses are more IC dominated, and finally the overall IC flux is closer to calorimetric and so slightly higher.

Our fiducial model assumes the ISRF components (other than the CMB) are dominated by short-lived stars and thus have a redshift evolution that scales with the cosmic star-formation rate. An extreme alternative is that the optical ISRF is dominated by long-lived main sequence stars whose energy density scales with the stellar mass and thus the integrated

cosmic star-formation rate, as in eq. (3.11). Adopting this scenario, we have calculated the IC contribution to the EGB. For clairty, we have omitted the curve from Fig. 3.3. but it is somewhat smaller than the fiducial model across all energies. This is easily understood: at high redshifts the star-formation rate is higher than today, but the stellar mass is lower and thus offers less optical photons and reduced calorimetry. But the effect is not dramatic; even in this extreme case, the reduction in the IC signal is less than a factor of two relative to our fiducial model.

Thus, we see that the IC results do depend on the adopted interstellar densities and their redshift evolution. But for reasonable choices, the variations in the final IC EGB result are $\approx 10^{\pm 0.3}$. The IC calculation in this sense appears rather robust to the systematic uncertainties in the modeling.

It is useful to compare the IC luminosity density in eq. (3.28) with that for pionic emission. As noted above, the cosmic IC emissivity is proportional to the cosmic star-formation rate, along with a weak sensitivity to the redshift evolution of interstellar densities. In contrast, the Fields et al. (2010) pionic emission depends on the product of cosmic star-formation rate and mean interstellar gas mass, via the nonlinear scaling $L_\pi \sim \psi^{1+\omega}$ with $\omega = 0.714$. Thus, the pionic emissivity represents a different moment of the cosmic star-formation rate $\mathcal{L}_\pi = \langle L_\pi n_{\rm gal} \rangle \sim \langle \psi^{1+\omega} n_{\rm gal} \rangle$. This nonlinear moment gives different results depending on how the star-formation distribution evolves with redshift. Two extreme limits correspond to: (a) pure density evolution, wherein galaxies have constant star-formation rates but evolving number density; versus (b) pure luminosity evolution in which the star-forming galaxy density is constant but the star-formation rates all evolve with redshift. The pionic curves we show correspond to the fiducial Fields et al. (2010) pure luminosity evolution case, which gives a contribution to the EGB larger by a factor ~ 3 than in the pure density evolution case. In the IC calculation, the pure luminosity and pure density evolution are degenerate, in that these models all give the same cosmic star-formation rate and thus the same IC output.

Figure 3.4 represents the central result of this paper, summarizing the EGB predictions

for gamma-ray emission from star-forming galaxies in the *Fermi* energy range. We show the fiducial IC curve from Fig. (3.3), the fiducial normal-galaxy pionic model of Fields et al. (2010), and the total EGB intensity that sums these components. Over the 100 MeV to 300 GeV range, the pionic component dominates the normal galaxy contribution. But as we have seen, the IC curve is a much flatter function of energy. The IC component thus becomes systematically more important at higher energies. Consequently, high-energy slope of the total emission is less steep than that of the pionic signal, and closer to the *Fermi*-LAT data shown in blue (Abdo et al., 2010k).

Including the IC emission thus improves somewhat the agreement between star-forming prediction and the observed EGB slope, a weaker point of the Fields et al. (2010) pionic-only model. Up to about $\sim$ 10 GeV, the central values of the model fall below the data, but are consistent within the theoretical and observational error budget (discussed below). At higher energies, the model underpredicts the data. Our pionic model neglects starburst galaxies; it may well be that their pionic emission is important at this energy range (e.g., Lacki et al., 2011). In addition, other unresolved sources (Strong et al., 1976a,c) such as blazars (e.g., Padovani et al., 1993; Stecker et al., 1993; Mücke & Pohl, 2000; Stecker & Venters, 2011) and other active galaxies (e.g., Grindlay, 1978; Kazanas & Protheroe, 1983), starbursts (Thompson et al., 2007) are also guaranteed to play a role . In any case, star-forming galaxies clearly are an important contribution to the *Fermi* EGB signal, and could well be the dominant component.

Note also that the IC curve does not become important at *low* energies until far below the pion bump. Thus, the Fields et al. (2010) conclusions stand: the pion feature should still remain as a distinguishing characteristic of a significant star-forming contribution to the EGB. Measurements below $\sim$ 200 MeV should show a break in the EGB slope if star-forming galaxies play an important role. Such a spectral feature provides one way to discriminate between star-forming galaxies and other sources, such as the guaranteed contribution from unresolved blazars.

Table 3.3: Fitting Functions

Form: $Y = 10^{aX^3+bX^2+cX+d}$, with $X = \log_{10}(E/1\,\mathrm{GeV})$					
Y		a	b	c	d
$E_{\rm em}^2 L_{\rm normal}(E_{\rm em})$	[GeV s^{-1}]	-2.51×10^{-2}	-5.03×10^{-2}	-9.49×10^{-2}	40.246
$E^2 I_{\rm normal}(E)$	[GeV cm^{-2} s^{-1} sr^{-1}]	-1.53×10^{-2}	-7.38×10^{-2}	-0.130	-7.63
$E_{\rm em}^2 L_{\rm starburst}(E_{\rm em})$	[GeV s^{-1}]	-9.16×10^{-3}	-7.38×10^{-3}	-5.41×10^{-2}	40.888
$E^2 I_{\rm starburst}(E)$	[GeV cm^{-2} s^{-1} sr^{-1}]	-2.37×10^{-3}	-2.59×10^{-2}	-6.29×10^{-2}	-7.86

Our estimate of the uncertainty in the total normal galaxy emission is represented by the shaded band in Figure 3.4. The errors in the pionic contribution dominate, and are taken from Fields et al. (2010). For the IC contribution, the errors are dominated by systematic uncertainties in the Milky-Way star formation rate $\psi_{\rm MW}$ and in the normalization $\dot{\rho}_\star(0)$ of the cosmic star-formation rate that are both $\sim 40\%$ (Fields et al., 2010). These factors are common to the overall normalizations of *both* the pionic and IC signals, cf. eq. (3.28). The effect of the uncertainties in the parameters magnetic field and interstellar densities on the normal IC emissivity is estimated from variation in the curves in Fig. 3.2(a) to be $\sim 50\%$. We propagate the errors in IC and pionic emissivities and the common errors in star formation rates, to construct the yellow band in Fig. 3.4. Because the pionic signal dominates the total, it also dominates the total error, and the uncertainty in the IC calculation does not change the result much except at the very highest energies where other systematics may be important.

We have ignored the effect of intergalactic absorption of the high-energy gamma rays via $\gamma\gamma_{\rm ebl} \rightarrow e^+e^-$ photo-pair production in collisions with extragalactic background light (e.g., Salamon & Stecker, 1998; Abdo et al., 2010e; Stecker et al., 2012). This attenuation starts to become significant for gamma rays over few tens of GeV. Therefore, beyond these energies our results will be suppressed by amounts that depend on the optical depth for these high-energy gamma rays. In this context it is worth noting that *Fermi*-LAT observations of the $z = 0.9$ active galaxy, 4C +55.17 do not show significant absorption of gamma rays

up to about 100 GeV (McConville et al., 2011). This object lies within the $z \sim 1$ regime where most of the IC contribution to the EGB occurs; thus we might expect that attenuation should be mild at *Fermi* energies. Recall also that at high energies, the electron propagation should include catatrophic losses from IC interactions, which have not been included in our calculations.

3.7 Discussion and Conclusions

We have calculated the contribution to the extragalactic gamma-ray background due to inverse-Compton emission from star-forming galaxies. To do this we model the IC emission in individual star-forming galaxies, which arises from cosmic-ray electron interactions with the ISRF. For normal star-forming galaxies, we normalize to the present-day Milky Way IC luminosity as determined by GALPROP (Strong et al., 2010). For starbursts, we use the M82 template guided by observations (de Cea del Pozo et al., 2009) and other results (Lacki et al., 2012; Paglione & Abrahams, 2012). We also provide a prescription for redshift evolution of interstellar matter and energy densities, based on equipartition arguments. Assuming cosmic rays are accelerated by supernovae implies that a galaxy's IC luminosity scales as $L_{\rm ic} \propto \psi$; this further implies that the cosmic IC luminosity density or volume emissivity is proportional to the cosmic star-formation rate: $\mathcal{L}_\gamma \propto \dot{\rho}_\star$.

This linear dependence of IC luminosity with star-formation rate has important implications in light of the star-forming galaxies *resolved* by *Fermi*. Namely, the $L_{\rm ic} \propto \psi$ trend provides a poor fit for *Fermi* galaxies, for which the observed correlation is non-linear: $L_{\rm ic} \propto \psi^{1.4\pm0.3}$ (e.g., Abdo et al., 2010f). This implies that the IC component is subdominant in *Fermi* galaxies, adding indirect evidence for the primacy of pionic emission in star-forming galaxies and prefiguring the trends we find for the EGB.

Turning to the EGB, we find that the IC contribution has a very broad maximum in $E^2 I_{\rm ic}$ at $E \simeq 40$ MeV, falling off very gradually away from this peak. This shape is a

redshift-smeared reflection of the underlying Milky-Way-like spectrum from the individual galaxies. In fact, the IC emission is so broadly peaked that is it effectively featureless. This contrasts markedly with the distinctive pionic feature from cosmic-ray hadronic interactions in star-forming galaxies.

The amplitude and shape of the IC contribution to the EGB depends on the nature of the interstellar radiation and matter fields, and their evolution with redshift. However, we find that when we adopt different but physically motivated variations to our fiducial model, the final EGB predictions change relatively little. This rough model-independence of the IC EGB is a consequence of partial calorimetry, i.e., the fact that IC photons represent a substantial fraction of cosmic-ray electron energy loss, so that the IC output is tied to cosmic-ray production via energy conservation.

We find that in all of our models the IC signal is always smaller than the pionic contribution. However, while this is true, IC also has a substantially flatter spectrum, so that the IC becomes increasingly important away from the pionic peak. This implies that, at least for normal star-forming galaxies, the IC contribution should dominate over pionic at high and low energies. For normal star-forming galaxies, one-zone models for scale heights $h < 2$ kpc IC can exceed pionic in a narrow window about TeV energies at the high end and below 100 MeV at the low end. However, at higher energies the opacity of the universe becomes important and losses become catastrophic, and requires different techniques to handle correctly. At energies below the *Fermi*-LAT range, the IC emission will be supplemented by processes such as bremsstrahlung, which we have not included; a detailed treatment of the MeV regime appears in Lacki et al. (2012).

The approximate calorimetric relationship between IC photons and cosmic-ray electrons has important consequences. The main redshift dependence of the cosmic IC emissivity is a linear dependence on the cosmic star-formation rate. Thus, our results are independent of whether the cosmic star-formation rate is a result of pure luminosity evolution, pure density evolution, or something in between. This is in contrast to the pionic case, which depends

nonlinearly on the star-formation luminosity function and so breaks the degeneracy between the pure luminosity and pure density evolution cases.

Our IC results for normal and starburst galaxies share important similarites. In both cases fractional calorimetry controls the basic scaling with star-formation rate, and leads to similarly broad spectral features that are not very different from power laws. While the M82 starburst template has a higher gamma-ray luminosity than the corresponding Milky-Way normal galaxy template, the photon output $(L/\psi)_{\rm template}$ per unit star formation is *lower* for starbursts. For this reason, and becuase of the relative rarity of starburst galaxies, the IC contribution to the EGB is dominated by that of normal galaxies. However, the starburst model has fewer observational constraints and thus larger uncertainties. The starburst IC contribution could become very important if, for example, the e/p injectio n ratio is very large in starbursts Lacki et al. (2012).

To simplify the discussion, the IC and pionic models presented here neglected the effects of Type Ia supernovae, implicitly assuming instead that all supernovae in star-forming galaxies are due to core-collapse. Lien & Fields (2012) considered in detail the effect of Type Ia supernovae on the pionic signal. They found that a self-consistent treatment includes both the addition of Type Ia explosions as cosmic-ray accelerators, but also as part of the Milky-Way normalization of the cosmic-ray/supernova ratio. The effects largely cancel, so that in the end, the net pionic galactic luminosity and EGB does not change substantially. In the case of IC emission a similar cancellation will occur. The only new contribution of possible importance comes from Type Ia explosions arising from long-lived progenitors in quiescent (i.e., not actively star-forming) galaxies such as ellipticals. Lien & Fields (2012) show that the pionic emission from these systems could be large if they have a substantial reservoir of hot, X-ray-emitting gas. But supernova rate in these galaxies represents a subdominant fraction of cosmic Type Ia activity, which itself is substantially smaller than the cosmic core-collapse rate. Thus, the IC contribution from these systems will be small. And so inclusion of Type Ia supernovae in a self-consistent way would change our results very little, less than

the uncertainties in the model.

There remains room to improve on our model. Future work would benefit from observational progress in clearly identifying an IC signal from individual star-forming galaxies, at energies away from the pionic peak. Theoretical work would benefit from a more detailed model for the ISRF and its evolution, and from the use of additional multiwavelength constraints on the cosmic ray electrons.

More broadly, a solid identification and quantification of the main components of the EGB remains a top priority for gamma-ray astrophysics and particle cosmology. Extending the *Fermi* EGB energy spectrum to both higher and lower energies will provide important new constraints. At sufficiently high energies, the cosmic opacity due to photo-pair production must become apparent if the EGB is dominated by *any* sources at cosmological distances (e.g., Salamon & Stecker, 1998; Abdo et al., 2010e; Stecker et al., 2012). And at energies just below those reported in Abdo et al. (2010k), a break in the EGB spectrum is an unavoidable prediction if the signal is dominantly unresolved pionic emission from star-forming galaxies (both normal and starbursts). An independent probe of EGB origin lies in anisotropy studies (Ando & Komatsu, 2006; Ando & Pavlidou, 2009; Hensley et al., 2010; Ackermann et al., 2012a; Malyshev & Hogg, 2011). Regardless of the outcome, an assay of the EGB components will provide important new information (and perhaps some surprises!) about the high-energy cosmos.

3.8 Acknowledgements

It is a pleasure to acknowledge stimulating conversations with Keith Bechtol, Vasiliki Pavlidou, Troy Porter, Tijana Prodanović, Amy Lien, Andy Strong, Todd Thompson, and Toni Venters. After our paper was first submitted, we benefitted greatly from discussions with Brian Lacki regarding his similar work. BDF would also like to thank the participants of the 2012 Sant Cugat Forum on Astrophysics for many lively and enlightening discussions.

This work was partially supported by NASA via the Astrophysics Theory Program through award NNX10AC86G.

Chapter 4

Statistics of gamma-ray sources

This chapter is an outlines a work in progress with co-authors Eric Baxter (first author), Scott Dodelson and Brian Fields.

There is great debate about the relative contribution of various gamma-ray emitting sources to the diffuse EGB. The way to resolve this is to study the various distinguishing properties of these sources as their gamma-ray spectral slope ,angular anisotropy in the source distribution, correlation with other wavelengths, etc. The statistics of the photons themselves bear a signature of the sources producing them. There are a number of candidates that contribute to the diffuse EGB. AGNs, star forming galaxies, pulsars, etc. are examples of known astronomical sources. In addition, there is possibility of unknown or exotic sources contributing to the EGB. The most exciting possibility is the contribution from particle dark matter via decays and annihilations producing gamma-rays. The known astronomical sources would be foregrounds to this. Thus it is, crucial to model them accurately not only in order to understand them but also to seperate them from a possible signature of dark matter.

For e.g., AGNs are fewer and brighter individually. Amongst these are blazars, AGNs whose jets point towards us. They are the dominant source class in the gamma-ray emitting point source catalog (Nolan et al., 2012a). Star forming galaxies on the other hand are far more numerous, but individually dim. Thus, one expects them to have a different photon distribution. The gamma-ray emissivity, q_γ of a distribution of sources can be given as,

$$q_\gamma = n_\gamma L_\gamma \tag{4.1}$$

Blazars have a number density of $n_\gamma \sim 10^{-9}\text{Mpc}^{-3}$ and an average luminosity, $L_\gamma \sim 10^3\text{photons sec}^{-1}$. Compared to this the star forming galaxies on the other hand have $n_\gamma \sim 10^{-3}\text{Mpc}^{-3}$ and $L_\gamma \sim 10^6\text{photons sec}^{-1}$. This rough estimate suggests that the emissivity from a distribution of few, bright blazars is comparable to that from a distribution of numerous, but dim star forming galaxies.

A detailed analysis of statistics of source photon counts distribution however, has the potential to reveal the true relative contribution of these sources. This is undertaken in Baxter, Chakraborty, Dodelson and Fields,.(in prep). An method based on extension of the P(D) analysis described in (Scheuer, 1957) is used to analyse the photon counts from *Fermi* -LAT. The quantity of interest here is the probability $P_\text{i}(C)$ of finding C_i photons in the pixel i of the sky. The individual $P_\text{i}(C)$ of the different contributing source types here are determined from their redshift-dependent luminosity functions. The luminosity functions of five different source types including the two classes of gamma-ray emitting blazars, are used namely

1. Star forming galaxies (SFGs)
2. Flat Spectrum Radio Quasars (FSRQs)
3. BL Lacertae Objects (BL LACs)
4. Dark matter annihilation from Galactic subhalos
5. Diffuse emission from the Galaxy

4.1 Formalism

From the luminosity function $\frac{dn}{dL}$ of a source type, the differential source flux distribution $\frac{dn}{dF}$ is computed. This is an observed quantity. Of course, what is really computed is the

probability of observing flux F, from a single source along the line of sight, $P_1(F)$ as,

$$P_1(F) \propto \int dz dL \frac{d_L^2}{(1+z)^2 E(z)} \frac{dn_c}{dL} \delta\left(F - \frac{L(1+z)^{-(\alpha-2)}}{4\pi d_L^2}\right) \tag{4.2}$$

$$= \int_{z(L_{min},F)}^{z(L_{max},F)} dz \frac{d_L^4 (1+z)^{(\alpha-2)}}{(1+z)^2 E(z)} \left.\frac{dn_c}{dL}\right|_{L=4\pi d_L^2 F(1+z)^{(\alpha-2)}} \tag{4.3}$$

where d_L is the standard luminosity distance. And the delta function ensures that the flux is F for a source of luminosity L at d_L. The underlying assumption here is that sources have a power law spectral energy distribution, an assumption good enough for star forming galaxies and blazars in the regime of interest. $z(L_{min}, F)$ and $z(L_{max}, F)$ are the redshifts expressed as functions of the minimum and maximum, luminosity L_{min} and L_{max}, respectively, that produce observed fluxes F. The source flux distribution $\frac{dn}{dF}$ is related to this by,

$$\frac{dn}{dF} = \mu P_1(F) \tag{4.4}$$

where μ is the mean number of sources per unit solid angle along the line of sight.

Having determined $P_{1,a}$ for each source type a, the probability of measuring a sum total flux F of all the source types, i.e. the flux probability distribution is the convolution of the individual $P_{1,a}$.

$$P(F) = P_{1,a} \star P_{1,b} ..... \star P_{1,z} \tag{4.5}$$

In reality LAT observations constitute discrete photon counts. The continuous flux probability is related to the discrete photon count probability in a particular pixel i via the exposure in that pixel as

$$P_i(C) = \int dF P_i(F) \frac{\exp(-E_i F)(E_i F)^C}{C!} \tag{4.6}$$

and analogous to the continuous flux distribution of a number of sources as in eq. (4.5), the

discrete counts distribution is also a convolution of the individual source types,

$$P_i(C) = \sum_{J,K,L,M=0}^{C} P_i^{FSRQ}(J) P_i^{SFG}(K) P_i^{DM}(L) P_i^{BLLac}(M) \\ P_i^{Gal}(C - J - K - L - M) \tag{4.7}$$

Thus, the data i.e. the counts distribution puts constraints on the model parameters in the luminosity function of the source types.

Chapter 5

High Energy Polarisation

The work in this chapter was done in collaboration with co-authors Vasiliki Pavlidou and Brian Fields. It is yet to be submitted to a journal.

5.1 Introduction

Active galaxies or AGNs (active galactic nuclei) are some of the most luminous yet mysterious astronomical objects in the universe. Their particle and radiative emissions are powered by central supermassive black hole accreting matter. Part of the gravitational energy associated with accretion is converted into energy of particles such as cosmic rays and neutrinos and high energy radiation like X-rays and gamma-rays. Thus, these particles and radiation are messengers of the extreme astrophysical conditions in the core of active galaxies.

Blazars are distant AGNs where the observer's line of sight is along the jet axis, i.e. the observer looks down into the jets. Polarised, high energy photons are expected to be produced by inverse-Compton scattering of low energy seed photons in blazars (McNamara et al., 2009; Krawczynski, 2012). Seed photons can come from external sources (Meyer et al., 2012) like the accretion disk and cosmic microwave background (CMB) and internal sources within the jet like the synchrotron photons (Zacharias & Schlickeiser, 2012) emitted by the electrons. External target photons through external Compton (EC) mechanism are expected to produce a lower degree of polarisation than internal photons such as self-synchrotron Compton (SSC) (McNamara et al., 2009; Krawczynski, 2012).

Various properties of the radiation from blazars like the overall intensity, spectrum, and

variability have been studied with multiwavelength observations. However, polarisation at high energies has received much less attention, not just for blazars, but for any source class. High energy polarisation measurements of the Crab nebula / pulsar (e.g., Dean et al., 2008) are the most significant of the high energy polarimetric observations with the Crab being used for calibrating polarisation observations. There's also evidence for solar flares producing polarised X-rays (McConnell et al., 2003). Amongst transient sources, there are very few successful observations of gamma-ray bursts (GRBs) as listed in Chang et al. (2013) that . No high energy polarimetric data exists for blazars. This is in part due to the challenges in measurement of polarisation in X-rays and soft gamma-rays. However, with numerous X-ray and soft gamma-ray polarimeters at various stages of planning, design and operation and studies of optical / FIR polarisation properties of blazars underway, a systematic study of high energy polarisation from blazars is due. Thus, the amount and degree of high energy polarisation from blazars is an empirical and open question. However, the theoretical expectations are described in section 5.3. Throughout when referring to high energy polarisation, we mean X-ray and soft gamma ray polarisation.

Of course, polarised emission from GRBs and blazars at low energies has been studied in a lot more detail (e.g., Lazzati, 2006; Rossi et al., 2004; Wardle & Kronberg, 1974; Agudo et al., 2010; Fujiwara et al., 2012). Synchrotron emission is intrinsically polarised (Rybicki & Lightman, 1986) extending over a broad range of energies and is the main emission mechanism in GRB prompt and afterglow emission as well jet emission from both GRBs and active galaxies. The polarisation depends on magnetic field structure in the environment as well as the energy distribution in the jets (Lazzati, 2006). Blazars have two broad peaks in the spectral energy distribution of the jet emission. The first, lower energy peak is due to synchrotron emission that is intrinsically polarised (Rybicki & Lightman, 1986). It ranges from radio to as high an energy as X-rays. Observed emission from blazars at lower energies show polarisation (e.g. Fujiwara et al., 2012). The second peak is typically associated to inverse-Compton scattering of low energy photons that retains a fraction of this polarisa-

tion due to the nature of the inverse Compton scattering process (Bonometto et al., 1970; Krawczynski, 2012).

Polarisation is a key ingredient in the multimessenger understanding of blazars. The gains of studying this property are enormous. Polarisation can distinguish between different emission mechanisms of blazars such as different leptonic models and potentially between hadronic and leptonic. The connection with the hadronic models is mainly through the secondary leptons. Hadronic models are accompanied by neutrino emission, whereas polarisation should predominantly be from leptonic models via Compton scattering. So there may be an interesting neutrino polarisation connection to explore. Existence of polarisation in X-ray and gamma-ray emission from blazars distinguishes it from unpolarised sources at these energies. Furthermore, if blazars were to possess a reasonably high degree of polarisation, being high redshift sources like gamma-ray bursts, they could be used for probing Lorentz invariance violation using vacuum birefringence i.e. the rotation of the plane of polarised light due to quantum gravity models (e.g., Coleman & Glashow, 1999; Ellis et al., 2000; Laurent et al., 2011). The variability of blazars is a plus which can serve as a diagnostic for monitoring the relation between the jet activity and polarisation. This will also allow measurement of polarisation during the flaring states of those blazars that would under normal circumstances be undetectable in polarisation.

In this paper, we wish to focus on detection prospects of X-ray and soft gamma-ray polarisation of blazars with polarised seed photons in their jet. In Sec. 5.2, we discuss the degree of polarisation expected from inverse-Compton scattering of polarised low energy photons by relativistic electrons in the jet with a power law distribution. The minimum detectable polarisation (MDP) for various telescopes in general is reviewed with detectability of a typical blazar in Sec. 5.3. lists some of the brightest blazars and the time required to detect the MDP for different polarimeters. The detection prospects are improved due to flaring as described in section 5.4. In the section 5.5, we discuss the potential of polarised data to indirectly constrain hadronic emission. And in section 5.6, the conclusions along

with future directions are described.

5.2 Degree of polarisation of blazar

The degree of polarisation is the fraction of polarised light. Polarisation may be linear, circular or more generally elliptical. In general, the extent of polarisation is quantified in terms of the Stokes' parameters, I, Q, U, V where as usual

$$\begin{aligned} I &= I_x + I_y \\ Q &= I_x - I_y \\ U &= I_a - I_b \\ V &= I_r - I_l \end{aligned} \tag{5.1}$$

a, b represent directions at 45° to x, y respectively. I is the intensity of light, Q and U are measures of linear polarisation along any direction say x and along 45° from x respectively (along a) and V is the measure of circular polarisation. $Q = 100\%$ implies that the light is polarised along the + or - x-axis. If $Q = U = 0$, then $V = I$ and light is circularly polarised. The degree of polarisation is in general given by,

$$\Pi = \frac{\sqrt{Q^2 + U^2 + V^2}}{I} \tag{5.2}$$

The degree of linear polarisation consists only of Q and U, $\Pi_{\rm lin} = \frac{\sqrt{Q^2+U^2}}{I}$. Bonometto et al. (1970) calculated the polarisation of photons produced by inverse-Compton scattering of an arbitrary distribution of photons off an arbitrary, distribution of electrons. The simpler case of monochromatic beam of photons is studied that sets up future papers to study more realistic and complicated distribution of photons. The electrons are unpolarised. Both the target photons and the electrons are assumed to not have any spatio-temporal variations. There are two key conditions central to this calculation relating the initial ϵ and scattered

photon energies E_γ. The first is the definition of inverse-Compton scattering,

$$E_\gamma \gg \epsilon \tag{5.3}$$

The second is the Thomson limit in the center of mass frame, valid for a lot number of astrophysical scenarios including that for blazars,

$$\frac{E_\gamma}{m_\mathrm{e}} \frac{\epsilon}{m_\mathrm{e}} \ll 1 \tag{5.4}$$

For the inverse-Compton upscattered radiation, Bonometto et al. (1970) find the degree of linear polarisation for completely (100%) polarised target photons is computed to be

$$\Pi_\mathrm{BCS} = \frac{\Sigma_1 + \Sigma_2}{\Sigma_1 + 3\Sigma_2} \tag{5.5}$$

where the Σ's are related to the electron distribution function, $m(\gamma)$ as a function of the Lorentz factor, γ,

$$m(\gamma) = \frac{dn_\mathrm{e}}{d\gamma}\gamma^{-2} \quad ; \Sigma_1 = \int_0^1 m(\gamma)\left(x^2 - \frac{1}{x^2} + 2\right)dx \quad ; \quad \Sigma_2 = \int_0^1 m(\gamma)\frac{(1-x)^2}{x^2}dx \tag{5.6}$$

n_e is the number density of electrons and $x = \gamma_\mathrm{min}/\gamma$, with γ_min being the minimum Lorentz factor required by the electron to produce an up-scattered photon of a given energy given by $\gamma_\mathrm{min} = \frac{E_\gamma}{2\ m_\mathrm{e}}(1 + \sqrt{1 + 4\frac{m_\mathrm{e}^2}{\epsilon E_\gamma}})$. Furthermore, their results are computed for an isotropic distribution of electrons. This is a good assumption as the relativistic electrons under consideration here scatter photons into a narrow cone $\sim \gamma^{-1}$ around the direction of propagation. And as long as the electron distribution doesn't vary a lot over this solid angle in the rest frame of the electron plasma, the results hold true.

According to Bonometto et al. (1970), unpolarised target photons lead to unpolarised light post inverse-Compton scattering. This can be understood in terms of their observation

that Stokes' parameters change signs in changing from one polarisation state to its orthogonal state as evident from eqns $7.3 - 7.5$ in their paper. As a result, unpolarised target photons that can be viewed as a superposition of equal proportions of orthogonal polarisation, cancel out to give zero net polarisation. This is in contrast to Thomson scattering, that can produce polarisation from unpolarised photons.

Krawczynski (2012) re-evaluates analytically and numerically the calculation of polarisation due to inverse-Compton scattering. The numerical calculation is required to unambiguously ascertain the range of validity of results and also for precision in determining the degree of polarisation. The degree of polarisation is explicitly computed for the case of photons scattered in the jet of blazars verifying the result that unpolarised target photons lead to unpolarised scattered photons. The self-synchrotron and external Compton cases are studied explicitly with the conclusion that the external Compton leads to a smaller degree of polarisation owing to low degree of polarisation of target photons either from the start as for the CMB or by averaging over axisymmetric configuration in case of broad line region clouds. The degree of linear polarisation from scattering of the mono-energetic unidirectional photons off a power-law distribution with index p of electrons is given by,

$$\Pi_{pl} = \frac{(1+p)(3+p)}{(11+4p+p^2)} \tag{5.7}$$

For $p = 2$, $\Pi_{pl} \approx 65\%$ and $p = 3$, $\Pi_{pl} \approx 75\%$. Now, Compton scattering of polarised light leads to polarised light, and the degree of polarisation Π, is modified from the initial polarisation, Π_{in}, by this above mentioned factor as (Bonometto et al., 1970; Krawczynski, 2012) for a non-thermal electron distribution,

$$\Pi = \Pi_{pl} \times \Pi_{in} \tag{5.8}$$

Theoretically, for a power-law distribution of electrons, the degree of polarisation of syn-

chrotron emission is given by (Rybicki & Lightman, 1986),

$$\Pi_{sync} = \frac{p+1}{p+7/3} \tag{5.9}$$

that would give a large values for typical $p = 2 - 3$. However, various effects like Faraday rotation and inhomogeneities in the magnetic field can reduce this value [1]. In light of these complications, it is more reliable to use the observed values of Π_{in}. We thus, plan to test empirically the relation between degrees of low energy polarisation and high energy polarisation. From Fujiwara et al. (2012), more than half of the gamma-ray blazars are highly ($> 10\%$) polarised for at least part of the duty cycle. This quick estimate suggests, that from Krawczynski (2012) and Fujiwara et al. (2012), a degree of polarisation of a few % at least, for *Fermi* -LAT blazars in X-rays and soft gamma-rays. According to simulations in McNamara et al. (2009), the numbers are even higher. However, we will use the results from Krawczynski (2012) based on the analytical calculations in Bonometto et al. (1970). These numbers are also more conservative.

Now in general, Π is a function of the direction of target photons and energy of the scattered photons. Figures 8 and 9 in Krawczynski (2012) show Π to be an increasing function of the scattered photon energy implying by extrapolation that soft gamma-rays are likely to be polarised. However, a detailed calculation appropriate at hard X-ray / soft gamma-ray energies is needed to show this explicitly. Also, the calculation of Krawczynski (2012) is for uniform distributions of magnetic field, seed photons and electrons. However, in realistic jet models, a full calculation including their spatio-temporal variation as suggested by eq.(55) in Krawczynski (2012) should be performed.

[1] $http://www.astro.uni-wuerzburg.de/\ mkadler/scripts/jets\_ss12/jets\_hand04.pdf$

5.3 Minimum Detectable Polarisation (MDP) - Detection sensitivity of telescopes

In terms of classical electrodynamics, polarisation is defined in terms of the direction of the electric field vector in an electromagnetic wave. A polarisation analyser is a component of a polarimeter, that passes light with polarisation vector aligned to a particular direction or axis, and blocks the light with an orthogonal polarisation detector. Of course, for high energy radiation as for soft gamma-rays and X-rays, the quantum mechanical picture of individual photons is more applicable. In the quantum picture, it is the helicity of photons i.e. the projection of the photon's spin along the direction of propagation which defines polarisation. With spin 1, photons have three polarisation states, +1, 0, -1. Of these, only the transverse components corresponding to the ± 1 states are non-zero for a real, massless photon. These correspond to the right and left handed helicities or equivalently the right or left circular polarised light. Of course, independent of the basis in which polarisation is expressed, it is measured by detectors in terms of differences of intensities quantified by Stokes' parameters given above in eq. (5.1). Measurements of intensities at different angles is the basic technique behind measuring polarisation. There are several processes which record and retain the angular variation of intensity of polarised light such as Bragg reflection, Compton scattering, photoelectric effect and pair production (Novick, 1975) [2]. Of these, the Compton polarimeters are appropriate for the energy range of photons discussed here, wherein, the full Klein-Nishina cross-section depends on the angle between the polarisation vectors of initial and scattered photons (Heitler, 1954).

Whether in the classical picture or the quantum picture, the angular dependence of the polarisation signal can only be quantified in a *statistical* sense due to presence of backgrounds and noise. According to Novick (1975); Weisskopf et al. (2010), for a source producing N counts, the probability distribution of fractional polarisation say P due to statistical fluctu-

[2] $http://www.cesr.fr/spip.php?article863$

ations, measured by an analyser passing one polarisation state, $f(\Pi) = \exp\Big(-N\Pi^2/4\Big)$. Now a real detector has backgrounds and thus, the polarisation signal is a modulation $a = \delta\Pi$ over and above the background. Therefore, the probability of measuring this polarisation signal a, due to the source in presence of the background is given approximately by, $f(\Pi) = \exp\Big(-N(\Pi - a)^2/4\Big)$. Of course, the polarisation signal will likely have a modulation phase, which complicates the probability distribution further (Weisskopf et al., 2010).

Thus, (Weisskopf et al., 2010), polarisation can be manifested as a modulation of a signal observed in the azimuth ϕ about the line of sight in direction of the source. The modulation occurs at an angular frequency of two times the rotation frequency. The signal-to-noise ratio for N counts in case of Poisson noise is $1/\sqrt{N}$. Therefore, amplitude of modulation over a signal of R_S counts $\sec^{-1}$ in presence of a background R_S counts $\sec^{-1}$, that has only 1% chance of being exceeded, or at 99% confidence is (Novick, 1975; Weisskopf et al., 2010),

$$a_{1\%} = \frac{R_S + R_B}{R_S}\frac{n_\sigma}{\sqrt{N}} \tag{5.10}$$

where $n_\sigma = 4.29$ for 99% confidence level. The detector response to polarised light is quantified in terms of modulation factor, μ which is the amplitude for 100% polarised light in absence of background. Therefore the detectability of a given source of certain strength by a given detector is quantified in terms of the minimum degree of polarisation it can detect called the minimum detectable polarisation. The MDP given a source in general is therefore given by Novick (1975); Weisskopf et al. (2010); Kalemci et al. (2004),

$$MDP = \frac{n_\sigma}{\mu\ R_S}\sqrt{\left(\frac{2(R_S + R_B)}{T}\right)} \tag{5.11}$$

with T being the exposure time.

Now given a detector with a certain modulation factor μ and background R_B counts $\sec^{-1}$,

eq. (5.11) can be inverted to determine the amount of time required to observe a particular source producing R_S counts $\sec^{-1}$. As described above, blazars are theoretically expected to have polarised synchrotron emission. However, the exact theoretical computation is complicated by effects like Faraday rotation and inhomogeneities in the magnetic field. These computations are important and need to be performed, but will not be the focus of this work. Instead we chose to rely on observations.

The GEMS White Paper Krawczynski et al. (2013) proposes for GEMS like missions a strategy similar to what we describe below. They emphasise on using archival data on low energy polarisation in order to motivate observations of high energy polarisation. Their idea, of course is restricted to GEMS like missions. The study here extends to other polarimeters. And in addition to archival or published data, we plan to perform synergistic polarimetric observations at low and high energies of blazars like the ones mentioned below using RoboPol. [3]

Blazars are observed to show polarised emission at low energies like at IR wavelengths (Fujiwara et al., 2012). These blazars are selected from the *Fermi* -LAT catalog, that is an excellent all sky representation of blazars. We use these observed polarisation values and determine the degree of high energy polarisation of a blazar as described in section 5.2. We invert the above eq. (5.11) to determine how long it would take to detect the chosen blazar. This exercise is performed for 3 of the brightest blazars with the highest degree of near-IR polarisation. Indeed, there are several other candidates, however, 3C 454.3, PKS 0048-09 and PKS 1124-186 are the brightest blazars that have the highest measured IR polarisation from the list in and recorded for various polarimeters in Fujiwara et al. (2012). In addition a source like 3C 454.3 has shown significant variability Wehrle et al. (2012); Jorstad et al. (2010). Its flaring behaviour makes it a prime candidate for polarisation measurements as we will comment on in the next section 5.4.

The required observing times for the various X-ray and soft gamma-ray polarimeters

[3] $http://robopol.org/$

are computed for these chosen blazars. The polarimeters are PoGOLITE ($25-100$ keV), GEMS-like mission ($2-10$ keV), ASTRO-H ($50-200$ keV), POLARIX ($2-10$ keV) and GAP ($50-300$ keV). The flux of the blazars in units of CGS and mCrab (i.e. in terms of the flux of Crab in that particular range of energies) is tabulated along with the polarisation of target photons (Π_{in}) and the required observed times in Tables 5.1, 5.2, 5.3, 5.4 and 5.5.

Source	Flux ($\times 10^{-6}$ergs cm^{-2} sec^{-1})	Flux mCrab	Input Polarisation % Π_{in}	Observation time (Flight Times)
3C 454.3	1.85×10^{-4}	13.0	10	237
PKS 0048-09	4.32×10^{-5}	3.04	11.63	3212
PKS 1124-186	4.32×10^{-5}	3.04	9.45	4861

Table 5.1: Polarisation observational prospects - PoGOLITE: 200 mCrab,10% in 1 flight ($20 days$)

Source	Flux ($\times 10^{-6}$ergs cm^{-2} sec^{-1})	Flux mCrab	Input Polarisation % Π_{in}	Observation time (ksec)
3C 454.3	5.0×10^{-5}	3.51	10	3.24
PKS 0048-09	5.0×10^{-6}	0.35	11.63	239.80
PKS 1124-186	9.10×10^{-6}	0.64	9.45	2.74×10^{3}

Table 5.2: Polarisation observational prospects with XRT / ROSAT fluxes - GEMS (2 - 10 keV): 1 mCrab, 2% in 1000 ksec

Source	Flux ($\times 10^{-6}$ergs cm^{-2} sec^{-1})	Flux mCrab	Input Polarisation % Π_{in}	Observation time (ksec)
3C 454.3	1.32×10^{-4}	9.28	10	214.90
PKS 0048-09	4.32×10^{-5}	3.04	11.63	1.49×10^{3}
PKS 1124-186	4.32×10^{-5}	3.04	9.45	2.25×10^{3}

Table 5.3: Polarisation observational prospects with Swift-BAT fluxes - ASTRO-H (50-200 keV): 10 mCrab, 10% in 1000 ksec

Source	Flux ($\times 10^{-6}$ergs cm^{-2} sec^{-1})	Flux mCrab	Input Polarisation % Π_{in}	Observation time (ksec)
3C 454.3	5.0×10^{-5}	3.51	10	8.03
PKS 0048-09	5.0×10^{-6}	0.35	11.63	599.42
PKS 1124-186	9.10×10^{-6}	0.64	9.45	274.90

Table 5.4: Polarisation observational prospects with XRT / ROSAT fluxes - POLARIX (2.0-10.0 keV): 1 mCrab, 10% in 100 ksec

Source	Flux ($\times 10^{-6}$ergs cm^{-2} sec^{-1})	Flux mCrab	Input Polarisation % Π_{in}	Observation time (days)
3C 454.3	1.85×10^{-4}	13.0	10	4.73
PKS 0048-09	4.32×10^{-5}	3.04	11.63	97.21
PKS 1124-186	4.32×10^{-5}	3.04	9.45	64.24

Table 5.5: Polarisation observational prospects - GAP (50.0-300.0 keV): 1 Crab, 20% in 2 days

The PoGOLITE results based on our estimates using the analysis in Krawczynski (2012) suggest that detection of blazars will be challenging with sensitivity of a balloon experiment. Flaring blazars observed with dedicated balloon flights may have a chance of detecting the polarisation from blazars. This will demand, planned observations based on triggers from the optical, UV, IR telescopes monitoring flaring activity. With the future space based instruments, the sensitivity is much higher and thus, statistically significant detections are highly likely with reasonable observing times. Now, the space based instruments are not dedicated merely to polarisation measurements and therefore, observational strategies are required. Due to the high sensitivity, quiescent or non-flaring blazars are also expected to be discovered. This is achievable during all sky scans as well as by targeted, longer observations of the more dim blazars. And for flaring blazars optical, UV, IR triggers can be used for making detections. These strategies must be kept in mind while planning for future missions.

In addition to using published and archival data, we plan to perform synergistic, multiwavelength polarimetry with RoboPol [4] and high energy polarimeters. RoboPol is a fast optical polarimeter designed specifically to study blazars. It is a pointed instrument with high cadence. The camera onboard the instrument is designed specifically for monitoring of blazar jets . The polarimeter is mounted on the University of Cretes Skinakas Observatory 1.3 m telescope. From the above results, idea of using a dedicated, specialised polarimeter at optical wavelengths in conjunction with a high energy polarimeter will significantly improve the chances of detecting blazars. This is because monitoring the flaring activity of blazars as described in detail the next section 5.4 can be very useful to improve detection prospects.

[4] *http://robopol.org/*

Furthermore, there is evidence that polarisation certainly at low energies is dynamic (Sorcia et al., 2013). This suggests that given low energy polarisation is ultimately a source of high energy polarisation, polarimetric variability could be crucial at X-rays and gamma rays too. Polarimetric variability means that there are times when the degree of polarisation increases and therefore detectability improves. Also, variability in flux could be connected to that in polarisation, a connection that would ultimately lead to clues about the underlying mechanisms. Thus, multiwavelength polarimetry sharpen the emission models which connect the low energy to the high energy emission. Therefore, in order to faithfully probe the emission models, it is important to do synchronised multiwavelength observations. This is where dedicated, specialised like RoboPol can be critical to our understanding of polarisation and in general emission processes in blazars.

5.4 Flaring

Blazars are known to have flux variations (Nalewajko, 2013). They fluxes can vary by up to a factor of 10 or 20 when they flare. As discussed in the previous section, flaring activity of blazars affect the detectability in the polarisation domain. The direct reason is simply that those blazars that in their quiescent state fall below the detection limit may be pushed above threshold when they flare. Secondly, the polarisation signal itself may vary due to the flaring activity. This could in principle reduce the detectability and needs to be determined observationally. Here we propose a formalism to quantify the former effect, that is the increase in the detected fraction of blazars due to an increase in their flux or effectively a lowering of the detection limit by the same factor.

For this we use the formalism of Feldman and Pavlidou (in prep). Every blazar flares given a long enough time. Feldman and Pavlidou treat the flaring and quiescent blazars as a single population with two states. Both flaring and quiescent blazars are represented by a

single luminosity function. The two states differ by a flaring factor is given by

$$R = \frac{F_{\rm f}}{F_{\rm q}} \tag{5.12}$$

where $F_{\rm f}$ and $F_{\rm q}$ are fluxes in the flaring and quiescent state respectively. This flaring factor is assumed to be the same for all blazars and uniform in flux.

They find that the source flux distribution fitting the *Fermi* -LAT data has contributions from both quiescent and flaring sources. This implies an extrapolation of the distribution down to the fluxes at keV and MeV energies at which the polarimeters operate. In practice, this is easy as blazars have a power-law spectrum. And this will be done at the end when we provide numbers for the fractional increase in the detected blazars.

For simplicity, we demonstrate the formalism in terms of the LAT fluxes above 100 MeV. Above $F \sim 2 \times 10^{-9}$ photons cm^{-2} sec^{-1}, the fit to LAT data is in excellent agreement with the model that has all the blazars flaring. In accordance with Feldman and Pavlidou, if the duty cycle i.e. the fraction of time a blazar is in a flaring state is χ, then at any given time the number of blazars per unit flux in the flaring state is related to that in the quiescent state,

$$\frac{dN}{dF_{\rm q}} = \frac{1-\chi}{\chi}\frac{dN}{dF_{\rm f}} = C_{\rm q}\,\frac{dN}{dF_{\rm f}} \tag{5.13}$$

where $C_{\rm q} = \frac{1-\chi}{\chi}$ represents the factor by which the number of blazars in the quiescent state exceed the number in the flaring state at any given time in the universe. The mean flux $\langle F \rangle$ of blazars, is a weighted average of the flux of blazars in the quiescent state, $F_{\rm q}$ and that in the flaring state, $F_{\rm f}$.

$$\langle F \rangle = \chi F_{\rm f} + (1-\chi) F_{\rm q} \tag{5.14}$$

Now the all sky source flux distribution is given in terms of the mean flux observed over

a long period of time as,

$$\begin{aligned}\frac{dN}{dF} &= A\left(\frac{F}{F_{\rm b}}\right)^{-\beta_1} \quad , \quad F \geq F_{\rm b} \\ &= A\left(\frac{F}{F_{\rm b}}\right)^{-\beta_2} \quad , \quad F < F_{\rm b}\end{aligned} \tag{5.15}$$

in accordance with (Abdo et al., 2010l). with the parameter values corresponding to the best fit values for all blazars both FSRQs and BL LACs put together are $A_{\rm Fermi} = 16.46 \times 10^{-14}{\rm cm}^2$ sec deg^{-2}, $F_{\rm b} = 6.60 \times 10^{-8}$ph cm^{-2} sec^{-1} , $\beta_1 = 2.49$ and $\beta_2 = 1.58$. The source flux distribution is normalised here to the break flux, to give $A = A_{\rm Fermi}F_{\rm b}^{-\beta_1} = 1.25 \times 10^5{\rm cm}^2$ sec deg^{-2} ph according to Feldman and Pavlidou.

As a result of flaring, the break flux is shifted to lower value $F_{\rm b}/R$. So, the source flux distribution is modified to include both flaring and quiescent blazars as they may be treated as a single population given by,

$$\begin{aligned}\left.\frac{dN}{dF}\right|_{\rm obs} &= A\left(\frac{F}{F_{\rm b}}\right)^{-\beta_1} + ARC_{\rm q}\left(\frac{RF}{F_{\rm b}}\right)^{-\beta_1} \quad , \quad F \geq F_{\rm b} \\ &= A\left(\frac{F}{F_{\rm b}}\right)^{-\beta_2} + ARC_{\rm q}\left(\frac{RF}{F_{\rm b}}\right)^{-\beta_1} \quad , \quad \frac{F_{\rm b}}{R} \leq F \leq F_{\rm b} \\ &= A\left(\frac{F}{F_{\rm b}}\right)^{-\beta_2} + ARC_{\rm q}\left(\frac{RF}{F_{\rm b}}\right)^{-\beta_2} \quad , \quad F \leq \frac{F_{\rm b}}{R}\end{aligned} \tag{5.16}$$

The observed quantity over an integration time T, is of course, the mean flux $\langle F \rangle$. Now, this leads to two limits, when the observation time is much longer than the period of the flare, P and vice versa. In the limit that, the observation time is long enough, $T \gg P$, all "flaring events" including multiple flares from the same source are detected. Therefore, the number of flaring events is given by $N_{\rm u}T/P = N_{\rm u}\chi T/t$. In this case, the mean flux is related

to the flaring flux as,

$$\langle F \rangle = \chi F_{\rm f} + (1-\chi) F_{\rm f}/R \tag{5.17}$$

$$=> F_{\rm f} = \frac{R}{(R-1)\chi + 1} \langle F \rangle = R_{\rm eff} \langle F \rangle \tag{5.18}$$

$$R_{\rm eff} = \frac{R}{(R-1)\chi + 1} \quad , \quad \frac{\chi T}{t} \gg 1 \tag{5.19}$$

For typical values of flaring factor, $R = 10$ and a duty cycle of $\chi = 1\%$, $R_{\rm eff} = 9.2$. For a longer duty cycle, say $\chi = 20\%$, the mean flux remains closer to the flaring flux and therefore we get a lower $R_{\rm eff} = 3.6$. Suppose, $N_{\rm u}$ is the number of sources undetected in the quiescent state, but that are detected during their flaring state. Therefore,

$$N_{\rm u} = \int_{\frac{F_{\rm sens}}{R_{\rm eff}}}^{F_{\rm sens}} \frac{dN}{dF}\, dF \tag{5.20}$$

where $F_{\rm sens}$ is the sensitivity of the polarimeter. Now in principle, computing $N_{\rm u}$ tells me the additional number of blazars detected in polarisation. In practice however, from the fluxes of our candidate blazars in the previous section and the observation times needed to detect them, it is only the very bright few blazars that will be detected anyway. And so the bright end of the source flux distribution $\frac{dN}{dF}$ is of interest. Of course, the exact number of additional blazars detected by the polarimeters will depend on their flux sensitivity (or MDP) and of course the duty cycle and periodicity of flaring. A comparison of the mean flux to the sensitivity gives an idea of the increase in detectability. The mean flux is computed for limit when all blazars originally below the sensitivity, that exceed the sensitivity limit due to flaring are detected.

Thus, from equation (5.20), the integration range reduces from $\sim 90\%$ to $\sim 72\%$. Picking a sensitivity higher than the break flux $F_{\rm sens} = F_{\rm b} R_{\rm eff}$ as most certainly the blazars detectable are above the break, could potentially almost double of the number of blazars for a duty

cycle of $\sim 20\%$. However, as stated before the actual numbers would depend on a number of factors including the assumption that all blazars flare. And indeed since there would be a handful of blazars, instead of a detailed statistical description, individual blazars that are known to flare and have a high degree of polarisation at the lower energies should be selected for pointed observations. We expect that the number of blazars detected due to flaring activity would nearly double.

5.5 Indirect constraints on hadronic emission

As we discussed above, polarisation is a probe of emission mechanisms of blazars. In fact, polarised X-rays and gamma-rays are primarily a probe of leptonic emission. Amongst leptonic emission, inverse-Compton scattering by electrons and synchrotron radiation are the most likely mechanisms of producing polarisation. The blazar spectral energy distribution consists of two broad spectral peaks or bumps (Abdo et al., 2010m). The lower energy peak is usually put down to synchrotron emission that is intrinsically polarised (Rybicki & Lightman, 1986). The higher energy peak is believed to be due to inverse-Compton scattering of either the synchrotron radiation itself or some other source of photons. As described above in detail, inverse-Compton emission in blazars is likely to be polarised since, the underlying target photon distribution is polarised. And data on polarised radiation is capable of identifying and distinguishing between synchrotron emission and inverse-Compton emission as they in principle produce different degrees of polarisation. Thus, thus discovery of polarised emission at high energies would be a test of models of blazar SEDs amongst other things.

Now high energy emission could also be hadronic (e.g. Becker, 2008; Reimer, 2012; Doert et al., 2012; Dermer et al., 2007). Hadronic processes involving protons produce high energy radiation mainly gamma rays in the following ways. They first interact with either other

protons or photons (Becker, 2008).

$$\begin{aligned} p\ \gamma \rightarrow \Delta^{+} \ &\rightarrow \ p\ \pi^{0} \\ &\rightarrow \ n\ \pi^{+} \end{aligned} \tag{5.21}$$

$$p\ p \rightarrow \pi^{+}\ \pi^{-}\ \pi^{0} \tag{5.22}$$

The resulting pions decays produce gamma rays directly or indirectly. Neutral pions decay to photons directly as

$$\pi^{0} \rightarrow \gamma\ \gamma \tag{5.23}$$

The charged pions decay into secondary leptons, that can then produce synchrotron or inverse-Compton emission.

$$\pi^{+} \ \rightarrow \ \mu^{+}\ \nu_{\mu} \rightarrow e^{+}\ \nu_{e}\ \nu_{\mu}\ \nu_{\mu} \tag{5.24}$$

Hadronic emission from blazars could also produce polarisation from the secondary leptons. Once, again the leptons would produce IC scattering and synchrotron radiation. The spectrum of this polarised radiation would be different from that produced by the primary leptons. As a result, by spectro-polarimetric observations secondary leptonic gamma rays will be identified and their relative proportion to other processes determined. Particularly as the secondary leptonic emission can be related to its primary hadronic source through branching ratios, it is possible to put indirect constraints on the primary hadronic emission via the leptonic secondaries. And as, these leptons are again correlated by well defined branching ratios to neutrinos, there are some prospects of a possible relation between neutrino and polarised high energy emission, though it is likely to be model dependent and potentially complicated. But these are exciting avenues that need to be explored in order to completely understand those very complications that are so central to the emission mechanisms in blazars.

5.6 Discussion and conclusions

It is very clear that polarimetry is the next frontier in high energy astronomy that holds a lot of promise. It is extremely challenging to perform polarimetric measurements in general. Specifically for blazars, it is possible that instruments in space are required to make detections. However, in an ideal situation, i.e. if there are dedicated balloon flights performing observations of previously selected sources that are flaring, then it is not inconceivable that a signal maybe be observed. Also, remembering that high energy polarisation hasn't yet been measured and the predictions are based on theoretical assumptions albeit reasonable ones, if the polarisation values happen to be as high as simulations in McNamara et al. (2009) predict then balloon experiments will have an excellent chance of detecting something.

The strategy of using the low energy polarisation measurements of blazars from Fujiwara et al. (2012); Blinov et al. (2013) and other similar work to select blazars looks promising to effectively focus on the ones which are the brightest and most polarised. All of this is expressed in terms of the MDP and required observation times. This is similar to the plan proposed by the GEMS team Krawczynski et al. (2013). The numbers for GEMS-like mission are consistent with those found by This is similar to the plan proposed by the GEMS team Krawczynski et al. (2013). Of course, this study is not limited to GEMS like missions or that energy range. Predictions have been made for a number of different polarimetric missions such as PoGOLITE, Astro-H, POLARIX, GAP.

As discussed in section 5.4, flaring increases detectability of blazars. Monitoring flaring activity of sources in optical and other wavelengths to determine flare statistics will help build our database of promising candidates while waiting for upcoming polarimetry missions. Low energy polarimetry missions like RoboPol can be used to guide high energy polarimetry observations based on monitoring of flaring blazar as Blinov et al. (2013). And in future, synergistic multiwavelength polarimetry observations will definitely increase chances of discovering blazars in this new domain.

Polarimetry is critical to not just multiwavelength, but possibly multimessenger astro-

physics as pointed out in section 5.5. Neutrinos are indicators of primarily hadronic emission mechanisms in blazars. Polarisation could be an indicator of both, though it is more directly related to the primary leptonic emission. It is associated to hadronic mechanism via radiative emission from the secondary electrons. Thus, polarimetry could probe both secondary and primary emission and hadronic and leptonic emission. And more specifically, it can distinguish between self-synchrotron and external Compton mechanism.

In addition, high polarimetry of blazars can potentially put constraints on Lorentz Invariance Violation in much the same way as GRBs do. If blazars were to possess a reasonably high degree of polarisation, being high redshift sources, they could be used for probing LIV (e.g., Coleman & Glashow, 1999; Ellis et al., 2000; Laurent et al., 2011) using vacuum birefringence.

Thus, high energy polarimetry is an exciting field with tremendous discovery potential. There is a huge scope for theoretical work and observational and mission strategising in preparation for future generation of polarimeters.

Chapter 6

Radio Supernovae in the Great Survey Era

Abstract

[1] Radio properties of supernova outbursts remain poorly understood despite longstanding campaigns following events discovered at other wavelengths. After ~ 30 years of observations, only ~ 50 supernovae have been detected at radio wavelengths, none of which are Type Ia. Even the most radio-loud events are $\sim 10^4$ fainter in the radio than in the optical; to date, such intrinsically dim objects have only been visible in the very local universe. The detection and study of radio supernovae (RSNe) will be fundamentally altered and dramatically improved as the next generation of radio telescopes comes online, including EVLA, ASKAP, and MeerKAT, and culminating in the Square Kilometer Array (SKA); the latter should be $\gtrsim 50$ times more sensitive than present facilities. SKA can repeatedly scan large ($\gtrsim 1\,\mathrm{deg}^2$) areas of the sky, and thus will discover RSNe and other transient sources in a new, automatic, untargeted, and unbiased way. We estimate SKA will be able to detect core-collapse RSNe out to redshift $z \sim 5$, with an all-redshift rate ~ 620 events yr^{-1} deg^{-2}, assuming a survey sensitivity of 50 nJy and radio lightcurves like those of SN 1993J. Hence SKA should provide a complete core-collapse RSN sample that is sufficient for statistical studies of radio properties of core-collapse supernovae. EVLA should find ~ 160 events yr^{-1} deg^{-2} out to redshift $z \sim 3$, and other SKA precursors should have similar detection rates. We also provided recommendations of the survey strategy to maximize the RSN detections of SKA. This new radio core-collapse supernovae sample will complement the detections from the optical

[1]This chapter matches the version which has been submitted to Astrophysical Journal, and posted version on arxiv.org numbered on arXiv:1206.0770 and is co-authored with Brian Fields.

searches, such as the LSST, and together provide crucial information on massive star evolution, supernova physics, and the circumstellar medium, out to high redshift. Additionally, SKA may yield the first radio Type Ia detection via follow-up of nearby events discovered at other wavelengths.

6.1 Introduction

Supernovae are among the most energetic phenomena in the universe, and are central to cosmology and astrophysics. For example, core-collapse supernovae are explosions arise from the death of massive stars and hence are closely related to the cosmic star-formation rate and to massive-star evolution, and are responsible for the energy and baryonic feedback of the environment (Madau et al., 1998). Type Ia supernovae show a uniform properties in their lightcurves and play a crucial role as cosmic "standardizable candles" (Phillips, 1993; Riess et al., 1996).

Our knowledge of the *optical* properties of supernovae, is increasing rapidly with the advent of prototype "synoptic"–i.e., repeated scan–sky surveys, such as SDSS-II (Frieman et al., 2008; Sako et al., 2008) and SNLS (Bazin et al., 2009; Palanque-Delabrouille et al., 2010). These campaigns are precursors to the coming "Great Survey" era in which synoptic surveys will be conducted routinely over very large regions of sky, e.g., LSST [2] (LSST Science Collaboration et al., 2009) and Pan-STARRS [3]. The number of detected supernovae will increase by several orders of magnitude in this era (LSST Science Collaboration et al., 2009; Lien & Fields, 2009).

In contrast to this wealth of optical information, properties of supernovae in the radio remain poorly understood, fundamentally due to observational limitations. Radio supernovae (RSNe) have primarily been discovered by follow-up observations of optical outbursts, and only very rarely by accident. To date, only $\sim$ 50 core-collapse outbursts have radio

[2]http://www.lsst.org/Science/docs/SRD.pdf
[3]http://pan-starrs.ifa.hawaii.edu/project/science/precodr.html

detections, and no Type Ia explosion has ever been detected in the radio (Weiler et al., 2004; Panagia et al., 2006). The core-collapse subtype Ibc has been a focus of recent study in the radio, because some Type Ibc events are associated with long Gamma-Ray Bursts (GRBs) (Galama et al., 1998; Kulkarni et al., 1998; Soderberg, 2007; Berger et al., 2003).

Current radio interferometers are scheduled primarily around targeted observations proposed by individual principal investigators. This stands in contrast to future radio interferometers planned for the coming "Great Survey" era. These include the Square Kilometer Array (SKA[4]) and its precursor prototype arrays (for example, ASKAP[5] and MeerKAT[6]). These telescopes will operate primarily as wide-field survey instruments focusing on several key science projects (Carilli & Rawlings, 2004). As synoptic telescopes, they will be far better suited to study all classes of transient and time-variable radio sources, including RSNe. Gal-Yam et al. (2006) already pointed out the power of synoptic radio surveys for detecting radio transients of various types, including supernovae and GRBs, in an unbiased way. Here we quantify the prospects for RSNe.

In this paper we explore this fundamentally new mode of *untargeted* RSN discovery and study. We adopt a forward-looking perspective, and consider the new science enabled by RSNe observations in an era in which the full SKA is operational. Our focus is mainly on core-collapse supernovae, the type for which some radio detections already exist. However, we will also discuss the possibility of Type Ia radio discovery based on current detection limits. We will first summarize current knowledge of radio core-collapse supernovae (§6.2), and the expected sensitivity of SKA (§6.3). Using this information, we forecast the radio core-collapse supernovae harvest of SKA (§6.4), and consider optimal survey strategies (§6.5). We conclude by anticipating the RSN science payoff in this new era (§6.6). We adopt a standard flat ΛCDM model with $\Omega_{\rm m} = 0.274$, $\Omega_\Lambda = 0.726$, and $H_0 = 70.5\,{\rm km\,s^{-1}\,Mpc^{-1}}$ (Komatsu et al., 2009) throughout.

[4]http://www.ska-telescope.org
[5]http://www.atnf.csiro.au/projects/askap
[6]http://www.ska.ac.za/meerkat

6.2 Radio Properties of Supernovae

Several key properties of RSNe have been established, as a result of the longstanding leadership of the NRL-STScI group (recently reviewed in Weiler et al., 2009; Stockdale et al., 2007; Panagia et al., 2006) and of the CfA group and others (summarized in Soderberg, 2007; Berger et al., 2003). We summarize these general RSN characteristics, which we will use to forecast the RSN discovery potential of synoptic radio surveys.

6.2.1 Radio Core-Collapse Supernovae

Observed core-collapse RSNe have luminosities spanning $\nu L_\nu \sim 10^{33} - 10^{38}$ erg s^{-1} at 5 GHz, and thus are $\gtrsim 10^4$ times less luminous in the radio than in the optical. Their intrinsic faintness has prevented RSN detection in all but the most local universe. Even within a particular core-collapse subtype, radio luminosities and lightcurves are highly diverse, e.g., two optically similar Type Ic events might be radio bright in one case and undetectable in the other (Munari et al., 1998; Nakano & Aoki, 1997) [7] [8]. Additionally, core-collapse RSNe spectral shapes strongly evolve with time; lightcurves peak over days to months depending on the frequency. RSN emission can be understood in terms of interactions between the blast, ambient relativistic electrons, and the circumstellar medium (Chevalier, 1982a,b, 1998).

To model RSN emission as a function of frequency and time, we adopt the semi-empirical form derived by Chevalier (1982a) and extended in Weiler et al. (2002),

$$L(t,\nu) = L_1 \left(\frac{\nu}{5\,\mathrm{GHz}}\right)^{\alpha} \left(\frac{t}{1\,\mathrm{day}}\right)^{\beta} e^{-\tau_{\mathrm{external}}} \left(\frac{1-e^{-\tau_{\mathrm{CSM_{clumps}}}}}{\tau_{\mathrm{CSM_{clumps}}}}\right) \left(\frac{1-e^{-\tau_{\mathrm{internal}}}}{\tau_{\mathrm{internal}}}\right) \quad . \quad (6.1)$$

We follow the notation of Weiler et al. (2002). $L(t,\nu)$ is the supernova luminosity at frequency ν and time t after the explosion. Optical depths from material both outside (τ_{external}, $\tau_{\mathrm{CSM_{clumps}}}$) and inside ($\tau_{\mathrm{internal}}$) the blast-wave front are taken into account (see Weiler et al.,

[7] http://rsd-www.nrl.navy.mil/7213/weiler/sne-home.html

[8] New Radio Supernova Results are available online at: http://rsdwww.nrl.navy.mil/7213/weiler/sne-home.html

2002).

Parameters embedded in each optical depth term are those for SN 1993J, one of the best studied RSNe (Weiler et al., 2007). Radio emission from SN 1993J is dominated by the clumped-circumstellar-medium (clump-CSM) term, and hence

$$L(t,\nu) \sim \frac{1 - e^{-\tau_{\mathrm{CSM_{clumps}}}}}{\tau_{\mathrm{CSM_{clumps}}}}, \tag{6.2}$$

where $\tau_{\mathrm{CSM_{clumps}}} = 4.6 \times 10^5 \ (\frac{\nu}{5\ \mathrm{GHz}})^{-2.1} \ (\frac{t}{1\ \mathrm{day}})^{-2.83}$, for SN 1993J. At small t, $\tau_{\mathrm{CSM_{clumps}}}$ is large and $L(t,\nu) \sim 1/\tau_{\mathrm{CSM_{clumps}}} \propto \nu^{2.1}\ t^{2.83}$, so luminosity grows as a power law at early times. With all optical depth parameters fit to SN 1993J, the peak luminosity is controlled by the prefactor L_1.

Our main focus will be on RSN discovery, and thus it is most important to capture the wide variety of peak radio luminosities, which correspond in our model to a broad distribution for L_1. Figure 6.1 shows a crude luminosity function (not-normalized) based on the sample of 20 core-collapse supernovae (15 Type II and 5 Type Ibc) that have a published peak luminosity at 5 GHz (Weiler et al., 2004; Stockdale et al., 2003, 2007; Papenkova et al., 2001; Baklanov et al., 2005; Pooley et al., 2002). We use 5 GHz data to construct our luminosity function because the most RSNe have been observed at this frequency. However, our predictions will span a range of frequencies, based on this luminosity function and eq. (6.2). The data are divided into four luminosity bins of size $\Delta \log_{10}(L) = 1$. The black curve in Fig. 6.1 is the best-fit Gaussian, with average luminosity $\log_{10}(L_{\mathrm{avg}}/\mathrm{erg\,s^{-1}\,Hz^{-1}}) = 27.3$, a standard deviation $\sigma = 1.25$, and $\chi^2 = 0.18$. SN 1987A is marked in Fig. 6.1, but was not used in the fit to avoid possible bias due to its uncommonly low luminosity. The fitted luminosity function might be biased towards the brighter end, because of the current survey sensitivity and the small and incomplete nature of the sample.

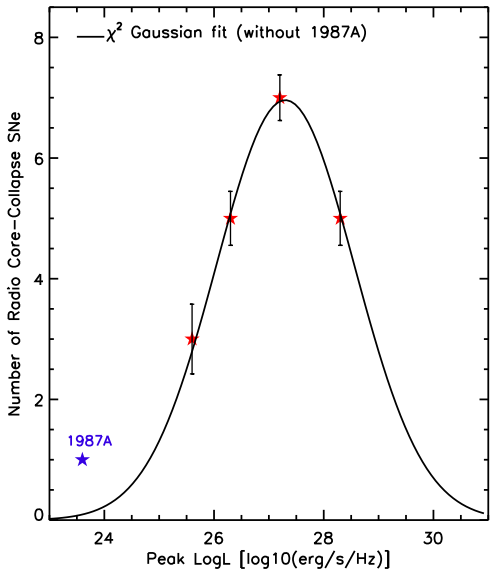

Figure 6.1: Radio luminosity function (not-normalized) at 5 GHz of core-collapse supernovae showing core-collapse supernovae count as a function of $\log_{10}(L)$, where L is the peak radio luminosity. Data are binned to $\Delta \log_{10}(L) = 1$. The black curve shows the χ^2-fitted Gaussian to the underlying data (red stars).

6.2.2 Radio Type Ia Supernovae

All searches to date have failed to detect radio emission from Type Ia supernovae. Panagia et al. (2006) reported the radio upper limits of 27 Type Ia supernovae from more than two decades of observations by the Very Large Array (VLA). The weakest limit on a Type Ia event is 4.2×10^{26} erg s^{-1} Hz^{-1} at 1.5 GHz for SN 1987N, which is around one order of magnitude lower than the average luminosity of radio-detected core-collapse supernovae (see §6.2.1). The strongest limit on Type Ia radio emission is even tighter, 8.1×10^{24} erg s^{-1} Hz^{-1} at 8.3 GHz for SN 1989B. Additionally, the $z \sim 0$ cosmic Type Ia supernova rate is around 1/4.5 of the core-collapse supernova rate (Bazin et al., 2009). The intrinsic faintness in radio and their smaller rate make detecting Type Ia in radio observations especially hard.

6.3 Next-Generation Radio Telescopes: Expected Sensitivity

Radio detections of supernovae to date have been restricted both by the limiting sensitivity of contemporary radio interferometers and the need for dedicated telescope time for transient followup. This situation will change drastically with SKA's unprecedented sensitivity and particularly by its ability to repeatedly scan large regions of the sky at this great depth.

Current SKA specifications adopt a target sensitivity parameter $A_{\rm eff}/T_{\rm sys} = 10^4$ m^2 K^{-1} at observing frequencies in the low several GHz, including $z = 0$ HI at 1.4 GHz. $A_{\rm eff}$ is the effective aperture, and $T_{\rm sys}$ is the system temperature. We will adopt this value of $A_{\rm eff}/T_{\rm sys}$, which yields a 1-σ rms thermal noise limit in total intensity of

$$\sigma_I = 0.15\ \mu{\rm Jy}\ (\Delta\nu/{\rm GHz})^{-1/2}\ (\delta{\rm t}/{\rm hr})^{-1/2}, \tag{6.3}$$

for a bandwidth $\Delta\nu$ and observation duration δt. The SKA will therefore reach a thermal noise limit of several nJy in deep continuum integrations ($\delta t \sim 1000$ hr) [9]. We define the associated survey sensitivity $S_{\rm min}$ (the minimum flux density threshold) as $S_{\rm min} = 3\sigma_I$. In common with other radio interferometers, SKA will accumulate sensitivity in targeted deep fields, including transient-monitoring fields, by accumulating integration time over multiple individual observing tracks. We therefore will adopt a fiducial SKA supernova sensitivity of $S_{\rm min} = 50$ nJy in 100 hours of observation, but we will show how our results are sensitive to other choices of $S_{\rm min}$.

It is anticipated that transient fields will be revisited with a cadence appropriate to the variability timescales under study and that interferometric inverse imaging methods will include source models with time variability. Survey optimization for interferometric transient detection is an active area of current SKA research. The technical details are beyond the intent and scope of this paper, but will be influenced by science goals for transient source

[9] http://www.skatelescope.org/PDF/DRM_v1.0.pdf

study in general, including pulsars, GRBs, and supernovae (as considered in this paper), as well as the as-yet undiscovered transient population.

6.4 Radio Supernovae for SKA

With its unprecedented sensitivity, SKA will be capable of synoptic search for core-collapse RSNe and open new possibilities in radio astronomy. In this section, we predict the RSN detections of SKA based on current knowledge to demonstrate how the RSN survey can be done.

6.4.1 Core-Collapse Supernovae

The detection rate $\Gamma_{\rm detect} = dN_{\rm SN}/(dt_{\rm obs}\, d\Omega\, dz)$ for a given RSN survey is

$$\Gamma_{\rm detect} = f_{\rm survey}\ f_{\rm radio}\ f_{\rm ISM}\ \Gamma_{\rm SN} \quad , \tag{6.4}$$

and is set by several observability factors f that modulate the total rate of all supernovae

$$\Gamma_{\rm SN}(z) = \frac{dN_{\rm SN}}{dV_{\rm comov}\, dt_{\rm em}}\ \frac{dt_{\rm em}}{dt_{\rm obs}}\ \frac{dV_{\rm comov}}{d\Omega\, dz} = \mathcal{R}_{\rm SN}(z)\, r^2_{\rm comov}(z)\, c \left|\frac{dt}{dz}\right| \tag{6.5}$$

within the cosmic volume out to redshift z (Madau et al., 1998; Lien & Fields, 2009).

We see that the total cosmic supernova rate $\Gamma_{\rm SN}$ depends on cosmology via the volume element and the time dilation terms. Because ΛCDM cosmological parameters are now known to high precision, these factors have a negligible error compared to the other ingredients in the calculation. The other factor in $\Gamma_{\rm SN}$ is the cosmic core-collapse supernova rate density $\mathcal{R}_{\rm SN}(z) = dN_{\rm SN}/(dV_{\rm comov}\, dt_{\rm emit})$. Some direct measurements of this rate now exist out to $z \sim 1$, but the uncertainties remain large (Cappellaro et al., 1999; Dahlen et al., 2004; Cappellaro et al., 2005; Hopkins & Beacom, 2006; Botticella et al., 2008; Dahlen et al., 2008; Kistler et al., 2011; Bazin et al., 2009; Smartt et al., 2009; Dahlen et al., 2010; Li et al.,

2011c; Horiuchi et al., 2011). However, core-collapse events are short-lived, and so the cosmic core-collapse rate is proportional to the cosmic star-formation rate $\dot{\rho}_\star$, which is much better-determined and extends to much higher redshifts. We thus derive $\mathcal{R}_{\rm SN}$ from the recent Horiuchi et al. (2009b) fit to the cosmic star-formation rate. The proportionality follows from the choice of initial mass function; we apply the Salpeter initial mass function (Salpeter, 1955) and assume the mass range of core-collapse SNe progenitors to be $8M_\odot - 50M_\odot$; this gives $\mathcal{R}_{\rm SN} = (0.007\, M_\odot^{-1})\, \dot{\rho}_\star$

Several effects reduce the total rate $\Gamma_{\rm SN}$ to the observed rate $\Gamma_{\rm detect}$ in eq. (6.4). Due to finite survey sensitivity, only a fraction $f_{\rm survey}$ of events are bright enough to detect, and only some fraction $f_{\rm radio}$ of supernovae will emit in the radio. We neglect interstellar extinction and assume $f_{\rm ISM} \sim 1$ at the radio wavelengths considered.

The term $f_{\rm radio}$ in eq. (6.4) contains the greatest uncertainty due to the relatively small sample of RSNe observed to date, and the unavoidable incompleteness of the sample (K. Weiler, private communication 2010). The only published fraction available is for Type Ibc supernovae. Using VLA for radio follow-up, Berger et al. (2003) suggests that $f_{\rm radio,Ibc} \sim 12\%$ after surveying 33 optically-detected Type Ibc supernovae. For the purpose of demonstration, we will adopt $f_{\rm radio} = 10\%$ for the calculations presented in this paper, which we believe is rather conservative.

An order-of-magnitude calculation provides a useful estimate of the expected core-collapse RSN rate. As discussed in §6.3, we adopt a fiducial SKA sensitivity of $S_{\rm min} = 50$ nJy. Hence SKA will be able to detect supernovae with average radio luminosity ($L \sim 10^{27}$ erg s^{-1} Hz^{-1}) to a distance $D_L = \sqrt{L/4\pi S_{\rm min}} \sim 4$ Gpc, which for a ΛCDM cosmology corresponds to $z \sim 1$. This will give a detectable volume of $V_{\rm detect} \sim (4/3)\pi D_L^3 \sim 2.85 \times 10^{11}$ Mpc^3. Observations show that the core-collapse supernova rate $R_{\rm SN} \sim 10^{-3}$ yr^{-1} Mpc^{-3} at $z \sim 1$ (Dahlen et al., 2008, 2010). Assuming the fraction of the total core-collapse supernovae that display the adopted average radio luminosity to be $f_{\rm radio} \sim 10\%$ (Berger et al., 2003), the all-sky detection rate $dN_{\rm SN}/dt \sim R_{\rm SN} \times f_{\rm radio} \times V_{\rm detect} \sim 2.85 \times 10^7$ yr^{-1}. This corresponds

to a areal detection rate $dN_{\rm SN}/(dt\,d\Omega) \sim 700$ yr^{-1} deg^{-2}. As we now see, a more careful calculation confirms this estimate.

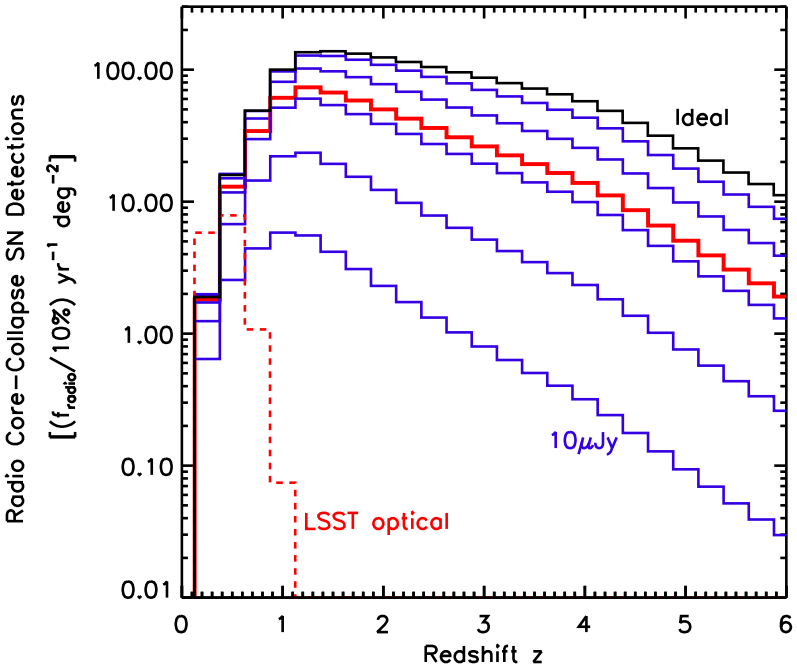

Figure 6.2: Estimated radio core-collapse supernova detection rate as a function of redshift at 1.4 GHz, assuming $f_{\rm radio} = 10\%$. Predictions are shown for different survey sensitivities: $S_{\rm min} = \{10\ \mu$Jy (blue), 1 μJy (blue), 100 nJy (blue), 50 nJy (thick red), 10 nJy (blue), 1 nJy (blue)$\}$ from bottom to top solid curves, respectively. We adopt 50 nJy as our benchmark sensitivity hereafter. For comparison, the red-dashed curve shows the LSST optical supernova detection rate per year per deg^2 (Lien & Fields, 2009). Also, the top solid curve (black) plots the ideal core-collapse RSN rate for comparison.

A careful prediction involves detailed calculation of $f_{\rm survey}(z)$. The fraction $f_{\rm survey}(z)$ of observable radio-emitting events depends on adopted survey sensitivity, and on the normalized supernova luminosity function $\Phi_{\rm 5GHz}(\log L)$, which is measured at a peak luminosity at 5 GHz (derived in § 6.2). In this paper we will only consider whether a supernova is detectable at its peak luminosity at each corresponding frequency. The peak radio luminosity should be reached earlier at higher frequencies because of preferential absorption at lower frequencies (Weiler et al., 2002). At different redshift, the peak flux density $S_{\rm min}^{\rm peak}$ in the

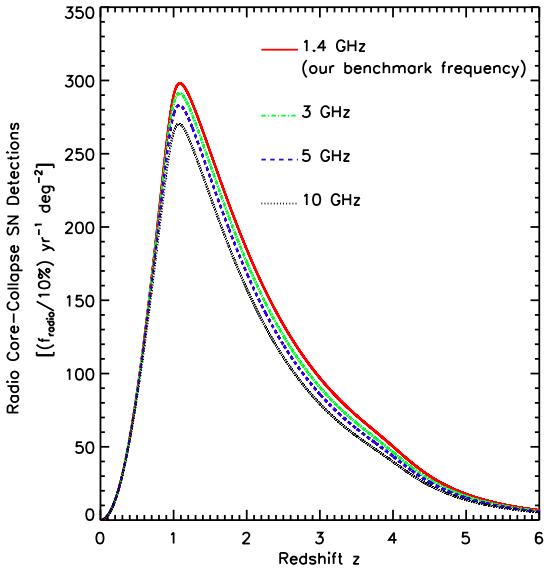

Figure 6.3: Estimated radio core-collapse supernova detection rate as a function of redshift for different frequency bands, for $f_{\rm radio} = 10\%$, and an adopted survey sensitivity $S_{\rm min} = 50$ nJy.

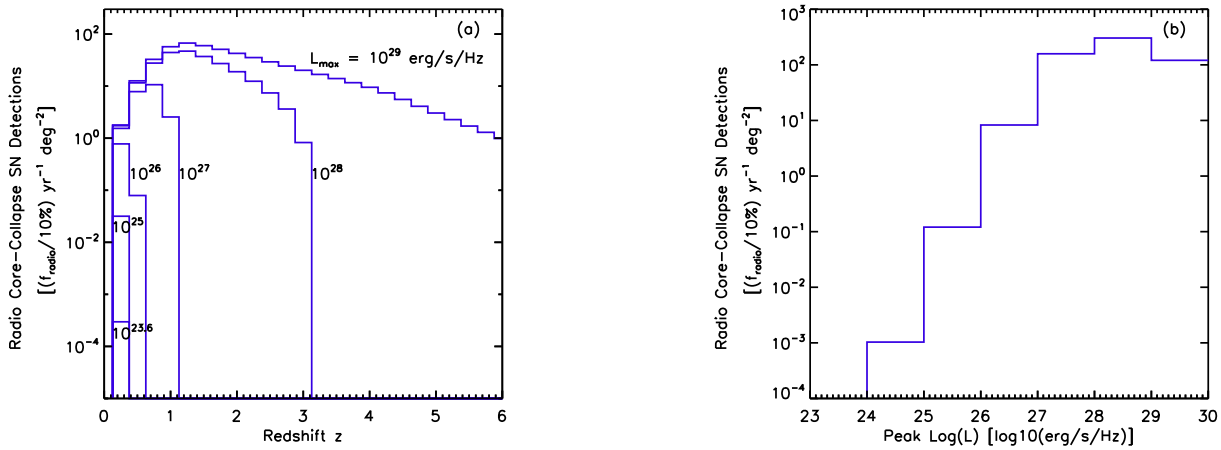

Figure 6.4: Core-collapse detection sensitivity to supernova radio luminosity, at 1.4 GHz, and for survey sensitivity $S_{\rm min} = 50$ nJy. (a)*Left Panel*: Supernova distribution over redshift, for different cutoffs for the luminosity function. (b)*Right Panel*: Supernova distribution in luminosity bins, integrated over all redshifts.

observed frequency ν can be tied to the corresponding luminosity threshold $L_{\rm min}^{\rm peak}$ by

$$L_{\rm min}^{\rm peak}(z;\nu_{\rm emit}) = \frac{4\pi D_L^2(z)}{(1+z)} S_{\rm min}^{\rm peak}(\nu_{\rm obs}), \tag{6.6}$$

where the luminosity distance is $D_L(z) = (1+z)\, c/H_0 \int_0^z dz' \, [\Omega_{\rm m}(1+z')^3+\Omega_\Lambda]^{-1/2}$. However, because the luminosity function we used is based on the peak luminosity at 5 GHz, we must find the corresponding luminosity threshold at this frequency by applying corrections based on the radio spectrum,

$$L^{\rm peak}_{\rm min,5GHz} = L^{\rm peak}_{\rm min} \, \frac{\int_{\rm 5GHz\ band} S^{\rm peak}(\nu_{\rm em})\ d\nu_{\rm em}}{\int_{\rm obs\ band} S^{\rm peak}[(1+z)\nu_{\rm obs}]\ d\nu_{\rm obs}}. \tag{6.7}$$

The detectable fraction resulting from survey sensitivity can therefore be estimated as

$$f_{\rm survey} = \int_{\log L^{\rm peak}_{\rm min,5GHz}} \Phi_{\rm 5GHz}(\log L)\, d\log L. \tag{6.8}$$

Figure. 6.2 plots the results of our predicted core-collapse RSN detection rate for different target survey sensitivities, $S_{\rm min}$. We adopt a benchmark frequency of 1.4 GHz because this will be one of the first major bands SKA deploys to observe neutral hydrogen. The related instantaneous field-of-view at 1.4 GHz of current SKA designs based on dish reflectors is approximately 1 deg^2, which we adopt. Fig. 6.2 plots the ideal core-collapse supernova rate for comparison (assuming infinite sensitivity but $f_{\rm radio} = 10\%$). One can see that the detection rate at 1 nJy is very close to the ideal rate in the universe.

Results for our fiducial SKA flux limit $S_{\rm min} = 50$ nJy are highlighted in Fig. 6.2. At this sensitivity, we see that we can expect that radio supernovae will be discovered (event rates > 5 RSN yr^{-1} deg^{-2}) over the enormous redshift range $z \simeq 0.5$ to 5. The total rate of RSNe expected in this entire redshift range is

$$\frac{dN_{\rm SN}}{dt\, d\Omega}(> 50 \text{ nJy}) \approx 620 \text{ RSNe yr}^{-1} \text{ deg}^{-2} \quad , \tag{6.9}$$

in good agreement with our above order-of-magnitude estimate. This sample size is large enough to be statistically useful and to allow for examination of the redshift history of RSNe. Moreover, out to $z \sim 1$, SKA will detect almost all cosmic RSNe in the field of view, while

at higher redshift the detections still comprise $> 10\%$ of the underlying ideal cosmic rate. For comparison, we also see that LSST will detect optical supernovae out to $z \lesssim 1$. Thus SKA will be complementary to LSST as a unique tool for cosmic supernova discovery.

Figure. 6.3 shows how core-collapse RSN detections vary for different observing frequencies, fixing a common survey sensitivity $S_{\rm min} = 50$ nJy and bandwidth $\Delta\nu = 1$ GHz. Results show similar numbers of detections at different bands, which is caused by a relatively flat spectrum shape at peak luminosities. Because SKA will be able to detect core-collapse RSNe out to high redshift $z \sim 5$, the frequency-redshift and time-dilation effects are significant. Weiler et al. (2002) noted that RSNe peak when the optical depth $\tau \sim 1$. Since the optical depth depends both on frequency and time with similar power index (Weiler et al., 2002), the frequency-redshift and time-dilation effects approximately cancel, so that a fixed observed frequency, the peak time is nearly redshift-independent.

As mentioned above, our luminosity function is likely biased toward the available bright events in a small and incomplete sample. To explore how this bias could affect our results, Fig. 6.4 shows how the detection rate with $S_{\rm min} = 50$ nJy at 1.4 GHz depends on core-collapse RSN luminosity. Fig. 6.4(a) shows that RSN with peak luminosities greater than 10^{27} erg s^{-1} Hz^{-1} contribute all of the detections beyond redshift $z \sim 1$, and RSN need to peak brighter than 10^{28} erg s^{-1} Hz^{-1} to be seen beyond $z \sim 3$. Fig. 6.4(b) similarly shows that the all-redshift detection rate becomes substantial for explosions peaking $> 10^{26}$ erg s^{-1} Hz^{-1}.

Type Ibc supernovae are of particular interest given their association with long gamma-ray bursts (GRBs; Galama et al., 1998; Woosley, 1993; Heger et al., 2003). Fig. 6.5 shows our predictions for Type Ibc detections of SKA per year per deg^2 at 1.4 GHz with a survey sensitivity of 50 nJy. The red curve shows the radio Type Ibc detections, assuming that Type Ibc represents 25% of core-collapse events (Li et al., 2011b), and $f_{\rm radio,Ibc} = 12\%$ with luminosity $\sim 10^{27}$ erg s^{-1} Hz^{-1} [10] (Berger et al., 2003). The blue curve shows the possible detections of the sub-class of Type Ibc supernovae that display extreme radio emission

[10]Here we simply assume a Gaussian distribution for the luminosity function centered at the specified luminosity with $\sigma = 1$.

and hence might be powered by central engines and related to GRBs. We assume that 0.5% of all Type Ibc supernovae are powered by central engines and have luminosities of $\sim 10^{29}$ erg s^{-1} Hz^{-1} (Berger et al., 2003). We adopted the spectrum of SN 1998bw, which is a Type Ic supernova (Weiler et al., 2002). Under these assumptions the SKA will be able to make unbiased, untargeted detections of ~ 130 radio Type Ibc supernovae per year per deg^2, and ~ 20 Type Ibc supernovae that might be connected to GRBs.

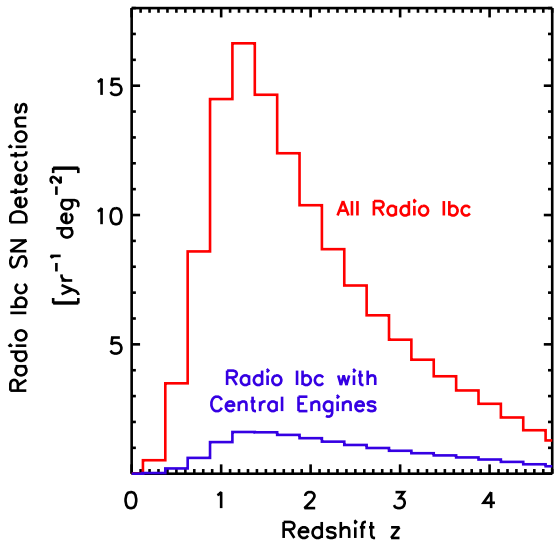

Figure 6.5: Predicted detection rate of Type Ibc supernovae as a function of redshift. In this plot we assume the sensitivity for SKA is $S_{\rm min} = 50$ nJy. The red curve shows all of the radio Ibc detections, assuming $f_{\rm radio,Ibc} = 12\%$ (Berger et al., 2003). The blue curve shows only the detection rate for Radio Ibc with central engines, assuming 0.5% of all of the Type Ibc RSNe are powered by central engines.

Finally, we turn to SKA precursors. The EVLA[11], a current leading-edge radio interferometer operating at centimeter wavelengths, is anticipated to reach a 1-σ rms noise of $\sigma_I \sim 1$ μJy or less in 10 hours, while SKA is expected to reach $\sigma_I \sim 50$ nJy in 10 hours. With data accumulated over repeated scans spanning over 1000 hours, an rms $\sigma_I \sim 5$ nJy may be reached. In synoptic surveys, we would expect EVLA to detect core-collapse events

[11]http://www.aoc.nrao.edu/evla

at a rate ~ 160 RSNe yr^{-1} deg^{-2} over a redshift range $z = 0.5$ to 3 (Fig. 6.2). A sample of this size over this redshift range will already mark a major advance in the study of cosmic RSNe, and further motivate the full SKA. ASKAP and MeerKAT are expected to have sensitivities comparable to that of EVLA (Johnston et al., 2009; de Blok et al., 2010), hence we would expect these to detect RSNe with similar rates and redshift reach.

6.4.2 Type Ia Supernovae

If all Type Ia RSNe are dimmer than the weakest limit presented in §6.2.2, the expected SKA detection rate is essentially zero. For example, if a typical Type Ia has a radio luminosity equal to the lowest published limit, $L = 8.1 \times 10^{24}$ erg s^{-1} Hz^{-1}, this can be seen with a sensitivity $S_{\rm min} = 50$ nJy out to a luminosity distance ~ 300 Mpc ($z \sim 0.08$). While ~ 3900 cosmic Ia events should occur per year out to this distance over the entire sky, $\ll 1$ events are expected in the SKA field of view. More optimistically, imagine a typical Type Ia radio luminosity is $L = 10^{26}$ erg s^{-1} Hz^{-1}, which is below $L = 4.2 \times 10^{26}$ erg s^{-1} Hz^{-1}, the highest published limit (Panagia et al., 2006); here the luminosity distance increases to ~ 1400 Mpc ($z \sim 0.28$). In this case, we find an SKA Type Ia detection rate ~ 0.5 yr^{-1} deg^{-2}, based on the local cosmic Type Ia rate derived from SDSS-II optical data (Dilday et al., 2010), $S_{\rm min} = 50$ nJy, and $f_{\rm radio} = 10\%$.[12] We see that even optimistically, we expect fewer than one event per SKA field-of-view per year. Even with $f_{\rm radio} = 100\%$, the detection rate is still only ~ 5 yr^{-1} deg^{-2}. Therefore we conclude that SKA will make few, if any, blind detections of Type Ia supernovae.

Targeted radio observations to follow up from nearby optical detections will probably be the best way to search for such events. For example, we expect 10 Type Ia events/year in the LSST sky within ~ 60 Mpc ($z \sim 0.015$). Type Ia (or core collapse!) events within this distance observed with $S_{\rm min} = 50$ nJy, would be detectable at luminosities $L \gtrsim 3.0 \times 10^{23}$ erg s^{-1} Hz^{-1}. Amusingly, this is close to the radio luminosity of SN 1987A.

[12] This also is implied by Fig. 6.4, which is for core-collapse events that have a higher cosmic rate.

6.5 Radio Survey Recommendations

A key requirement for detecting weak radio emission from CSM-supernovae interactions is improved radio interferometer sensitivity. High angular resolution – below an arcsecond at 1.4 GHz, (Weiler et al., 2004) – is also required to avoid natural confusion and to help identify supernovae against background galaxies. This is similar to the maximum EVLA angular resolution at 1.4 GHz. For comparison, the maximum anticipated SKA baseline length of 3000 km, producing angular resolution of 0.014 arcsecond at 1.4 GHz, is sufficient to distinguish different galaxies and also to resolve galaxies as extended sources within the observable universe with rms confusion limit of $<$ 3 nJy at 1.4 GHz (Carilli & Rawlings, 2004).

A key science goal of the SKA is to detect transient radio sources, both known (e.g. pulsars, GRBs), and as-yet unknown. This requires sophisticated transient detection and classification algorithms very likely running commensally with other large surveys planned by the SKA, such as the HI spectroscopic survey and deep continuum fields. We assume here that SKA transient detection algorithms will encompass automated detection of RSNe. For example, current parameterized models (Weiler et al., 1986, 1990; Montes et al., 1997; Chevalier, 1982a,b) based on available data predict patterns of spectral index evolution characteristic of supernovae in general, and supernova sub-types in particular. This information could be exploited for RSN detection, even potentially against a background of unrelated source variability. Broad frequency coverage is important in this regard (Weiler et al., 2004).

The SKA intrinsically is a high dynamic-range instrument, given the sensitivity implied by the large collecting area. The most demanding SKA science applications will require a dynamic range of 10^7:1. The detection of faint RSNe will require a dynamic range that falls within that envelope.

Although the lightcurves of RSNe show great diversity, the luminosities of core-collapse supernovae usually change much slower in radio than in optical. RSN lightcurves typically evolve on timescales of weeks to years; a useful lightcurve compilation appears in Stockdale

et al. (2007). Thus the minimum survey cadence (revisit periodicity) need not be any more frequent than this. Also, we have shown that core-collapse RSNe can be found out to high redshift with surveys pushing down to $S_{\rm min} = 50$ nJy. For SKA this corresponds to about 100 hours of exposure, in line with planned deep field exposures which are part of the key science. Thus, SKA as currently envisioned is well-suited to core-collapse discovery.

On the other hand, SKA probably will not have sufficient survey sensitivity for a volumetric search for Type Ia events, based on our current knowledge of the cosmic Type Ia rate and the upper limits in their luminosities set by the non-detection of these events. Follow-up observations from other wavelengths will likely be the best way to search for Type Ia RSNe.

The small volume of the local universe will limit nearby *untargeted* SKA detections of low-redshift core-collapse RSNe. We estimate only ~ 2 core-collapse RSN detections per year per square degree within redshift $z \sim 0.5$ (assuming a 50 nJy sensitivity at 1.4 GHz and $f_{\rm radio} = 10\%$). Unless SKA has large sky coverage comparable to those of optical surveys, it will be hard to get statistical information from such a small sample. Therefore, *targeted* radio followup of optically-confirmed nearby supernovae will be crucial to build a core-collapse RSN "training set" database needed for refining automatic identification and classification techniques.

With detection methods optimized based on low-z radio data for optically-identified events, radio surveys can then be used to independently detect core-collapse RSNe at high redshift based only on their radio emission. As shown in Fig. 6.2, supernova searches at high redshift ($z \gtrsim 1$) will largely rely on radio synoptic surveys, the inverse of the strategy proposed above for low-redshift domain. Surveys for core-collapse RSNe will likely not be synoptic all-sky surveys due to operational limitations, but will likely proceed in a limited set of sub-fields, visited over an hierarchical set of cadences to cover a range of time-scales for general transient phenomena and multiple commensal science objectives. It is also important to match core-collapse RSNe survey sky coverage and cadence to that used in complementary optical surveys. LSST will repeatedly scan the whole sky every ~ 3 days. Thus a cadence

~ 1 week for RSNe sub-fields will be preferred for an SKA core-collapse supernova survey.

6.6 Discussion and Conclusions

SKA's capability for unbiased synoptic searches over large fields of view will revolutionize the discovery of radio transients in general and core-collapse RSNe in particular (Gal-Yam et al., 2006). The unprecedented sensitivity of SKA could allow detection of core-collapse RSNe out to a redshift $z \sim 5$. These detections will be *unbiased* and *automatic* in that they can occur anywhere in the large SKA field of view without need for targeting based on prior detection at other wavelengths. With SKA, the core-collapse RSN inventory should increase from the current number of several dozen to $\sim 620\ \mathrm{yr}^{-1}\ \mathrm{deg}^{-2}$. EVLA should detect $\sim 160\ \mathrm{yr}^{-1}\ \mathrm{deg}^{-2}$, and other SKA precursors should reap similarly large RSN harvests. In contrast, intrinsically dim RSNe such as Type Ia events and 1987A-like core-collapse explosions are unlikely to be found blindly. However, the SKA (and precursor) sensitivities will offer the possibility of detecting these events via *targeted* followup of discoveries by optical synoptic surveys such as LSST.

The science payoff of large-scale RSNe searches touches many areas of astrophysics and cosmology. We conclude with examples of possible science applications with the new era of RSN survey. However, the true potential of untargeted radio search is very likely beyond what we mention.

Non-prompt RSN emission requires the presence of circumstellar matter, so such surveys will probe this material and the pre-supernova winds producing it. For core-collapse supernovae, pre-supernova winds should depend on the metallicities of the progenitor stars (Leitherer et al., 1992; Kudritzki & Puls, 2000; Vink et al., 2001; Mokiem et al., 2007), and should be weaker in metal-poor environments with lower opacities in progenitor atmospheres. This effect should lead to correlations between RSN luminosity and host metallicity, as well as an evolution of the RSN luminosity function towards lower values at higher redshifts. For

Type Ia supernovae, the mass-loss rate from the progenitors depends on the nature of the binary system, i.e., single or double degenerate (Nomoto et al., 1984; Iben & Tutukov, 1984; Webbink, 1984). Radio detection of Type Ia supernovae will probe the mass and density profile of the surrounding environment and hence be valuable for studying Type Ia physics (Eck et al., 1995; Panagia et al., 2006; Chomiuk et al., 2011).

Large-scale synoptic RSNe surveys will complement their optical counterparts. While optical surveys such as LSST will provide very large supernova statistics at $z \lesssim 1$, radio surveys will be crucial for detections at higher redshifts. The nature and evolution of dust obscuration presents a major challenge for optical supernova surveys and supernova cosmology. Current studies suggest dust obscuration increases rapidly with redshift, but uncertainties are large. Mannucci et al. (2007) estimate that optical surveys may miss $\sim 60\%$ of core-collapse supernovae and $\sim 35\%$ of Type Ia supernovae at redshift $z \sim 2$. RSN observations, in contrast, are essentially unaffected by dust. Thus, high-redshift supernovae could be detected at radio wavelengths but largely missed in counterpart optical searches. Comparing supernova detections in both optical and radio will provide a new and independent way to measure dust dependence on redshift. In particular, SKA will be a powerful tool to directly detect supernovae in dust-obscured regions at large redshift, and therefore offer what may be the only means to study the total supernovae rate, star-formation, and dust behavior in these areas.

Additionally, radio surveys will reveal rare and exotic events. For example, some Type Ibc supernovae are linked to long GRBs (Galama et al. 1998; and see reviews in Woosley & Bloom, 2006; Gehrels et al., 2009), probably via highly relativistic jets powered by central engines and will manifest themselves in extremely luminous radio emission (Woosley, 1993; Iwamoto et al., 1998; Li & Chevalier, 1999; Woosley et al., 1999; Heger et al., 2003). Thus one might expect radio surveys to preferentially detect more Type Ibc supernovae than other supernova types. An unbiased sample of Type Ibc RSNe will provide new information about the circumstellar environments of these explosions and thus probe the mass-loss effects

believed to be crucial to the Ibc pre-explosion evolutionary path (Price et al., 2002; Soderberg et al., 2004, 2006a; Crockett et al., 2007; Wellons & Soderberg, 2011); in addition, a large sample of Ibc RSNe will allow systematic study of the differences, if any, between those which do an do not host GRBs (Berger et al., 2003; Soderberg et al., 2006b; Soderberg, 2007).

Furthermore, radio surveys give unique new insight into a possible class of massive star deaths via direct collapse into black holes, with powerful neutrino bursts but no electromagnetic emission (MacFadyen & Woosley, 1999; Fryer, 1999; MacFadyen et al., 2001; Heger et al., 2003). These "invisible collapses" can be probed by comparing supernovae detected electromagnetically and the diffuse background of cosmic supernova neutrinos (Lien et al., 2010, and references therein). By revealing dust-enshrouded SNe, radio surveys will make this comparison robust by removing the degeneracy between truly invisible events and those which are simply optically obscured. Indeed, direct collapse events without explosions but with relativistic jets are candidates for GRB progenitors. A comparison among RSNe, optical supernovae, GRBs, and neutrino observations will provide important clues to the physics of visible and invisible collapses, and their relation with GRBs.

We thus believe that a synoptic survey in radio wavelengths will be crucial in many fields of astrophysics, for it will bring the first complete and unbiased RSN sample and systematically explore exotic radio transients. SKA will be capable of performing such an untargeted survey with its unprecedented sensitivity. Our knowledge of supernovae will thus be firmly extended into the radio and to high redshifts.

6.7 Acknowledgments

We thank Kurt Weiler, Christopher Stockdale, and Shunsaku Horiuchi for encouragement and illuminating conversations. We are also grateful to Joseph Lazio for helpful comments that have improved this paper.

Chapter 7

Conclusions and Future Work

7.1 Discussion and Conclusions

The Standard Model "Foregrounds" in nuclear and particle astrophysics are interesting by themselves as sites of interesting and often extreme astrophysics. In addition, it is critical to understand them in order to be able to disentangle them from signatures of new physics and astrophysics. The lithium problem is a classic case in point in the early universe. The effect of standard nuclear physics needs to be disentangled from more exotic particle physics effects. The search for nuclear resonances that can destroy ^{7}Li or ^{7}Be effectively represents an effort to do this. The production reactions are very well understood leaving no room for any addition or modification to the production network. So the destruction reactions are the only options. The result of the study revealed that despite the large number of apriori possible resonance channels involving n,p, d, t, ^{3}He, ^{4}He bombarding and destroying ^{7}Li and ^{7}Be nuclei, very few channels have rates high enough to bring the abundances of ^{7}Li down to observed values. After systematically scanning the space of resonance strengths and energies, only three candidate resonances remain and are enlisted once again here in the table 7.1.

This work along with few others (For e.g., Cyburt & Pospelov, 2012; Boyd et al., 2010a), prompted experiments (Kirsebom & Davids, 2011; O'Malley et al., 2011; Charity et al., 2011) to look for these resonances. These experiments have essentially ruled out the possibility of these resonances solving the lithium problem (Coc, 2013). This strengthens the exciting possibility of the lithium discrepancy being an indication of new physics beyond the Standard

Compound Nucleus, J^π, E_{ex}	Initial State	L_{init}	L_{fin}	E_{res}	Γ_{tot}	Exit Channels	Exit Channel Width
^{9}B, $(5/2^+)$, 16.71 MeV	$^7\mathrm{Be} + d$	1	0	219.9 keV	unknown	$p + {}^8\mathrm{Be}^*$ (16.63 MeV)	unknown
			1			$\alpha + {}^5$Li	unknown
^{10}B, 2^+, 18.80 MeV	$^7\mathrm{Be} + t$	1	1	130.9 keV	< 600 keV	$p + {}^9\mathrm{Be}^*$ (11.81 MeV)	unknown
			1			^{3}He	unknown
			2			α	unknown
^{10}C, unknown	$^7\mathrm{Be} + {}^3\mathrm{He}$	unknown	unknown	unknown	unknown	p	unknown
			unknown	($Q = 15.003$ MeV)		α	unknown
						^{3}He (elastic)	unknown

Table 7.1: This table lists surviving candidate resonances.

Model. Of course, the possibility of a refined interpretation of the observational data to reconcile with theoretical predictions, in terms of improved models of stellar atmospheres is also very promising.

The study of properties of cosmic gamma-ray sources has been a very interesting one. The computation of the inverse-Compton emission from star forming galaxies shows that it is subdominant compared to pionic emission in most of the *Fermi* -LAT range of energies, unless starburst galaxies have a much higher e/p ratio compared to normal galaxies, suggested by some groups (Lacki et al., 2011). Aside from this caveat, it appears that the gamma-ray emission from star forming galaxies is dominated by the pionic emission. This is in the pure luminosity evolution model where only the luminosity of the galaxies evolves with redshift and not the number density. In the pure density evolution case, the pionic emission is nearly 4 times weaker than the pure luminosity evolution for normal galaxies (Fields et al., 2010). The linear scaling of the inverse-Compton emission with the star formation rate, implies that the IC result remains the same as in the pure luminosity evolution case. And hence for normal galaxies, the pionic emission will dominate in either case. For starbursts this is not as obvious. According to high e/p models (Lacki et al., 2011) consistent with low values of magnetic fields ($50\mu G$ instead of $300\mu G$), the IC emission can dominate over the pionic emission at *Fermi* -LAT energies.

From the overall gamma-ray intensity of star forming galaxies as a function of energy, they are a guaranteed and potentially significant contribution. And this is a subject of ongoing

research. However, it leaves the possibility of other sources as blazars also contributing competitively (Stecker & Venters, 2011), particularly at high energies. This means that it is important to have other "tie-breakers" to answer the question of relative contribution of these sources to the diffuse EGB. This provides strong motivation to look at photon statistics of these sources as a possible tie-breaker. From the preliminary results, it seems inevitable that a EGB has a uniformly, multicomponent origin. That is both blazars and star forming galaxies contribute without either one being dominant. This includes photons from resolved as well as unresolved sources. The star-forming galaxies being numerous but dim produce a largely Poisson distribution of photon counts. This is of course, contaminated by an irreducible Poisson emission from the Galaxy. Thus, the normalisation of the Poisson component represents an upper limit to the contribution of star forming galaxies. The blazars on the other hand being brighter but less numerous, are capable of producing high count pixels. As a result, their photon distribution has a high count tail. This is a distinguishing signature between star forming galaxies and blazars. Preliminary results indicate that blazars contribute to 21% of all the photons consistent with other analyses (Malyshev & Hogg, 2011; Abdo et al., 2010l) including the LAT team's own analysis.

Gamma-ray and X-ray polarimetry represents the next frontier in high energy astronomy. The objects of interest here in this research and sources of cosmic rays in general are promising targets for future generations of polarimeters. Blazars and GRBs are in particular the most exciting ones. This is because, they are both touted as candidates for producing ultra high energy cosmic rays. And in general, they are regarded as the most powerful particle accelerators in the universe. The accelerator properties are intimately tied to the high energy emission mechanisms probed by polarimetry. Despite the fact that the polarimeters are at most in the soft gamma-ray energy range, the relations between different energy bands from energy exchanges through various radiative processes obeying energy conservation (Becker, 2008), implies that polarimetry can potentially constrain cosmic ray related emission mechanisms. Polarised emission from GRBs has been measured by SPI on INTEGRAL (For eg

Götz et al., 2009), albeit for very few sources. Blazars on the other hand may require much more sensitive space based polarimeters to be detected in this domain. Furthermore, polarised emission should largely trace the leptonic emission as inverse-Compton scattering of low energy photons by electrons and synchrotron emission are likely to be the most important mechanisms producing polarised X-rays and soft gamma-rays. And both synchrotron and IC with different degrees of polarisation, can be distinguished by high energy polarisation. Hadronic emission on the other hand, dont lead to polarised emission for the processes involving primary particles or reactions. The secondary electrons produced from hadronic processes are however capable of producing polarised emission like for the primary leptons, however with a different spectrum. Through the secondary leptonic emission polarised emission can indirectly probe hadronic processes. It could also therefore be potentially related to neutrinos.

7.2 Future work

Naturally one of the promising future directions is the science of high energy polarimetry. Observationally, estimating what fraction of blazars and GRBs would be discovered by future generations of polarimeters, is one obvious goal. This involves doing feasibility studies, optimising detection strategies, and hopefully eventually proposing for actual observations. Theoretically, studying the emission mechanisms of both blazars and GRBs is a major challenge primarily in details of the various competing models. But chosing models that can make predictions testable by future polarisation missions would be one way to approach this task. Incorporating the multimessenger approach by connecting to neutrinos is an exciting avenue.

I will join the HESS and CTA collaborations. This provides an opportunity to extend my gamma-ray experience to very high energies. Once again these are testing grounds for some of those very objects that have been of interest to me during my thesis. Cosmic

accelerators like star forming galaxies, blazars, GRBs, etc. are all very interesting at TeV energies. Properties of individual sources like spectra of galaxies both active and otherwise, flaring of blazars, etc. are areas of exciting research with the improved sensitivity of HESS II. Furthermore, the possibility of testing the line emission from dark matter with HESS II is extremely exciting.

Thus, I wish to continue to explore particle astrophysics with newer tools and methods.

Appendix A

A.1 The Narrow Resonance Approximation

Consider a reaction $A + b \rightarrow C^* \rightarrow c + D$, which passes through an excited state of the compound nucleus C^*. We treat separately normal and subthreshold reactions, defined respectively by a positive and negative sign of the resonance energy $E_{\rm res} = E_{\rm ex} - Q_C$, where $E_{\rm ex}$ is the excitation energy of the C^* state considered, and $Q_C = \Delta(A) + \Delta(B) - \Delta(C^*)$.

In general, the thermally averaged rate is

$$\langle \sigma v \rangle = \frac{\int d^3v \; e^{-\mu v^2/2T} \sigma v}{\int d^3v \; e^{-\mu v^2/2T}} = \sqrt{\frac{8}{\pi \mu}} \; T^{-3/2} \int_0^\infty dE \; E \; \sigma(E) e^{-E/T} \tag{A.1}$$

For a Breit-Wigner resonance with widths not strongly varying with energy, this becomes

$$\langle \sigma v \rangle = \frac{4\pi\omega\Gamma_{\rm init}\Gamma_{\rm fin}}{(2\pi\mu T)^{3/2}} \int_0^\infty dE \frac{e^{-E/T}}{(E - E_{\rm res})^2 + (\Gamma_{\rm tot}/2)^2} \tag{A.2}$$

Thus the thermal rate is controlled by the integral of the Lorentzian resonance profile modulated with the exponential Boltzmann factor.

The narrow resonance approximation has usually only been applied to the normal resonance case, and assumes that the total resonance width is small compared to the temperature: $\Gamma_{\rm tot} \ll T$.

A.1.1 Narrow Normal Resonances

In the normal or "superthreshold" case, the integral includes the peak of the Lorentzian where $E = E_{\rm res}$. The narrow condition then guarantees that over the Lorentzian width, the Boltzmann factor does not change appreciably, and so we make the approximation

$$\exp\left(-\frac{E}{T}\right) \approx \exp\left(-\frac{\hat{E}}{T}\right) \tag{A.3}$$

where we choose the "typical" energy to be the peak of the Lorentzian, $\hat{E} = E_{\rm res}$. Then the integral becomes

$$\langle \sigma v \rangle_{\Gamma_{\rm tot} \ll T} \approx \frac{\omega \Gamma_{\rm init} \Gamma_{\rm fin}}{2(2\pi\mu T)^{3/2}} e^{-E_{\rm res}/T} \int_0^\infty dE \frac{1}{(E - E_{\rm res})^2 + (\Gamma_{\rm tot}/2)^2} \tag{A.4}$$

Furthermore, it is usually also implicitly assumed that the resonance energy is large compared to the width: $E_{\rm res} \gg \Gamma_{\rm tot}$. Then the integral gives $2\pi/\Gamma_{\rm tot}$, and the thermally averaged cross-section under this approximation is given by Angulo et al. (1999),

$$\begin{aligned} \langle \sigma v \rangle_{\Gamma_{\rm tot} \ll T, E_{\rm res}} &= \omega\ \Gamma_{\rm eff} \left(\frac{2\pi}{\mu T}\right)^{3/2} e^{-E_{\rm res}/T} & \text{(A.5)} \\ &= 2.65 \times 10^{-13} \mu^{-3/2}\ \omega\ \Gamma_{\rm eff}\ T_9^{-3/2} \exp(-11.605\ E_{\rm res}/T_9)\ {\rm cm^3 s^{-1}} & \text{(A.6)} \end{aligned}$$

where the latter expression has $T_9 = T/10^9$ K.

Note however, that eq. (A.2) is exactly integrable as it stands and does not require we make the usual $E_{\rm res} \gg \Gamma_{\rm tot}$ approximation. Thus for the normal case we modify the usual reaction rate and instead adopt the form

$$\langle \sigma v \rangle_{\rm narrow,normal} = \langle \sigma v \rangle_{\Gamma_{\rm tot} \ll T, E_{\rm res}}\ f(2E_{\rm res}/\Gamma_{\rm tot}) \tag{A.7}$$

Here we introduce a temperature-independent correction for finite $E_{\rm res}/\Gamma_{\rm tot}$ (still with $E_{\rm res} >$

0)

$$f(u) = \frac{1}{2} + \frac{1}{\pi} \arctan u \quad . \tag{A.8}$$

This factor spans $f \to 1/2$ for $E_{\rm res} \ll \Gamma_{\rm tot}$ to $f \to 1$ for $E_{\rm res} \gg \Gamma_{\rm tot}$.

In practice, we adopt a slightly modified version of the correction factor in our plots. Recall that in Figs. 2.2–2.9, we show results for lithium abundances in the presence of resonant reactions with fixed input channels, but without reference to a specific final state. Without the correction factor, the resonant reaction rate is characterized by two parameters, $E_{\rm res}$ and $\Gamma_{\rm eff}$. These two parameters are insufficient to specify the correction factor, which depends on $E_{\rm res}/\Gamma_{\rm tot}$. Rather than separately introduce $\Gamma_{\rm tot}$, we instead approximate the correction factor as $f(2E_{\rm res}/\Gamma_{\rm eff})$. Because $\Gamma_{\rm eff} < \Gamma_{\rm tot}$ and f is monotonically increasing, this always *underestimates* the value of f and thus conservatively *understates* the importance of the resonance we seek (but the approximation is never off by more than a factor of 2 in the normal case).

A.1.2 Narrow Subhreshold Resonances

Still making the narrow resonance approximation $\Gamma_{\rm tot} \ll T$, we now turn to the subthreshold case, in which $E_{\rm res} < 0$. To make effect of the sign change explicit, we rewrite eq. (A.2) as

$$\langle \sigma v \rangle = \frac{\omega \Gamma_{\rm init} \Gamma_{\rm fin}}{2(2\pi\mu T)^{3/2}} \int_0^\infty dE \frac{e^{-E/T}}{(E + |E_{\rm res}|)^2 + (\Gamma_{\rm tot}/2)^2} \tag{A.9}$$

Now the integrand always excludes the resonant peak, and only includes the high-energy wing. As with the normal case, the narrowness of the resonance implies that the Boltzmann exponential does not change much where the Lorentzian has a significant contribution, and so we again will approximate $e^{-E/T} \approx e^{-\hat{E}/T}$. Since we avoid the resonant peak, the choice of $\hat{E}$ not as straightforward in the subthreshold case where we took $\hat{E} = E_{\rm res}$. This choice makes no sense in the subthreshold case, because the $e^{-E_{\rm res}/T} > 1$ in the subthreshold case, yet obviously kinetic energy $E > 0$ and thus the Boltzmann factor must always be a suppression

and not an enhancement!

Yet clearly $|E_{\rm res}|$ remains an important scale. Thus we put $\hat{E} = \hat{u}|E_{\rm res}|$, and we have examined results for different values of the dimensionless parameter $\hat{u}$. We find good agreement with numerical results when we adopt $\hat{u} \approx 1$, i.e., $\hat{E} = |E_{\rm res}|$. Thus for the subthreshold case we adopt a reaction rate which is in closely analogous to the normal case:

$$\langle \sigma v \rangle_{\rm narrow,\,subthreshold} = \omega\ \Gamma_{\rm eff} \left(\frac{2\pi}{\mu T} \right)^{3/2} e^{-|E_{\rm res}|/T} f\left(-2|E_{\rm res}|/\Gamma_{\rm tot}\right) \tag{A.10}$$

Similarly to the normal case, as the reaction becomes increasingly off-resonance, i.e., as $|E_{\rm res}|$ grows, there is an exponential suppression. In addition, the correction factor has limits $f \to 1/2$ for $|E_{\rm res}| \ll \Gamma_{\rm tot}$, and $f \to 0$ as $|E_{\rm res}| \gg \Gamma_{\rm tot}$. Finally, note that, as a function of $E_{\rm res}$, our subthreshold and normal rates match at $E_{\rm res} = 0$, as they must physically.

Appendix B

B.1 The energy loss rates

The energy losses other than IC are bremsstrahlung, synchrotron and ionisation. They are expressed as follows (Hayakawa, 1973; Ginzburg, 1979): synchrotron losses

$$\begin{aligned} b_{\rm sync}(E_{\rm e}) &= \frac{4}{3}\sigma_{\rm T}\ c\ U_{\rm mag}\left(\frac{E_{\rm e}}{m\ c^2}\right)^2 = \frac{1}{6\ \pi}\sigma_{\rm T}\ cB^2\left(\frac{E_{\rm e}}{m}\right)^2 \\ &\approx 3\times10^{-10}\ {\rm GeV\ sec^{-1}}\ \left(\frac{B}{1\ \mu{\rm G}}\right)^2\ \left(\frac{E_{\rm e}}{10\ {\rm TeV}}\right)^2 \end{aligned} \tag{B.1}$$

are controlled by the interstellar magnetic energy density $U_{\rm mag}$. The bremsstrahlung losses depend on whether the medium is ionised or neutral. Due to the presence of both H I and H II, the bremsstrahlung losses are due to both neutral and ionised hydrogen (Hayakawa, 1973; Ginzburg, 1979):

$$b_{\rm brem}(E_{\rm e}) = b_{\rm brem,ion}(E_{\rm e}) + b_{\rm brem,n}(E_{\rm e}) \tag{B.2}$$

$$b_{\rm brem,ion}(E_{\rm e}) = \frac{3}{\pi}\ n_{\rm H\ II}\ \alpha\ \sigma_{\rm T}\ c\ E_{\rm e}\left[\ln\left(\frac{2\ E_{\rm e}}{m\ c^2}\right) - \frac{1}{3}\right] \tag{B.3}$$

$$\begin{aligned} &= 1.37\times10^{-12}\ {\rm GeV\ sec^{-1}}\left(\frac{n_{\rm H\ II}}{1\ {\rm cm^{-3}}}\right) \\ &\quad\times\left(\frac{E_{\rm e}}{10\ {\rm TeV}}\right)\left[\ln\left(\frac{E_{\rm e}}{10\ {\rm TeV}}\right) + 17.2\right] \end{aligned} \tag{B.4}$$

$$b_{\mathrm{brem,n}}(E_{\mathrm{e}}) = \frac{3}{\pi}\, n_{\mathrm{H\ I}}\, \alpha\, \sigma_{\mathrm{T}}\, c\, E_{\mathrm{e}} \left[\ln(191) + \frac{1}{18}\right] \tag{B.5}$$

$$= 7.3 \times 10^{-12}\ \mathrm{GeV\ sec^{-1}} \left(\frac{n_{\mathrm{H\ I}}}{1\ \mathrm{cm^{-3}}}\right) \left(\frac{E_{\mathrm{e}}}{10\ \mathrm{TeV}}\right) \tag{B.6}$$

Here $n_{\mathrm{H\ I}}$ and $n_{\mathrm{H\ II}}$ are the number density of relativistic electrons in the interstellar medium, which is equal to the number density of H I and H II.

References

Abazajian, K. N., Blanchet, S., & Harding, J. P. 2011, Physical Review D, 84, 103007

Abdo, A. A., Ackermann, M., Ajello, M., et al. 2009, Physical Review Letters, 103, 251101

—. 2010a, ApJ, 709, L152

—. 2010b, ApJ, 709, L152

—. 2010c, A&A, 523, A46

—. 2010d, A&A, 523, A46

—. 2010e, The Astrophysical Journal, 723, 1082

—. 2010f, A&A, 523, L2

—. 2010g, A&A, 523, L2

—. 2010h, A&A, 512, A7

—. 2010i, A&A, 512, A7

—. 2010j, Physical Review Letters, 104, 101101

—. 2010k, Physical Review Letters, 104, 101101

—. 2010l, The Astrophysical Journal, 720, 435

Abdo, A. A., Ackermann, M., Agudo, I., et al. 2010m, The Astrophysical Journal, 716, 30

Acero, F., Aharonian, F., Akhperjanian, A. G., et al. 2009, Science, 326, 1080

Ackermann, M., Ajello, M., Albert, A., et al. 2012a, Physical Review D, 85, 083007

—. 2012b, Physical Review D, 86, 022002

Ackermann, M., Ajello, M., Allafort, A., et al. 2012c, The Astrophysical Journal, 755, 164

Adahchour, A., & Descouvemont, P. 2003, Journal of Physics G Nuclear Physics, 29, 395

Agudo, I., Thum, C., Wiesemeyer, H., & Krichbaum, T. P. 2010, ApJS, 189, 1

Ahlers, M., Mertsch, P., & Sarkar, S. 2009, Physical Review D, 80, 123017

Ajzenberg-Selove, F. 1990, Nuclear Physics A, 506, 1

Ando, S., Cyburt, R. H., Hong, S. W., & Hyun, C. H. 2006, Physical Review C, 74, 025809

Ando, S., & Komatsu, E. 2006, Physical Review D, 73, 023521

Ando, S., Komatsu, E., Narumoto, T., & Totani, T. 2007, Physical Review D, 75, 063519

Ando, S., & Pavlidou, V. 2009, *Mon. Not. Roy. Astron. Soc.*, 400, 2122

Angulo, C., Arnould, M., Rayet, M., et al. 1999, Nuclear Physics A, 656, 3

Angulo, C., Casarejos, E., Couder, M., et al. 2005, ApJ, 630, L105

Asplund, M., Lambert, D. L., Nissen, P. E., Primas, F., & Smith, V. V. 2006, The Astrophysical Journal, 644, 229

Baklanov, P. V., Blinnikov, S. I., & Pavlyuk, N. N. 2005, Astronomy Letters, 31, 429

Bania, T. M., Rood, R. T., & Balser, D. S. 2002, Nature, 415, 54

Bazin, G., Palanque-Delabrouille, N., Rich, J., et al. 2009, A&A, 499, 653

Becker, J. K. 2008, Phys. Rep., 458, 173

Berger, E., Kulkarni, S. R., Frail, D. A., & Soderberg, A. M. 2003, The Astrophysical Journal, 599, 408

Bignami, G. F., Fichtel, C. E., Hartman, R. C., & Thompson, D. J. 1979, The Astrophysical Journal, 232, 649

Blinov, D., Myserlis, I., Angelakis, E., King, O., & Pavlidou, V. 2013, The Astronomer's Telegram, 4779, 1

Blumenthal, G. R., & Gould, R. J. 1970, Reviews of Modern Physics, 42, 237

Bonifacio, P. 2002, A&A, 395, 515

Bonifacio, P., Pasquini, L., Spite, F., et al. 2002, A&A, 390, 91

Bonometto, S., Cazzola, P., & Saggion, A. 1970, A&A, 7, 292

Botticella, M. T., Riello, M., Cappellaro, E., et al. 2008, A&A, 479, 49

Boyd, R. N., Brune, C. R., Fuller, G. M., & Smith, C. J. 2010a, Physical Review D, 82, 105005

—. 2010b, Physical Review D, 82, 105005

Brecher, K., & Morrison, P. 1967, ApJ, 150, L61

Bringmann, T., Donato, F., & Lineros, R. A. 2012, *JCAP*, 1, 49

Cappellaro, E., Evans, R., & Turatto, M. 1999, A&A, 351, 459

Cappellaro, E., Riello, M., Altavilla, G., et al. 2005, A&A, 430, 83

Caraveo, P. A., Bennett, K., Bignami, G. F., et al. 1980, A&A, 91, L3

Carilli, C. L., & Rawlings, S. 2004, New Astronomy Review, 48, 979

Caughlan, G. R., & Fowler, W. A. 1988, Atomic Data and Nuclear Data Tables, 40, 283

Chakraborty, N., & Fields, B. D. 2012, ArXiv e-prints

Chakraborty, N., Fields, B. D., & Olive, K. A. 2011, Physical Review D, 83, 063006

Chang, Z., Jiang, Y., & Lin, H. N. 2013, ArXiv e-prints

Charity, R. J., Elson, J. M., Manfredi, J., et al. 2011, Physical Review C, 84, 014320

Chevalier, R. A. 1982a, ApJ, 259, L85

—. 1982b, The Astrophysical Journal, 259, 302

—. 1998, The Astrophysical Journal, 499, 810

Chomiuk, L., Soderberg, A. M., Chevalier, R., Badenes, C., & Fransson, C. 2011, in Bulletin of the American Astronomical Society, Vol. 43, American Astronomical Society Meeting Abstracts #217, #304.05

Cirelli, M., & Panci, P. 2009, Nuclear Physics B, 821, 399

Coc, A. 2013, Journal of Physics Conference Series, 420, 012136

Coc, A., Nunes, N. J., Olive, K. A., Uzan, J.-P., & Vangioni, E. 2007, Physical Review D, 76, 023511

Coc, A., Vangioni-Flam, E., Descouvemont, P., Adahchour, A., & Angulo, C. 2004a, The Astrophysical Journal, 600, 544

—. 2004b, The Astrophysical Journal, 600, 544

Coleman, S., & Glashow, S. L. 1999, Physical Review D, 59, 116008

Crockett, R. M., Smartt, S. J., Eldridge, J. J., et al. 2007, *Mon. Not. Roy. Astron. Soc.*, 381, 835

Cuoco, A., Iocco, F., Mangano, G., et al. 2004, International Journal of Modern Physics A, 19, 4431

Cyburt, R. H. 2004a, Physical Review D, 70, 023505

—. 2004b, Physical Review D, 70, 023505

Cyburt, R. H., & Davids, B. 2008, Physical Review C, 78, 064614

Cyburt, R. H., Ellis, J., Fields, B. D., et al. 2010, *JCAP*, 10, 32

Cyburt, R. H., Ellis, J., Fields, B. D., Olive, K. A., & Spanos, V. C. 2006, *JCAP*, 11, 14

Cyburt, R. H., Fields, B. D., & Olive, K. A. 2001, New Astronomy, 6, 215

—. 2003, Physics Letters B, 567, 227

—. 2004, Physical Review D, 69, 123519

—. 2008, *JCAP*, 11, 12

Cyburt, R. H., Fields, B. D., Olive, K. A., & Skillman, E. 2005, Astroparticle Physics, 23, 313

Cyburt, R. H., & Pospelov, M. 2012, International Journal of Modern Physics E, 21, 50004

Dahlen, T., Strolger, L., & Riess, A. G. 2010, in Bulletin of the American Astronomical Society, Vol. 42, American Astronomical Society Meeting Abstracts #215, #430.23

Dahlen, T., Strolger, L.-G., & Riess, A. G. 2008, The Astrophysical Journal, 681, 462

Dahlen, T., Strolger, L.-G., Riess, A. G., et al. 2004, The Astrophysical Journal, 613, 189

de Blok, E. W. J. G., Booth, R., Jonas, J., & Fanaroff, B. 2010, in ISKAF2010 Science Meeting

de Cea del Pozo, E., Torres, D. F., & Rodriguez Marrero, A. Y. 2009, The Astrophysical Journal, 698, 1054

Dean, A. J., Clark, D. J., Stephen, J. B., et al. 2008, Science, 321, 1183

Dermer, C. D., Ramirez-Ruiz, E., & Le, T. 2007, ApJ, 664, L67

Dilday, B., Smith, M., Bassett, B., et al. 2010, The Astrophysical Journal, 713, 1026

Dmitriev, V. F., Flambaum, V. V., & Webb, J. K. 2004, Physical Review D, 69, 063506

Doert, M., Becker, J. K., Halzen, F., O'Murchadha, A., & Rhode, W. 2012, Journal of Physics Conference Series, 355, 012039

Eck, C. R., Cowan, J. J., Roberts, D. A., Boffi, F. R., & Branch, D. 1995, ApJ, 451, L53

Ellis, J., Farakos, K., Mavromatos, N. E., Mitsou, V. A., & Nanopoulos, D. V. 2000, The Astrophysical Journal, 535, 139

Ellis, J., Olive, K. A., & Vangioni, E. 2005, Physics Letters B, 619, 30

Esmailzadeh, R., Starkman, G. D., & Dimopoulos, S. 1991, The Astrophysical Journal, 378, 504

Faucher-Giguère, C.-A., & Loeb, A. 2010, *JCAP*, 1, 5

Felten, J. E. 1965, Physical Review Letters, 15, 1003

Felten, J. E., & Morrison, P. 1963, Physical Review Letters, 10, 453

Fermi-LAT Collaboration. 2013, ArXiv e-prints

Fichtel, C. E., Hartman, R. C., Kniffen, D. A., et al. 1975, The Astrophysical Journal, 198, 163

Fields, B. D., Pavlidou, V., & Prodanović, T. 2010, ApJ, 722, L199

Frieman, J. A., Bassett, B., Becker, A., et al. 2008, The Astronomical Journal, 135, 338

Fryer, C. L. 1999, The Astrophysical Journal, 522, 413

Fujiwara, M., Matsuoka, Y., & Ienaka, N. 2012, The Astronomical Journal, 144, 112

Fumagalli, M., O'Meara, J. M., & Prochaska, J. X. 2011, Science, 334, 1245

Gal-Yam, A., Fox, D. B., Price, P. A., et al. 2006, Nature, 444, 1053

Galama, T. J., Vreeswijk, P. M., van Paradijs, J., et al. 1998, Nature, 395, 670

Gehrels, N., Ramirez-Ruiz, E., & Fox, D. B. 2009, ARA&A, 47, 567

Geringer-Sameth, A., & Koushiappas, S. M. 2012, *Mon. Not. Roy. Astron. Soc.*, 421, 1813

Ginzburg, V. L. 1979, Theoretical physics and astrophysics (Oxford: Pergamon)

González Hernández, J. I., Bonifacio, P., Caffau, E., et al. 2009, A&A, 505, L13

Götz, D., Laurent, P., Lebrun, F., Daigne, F., & Bošnjak, Ž. 2009, ApJ, 695, L208

Grindlay, J. E. 1978, Nature, 273, 211

H. E. S. S. Collaboration, Abramowski, A., Acero, F., et al. 2012, ArXiv e-prints

Hayakawa, S. 1973, Cosmic ray physics: nuclear and astrophysical aspects. (Moskva:Mir)

Heger, A., Fryer, C. L., Woosley, S. E., Langer, N., & Hartmann, D. H. 2003, The Astrophysical Journal, 591, 288

Heitler, W. 1954, Quantum theory of radiation

Helder, E. A., Vink, J., Bassa, C. G., et al. 2009, Science, 325, 719

Hensley, B. S., Siegal-Gaskins, J. M., & Pavlidou, V. 2010, The Astrophysical Journal, 723, 277

Hopkins, A. M., & Beacom, J. F. 2006, The Astrophysical Journal, 651, 142

Horiuchi, S., Beacom, J. F., & Dwek, E. 2009a, Physical Review D, 79, 083013

—. 2009b, Physical Review D, 79, 083013

Horiuchi, S., Beacom, J. F., Kochanek, C. S., et al. 2011, The Astrophysical Journal, 738, 154

Howk, J. C., Lehner, N., Fields, B. D., & Mathews, G. J. 2012, Nature, 489, 121

Hoyle, F. 1954, ApJS, 1, 121

Hunter, S. D., Bertsch, D. L., Catelli, J. R., et al. 1997, The Astrophysical Journal, 481, 205

Iben, Jr., I., & Tutukov, A. V. 1984, ApJS, 54, 335

Iwamoto, K., Mazzali, P. A., Nomoto, K., et al. 1998, Nature, 395, 672

Izotov, Y. I., Chaffee, F. H., Foltz, C. B., et al. 1999, The Astrophysical Journal, 527, 757

Jedamzik, K. 2004, Physical Review D, 70, 063524

Jedamzik, K., & Pospelov, M. 2009, New Journal of Physics, 11, 105028

Johnston, S., Feain, I. J., & Gupta, N. 2009, in Astronomical Society of the Pacific Conference Series, Vol. 407, The Low-Frequency Radio Universe, ed. D. J. Saikia, D. A. Green, Y. Gupta, & T. Venturi, 446

Jones, F. C. 1968, Physical Review, 167, 1159

Jorstad, S. G., Marscher, A. P., Larionov, V. M., et al. 2010, The Astrophysical Journal, 715, 362

Kalemci, E., Boggs, S., Wunderer, C., & Jean, P. 2004, in ESA Special Publication, Vol. 552, 5th INTEGRAL Workshop on the INTEGRAL Universe, ed. V. Schoenfelder, G. Lichti, & C. Winkler, 859

Kazanas, D., & Protheroe, R. J. 1983, Nature, 302, 228

Kennicutt, Jr., R. C. 1998, The Astrophysical Journal, 498, 541

Kirsebom, O. S., & Davids, B. 2011, Physical Review C, 84, 058801

Kistler, M. D., Yüksel, H., Ando, S., Beacom, J. F., & Suzuki, Y. 2011, Physical Review D, 83, 123008

Kneller, J. P., Scherrer, R. J., Steigman, G., & Walker, T. P. 2001, Physical Review D, 64, 123506

Kolb, E. W., & Turner, M. S. 1990, The early universe.

Komatsu, E., Dunkley, J., Nolta, M. R., et al. 2009, ApJS, 180, 330

Komatsu, E., Smith, K. M., Dunkley, J., et al. 2011, ApJS, 192, 18

Korn, A. J., Grundahl, F., Richard, O., et al. 2006, Nature, 442, 657

Kraushaar, W. L., Clark, G. W., Garmire, G. P., et al. 1972, The Astrophysical Journal, 177, 341

Krawczynski, H. 2012, The Astrophysical Journal, 744, 30

Krawczynski, H., Angelini, L., Baring, M., et al. 2013, ArXiv e-prints

Kudritzki, R.-P., & Puls, J. 2000, ARA&A, 38, 613

Kulkarni, S. R., Frail, D. A., Wieringa, M. H., et al. 1998, Nature, 395, 663

Lacki, B. C., Horiuchi, S., & Beacom, J. F. 2012, ArXiv e-prints

Lacki, B. C., Thompson, T. A., & Quataert, E. 2010, The Astrophysical Journal, 717, 1

Lacki, B. C., Thompson, T. A., Quataert, E., Loeb, A., & Waxman, E. 2011, The Astrophysical Journal, 734, 107

Laurent, P., Götz, D., Binétruy, P., Covino, S., & Fernandez-Soto, A. 2011, Physical Review D, 83, 121301

Lazzati, D. 2006, New Journal of Physics, 8, 131

Lebrun, F., Paul, J. A., Bignami, G. F., et al. 1982, A&A, 107, 390

Leitherer, C., Robert, C., & Drissen, L. 1992, The Astrophysical Journal, 401, 596

Lenain, J.-P., & Walter, R. 2011, A&A, 535, A19

Li, W., Chornock, R., Leaman, J., et al. 2011a, *Mon. Not. Roy. Astron. Soc.*, 412, 1473

—. 2011b, *Mon. Not. Roy. Astron. Soc.*, 412, 1473

Li, W., Leaman, J., Chornock, R., et al. 2011c, *Mon. Not. Roy. Astron. Soc.*, 412, 1441

Li, Z.-Y., & Chevalier, R. A. 1999, The Astrophysical Journal, 526, 716

Lien, A., Chakraborty, N., Fields, B. D., & Kemball, A. 2011, The Astrophysical Journal, 740, 23

Lien, A., & Fields, B. D. 2009, *JCAP*, 1, 47

—. 2012, ArXiv e-prints

Lien, A., Fields, B. D., & Beacom, J. F. 2010, Physical Review D, 81, 083001

Loeb, A., & Waxman, E. 2000, Nature, 405, 156

LSST Science Collaboration, Abell, P. A., Allison, J., et al. 2009, ArXiv e-prints

MacFadyen, A. I., & Woosley, S. E. 1999, The Astrophysical Journal, 524, 262

MacFadyen, A. I., Woosley, S. E., & Heger, A. 2001, The Astrophysical Journal, 550, 410

Madau, P., della Valle, M., & Panagia, N. 1998, *Mon. Not. Roy. Astron. Soc.*, 297, L17

Makiya, R., Totani, T., & Kobayashi, M. A. R. 2011, The Astrophysical Journal, 728, 158

Malyshev, D., & Hogg, D. W. 2011, The Astrophysical Journal, 738, 181

Mannucci, F., Della Valle, M., & Panagia, N. 2007, *Mon. Not. Roy. Astron. Soc.*, 377, 1229

Mayer-Hasselwander, H. A., Buccheri, R., Kanbach, G., et al. 1980, in Annals of the New York Academy of Sciences, Vol. 336, Ninth Texas Symposium on Relativistic Astrophysics, ed. J. Ehlers, J. J. Perry, & M. Walker, 211–222

McConnell, M. L., Smith, D. M., Emslie, A. G., et al. 2003, in Bulletin of the American Astronomical Society, Vol. 35, AAS/Solar Physics Division Meeting #34, 850

McConville, W., Ostorero, L., Moderski, R., et al. 2011, The Astrophysical Journal, 738, 148

McNamara, A. L., Kuncic, Z., & Wu, K. 2009, *Mon. Not. Roy. Astron. Soc.*, 395, 1507

Meléndez, J., Casagrande, L., Ramírez, I., Asplund, M., & Schuster, W. J. 2010a, A&A, 515, L3

Meléndez, J., Ramírez, I., Casagrande, L., et al. 2010b, Astrophysics and Space Science, 328, 193

Meyer, E. T., Fossati, G., Georganopoulos, M., & Lister, M. L. 2012, ApJ, 752, L4

Miniati, F. 2002, *Mon. Not. Roy. Astron. Soc.*, 337, 199

Mokiem, M. R., de Koter, A., Vink, J. S., et al. 2007, A&A, 473, 603

Montes, M. J., Weiler, K. W., & Panagia, N. 1997, The Astrophysical Journal, 488, 792

Moskalenko, I. V., & Porter, T. A. 2009, ApJ, 692, L54

Moskalenko, I. V., & Strong, A. W. 2000, The Astrophysical Journal, 528, 357

Mücke, A., & Pohl, M. 2000, *Mon. Not. Roy. Astron. Soc.*, 312, 177

Mukhanov, V. 2004, International Journal of Theoretical Physics, 43, 669

Munari, U., Barbon, R., Piemonte, A., Tomasella, L., & Rejkuba, M. 1998, A&A, 333, 159

Murphy, E. J., Porter, T. A., Moskalenko, I. V., Helou, G., & Strong, A. W. 2012, The Astrophysical Journal, 750, 126

Nakano, S., & Aoki, M. 1997, IAU circ., 6795, 2

Nalewajko, K. 2013, *Mon. Not. Roy. Astron. Soc.*, 598

Nolan, P. L., Abdo, A. A., Ackermann, M., et al. 2012a, ApJS, 199, 31

—. 2012b, ApJS, 199, 31

Nomoto, K., Thielemann, F.-K., & Yokoi, K. 1984, The Astrophysical Journal, 286, 644

Novick, R. 1975, Space Science Reviews, 18, 389

O'Malley, P. D., Bardayan, D. W., Adekola, A. S., et al. 2011, Physical Review C, 84, 042801

O'Meara, J. M., Burles, S., Prochaska, J. X., et al. 2006, ApJ, 649, L61

Padovani, P., Ghisellini, G., Fabian, A. C., & Celotti, A. 1993, *Mon. Not. Roy. Astron. Soc.*, 260, L21

Paglione, T. A. D., & Abrahams, R. D. 2012, The Astrophysical Journal, 755, 106

Palanque-Delabrouille, N., Ruhlmann-Kleider, V., Pascal, S., et al. 2010, A&A, 514, A63

Panagia, N., Van Dyk, S. D., Weiler, K. W., et al. 2006, The Astrophysical Journal, 646, 369

Papenkova, M., Li, W. D., Wray, J., Chleborad, C. W., & Schwartz, M. 2001, IAU circ., 7722, 1

Pavlidou, V., & Fields, B. D. 2001, The Astrophysical Journal, 558, 63

—. 2002, ApJ, 575, L5

Persic, M., & Rephaeli, Y. 2010, *Mon. Not. Roy. Astron. Soc.*, 403, 1569

—. 2011, ArXiv e-prints

—. 2012, ArXiv e-prints

Phillips, M. M. 1993, ApJ, 413, L105

Pieper, S. C., Varga, K., & Wiringa, R. B. 2002, Physical Review C, 66, 044310

Pohl, M. 1993, A&A, 270, 91

—. 1994, A&A, 287, 453

Pooley, D., Lewin, W. H. G., Fox, D. W., et al. 2002, The Astrophysical Journal, 572, 932

Porter, T. A., Moskalenko, I. V., Strong, A. W., Orlando, E., & Bouchet, L. 2008, The Astrophysical Journal, 682, 400

Price, P. A., Berger, E., Reichart, D. E., et al. 2002, ApJ, 572, L51

Regis, M., & Ullio, P. 2008, Physical Review D, 78, 043505

Reimer, A. 2012, Journal of Physics Conference Series, 355, 012011

Riess, A. G., Press, W. H., & Kirshner, R. P. 1996, The Astrophysical Journal, 473, 88

Robitaille, T. P., & Whitney, B. A. 2010, ApJ, 710, L11

Rossi, E. M., Lazzati, D., Salmonson, J. D., & Ghisellini, G. 2004, *Mon. Not. Roy. Astron. Soc.*, 354, 86

Ryan, S. G., Beers, T. C., Olive, K. A., Fields, B. D., & Norris, J. E. 2000, ApJ, 530, L57

Rybicki, G. B., & Lightman, A. P. 1986, Radiative Processes in Astrophysics

Sako, M., Bassett, B., Becker, A., et al. 2008, The Astronomical Journal, 135, 348

Salamon, M. H., & Stecker, F. W. 1998, The Astrophysical Journal, 493, 547

Salpeter, E. E. 1955, The Astrophysical Journal, 121, 161

Sanders, D. B., Mazzarella, J. M., Kim, D.-C., Surace, J. A., & Soifer, B. T. 2003, The Astronomical Journal, 126, 1607

Scheuer, P. A. G. 1957, Proceedings of the Cambridge Philosophical Society, 53, 764

Smartt, S. J., Eldridge, J. J., Crockett, R. M., & Maund, J. R. 2009, *Mon. Not. Roy. Astron. Soc.*, 395, 1409

Smith, M. S., Kawano, L. H., & Malaney, R. A. 1993, ApJS, 85, 219

Soderberg, A. M. 2007, in American Institute of Physics Conference Series, Vol. 937, Supernova 1987A: 20 Years After: Supernovae and Gamma-Ray Bursters, ed. S. Immler, K. Weiler, & R. McCray, 492–499

Soderberg, A. M., Chevalier, R. A., Kulkarni, S. R., & Frail, D. A. 2006a, The Astrophysical Journal, 651, 1005

Soderberg, A. M., Frail, D. A., & Wieringa, M. H. 2004, ApJ, 607, L13

Soderberg, A. M., Nakar, E., Berger, E., & Kulkarni, S. R. 2006b, The Astrophysical Journal, 638, 930

Sorcia, M., Benítez, E., Hiriart, D., et al. 2013, ArXiv e-prints

Spite, F., & Spite, M. 1982, A&A, 115, 357

Sreekumar, P., Bertsch, D. L., Dingus, B. L., et al. 1998, The Astrophysical Journal, 494, 523

Stecker, F. W., Malkan, M. A., & Scully, S. T. 2012, ArXiv e-prints

Stecker, F. W., Salamon, M. H., & Malkan, M. A. 1993, ApJ, 410, L71

Stecker, F. W., & Venters, T. M. 2011, The Astrophysical Journal, 736, 40

Steigman, G. 2007, Annual Review of Nuclear and Particle Science, 57, 463

Stockdale, C. J., Kelley, M. T., Weiler, K. W., et al. 2007, in American Institute of Physics Conference Series, Vol. 937, Supernova 1987A: 20 Years After: Supernovae and Gamma-Ray Bursters, ed. S. Immler, K. Weiler, & R. McCray, 264–268

Stockdale, C. J., Weiler, K. W., Van Dyk, S. D., et al. 2003, The Astrophysical Journal, 592, 900

Strong, A. W., & Moskalenko, I. V. 1998, The Astrophysical Journal, 509, 212

Strong, A. W., Moskalenko, I. V., & Reimer, O. 2000, The Astrophysical Journal, 537, 763

Strong, A. W., Orlando, E., & Jaffe, T. R. 2011, A&A, 534, A54

Strong, A. W., Porter, T. A., Digel, S. W., et al. 2010, ApJ, 722, L58

Strong, A. W., Wolfendale, A. W., & Worrall, D. M. 1976a, Journal of Physics A Mathematical General, 9, 1553

—. 1976b, *Mon. Not. Roy. Astron. Soc.*, 175, 23P

—. 1976c, *Mon. Not. Roy. Astron. Soc.*, 175, 23P

Teichmann, T., & Wigner, E. P. 1952, Physical Review, 87, 123

Thompson, T. A., Quataert, E., & Waxman, E. 2007, The Astrophysical Journal, 654, 219

Tilley, D. R., Kelley, J. H., Godwin, J. L., et al. 2004, Nuclear Physics A, 745, 155

Torres, D. F., Reimer, O., Domingo-Santamaría, E., & Digel, S. W. 2004, ApJ, 607, L99

Uchiyama, Y., Aharonian, F. A., Tanaka, T., Takahashi, T., & Maeda, Y. 2007, Nature, 449, 576

VERITAS Collaboration, Acciari, V. A., Aliu, E., et al. 2009, Nature, 462, 770

Vink, J. S., de Koter, A., & Lamers, H. J. G. L. M. 2001, A&A, 369, 574

Voelk, H. J. 1989, A&A, 218, 67

Völk, H. J., Aharonian, F. A., & Breitschwerdt, D. 1996, Space Science Reviews, 75, 279

Wagoner, R. V., Fowler, W. A., & Hoyle, F. 1967a, The Astrophysical Journal, 148, 3

—. 1967b, The Astrophysical Journal, 148, 3

Wainscoat, R. J., Cohen, M., Volk, K., Walker, H. J., & Schwartz, D. E. 1992, ApJS, 83, 111

Wardle, J. F. C., & Kronberg, P. P. 1974, The Astrophysical Journal, 194, 249

Webber, W. R., Simpson, G. A., & Cane, H. V. 1980, The Astrophysical Journal, 236, 448

Webbink, R. F. 1984, The Astrophysical Journal, 277, 355

Wehrle, A. E., Marscher, A. P., Jorstad, S. G., et al. 2012, The Astrophysical Journal, 758, 72

Weiler, K. W., Panagia, N., Montes, M. J., & Sramek, R. A. 2002, ARA&A, 40, 387

Weiler, K. W., Panagia, N., & Sramek, R. A. 1990, The Astrophysical Journal, 364, 611

Weiler, K. W., Panagia, N., Sramek, R. A., et al. 2009, in American Institute of Physics Conference Series, Vol. 1111, American Institute of Physics Conference Series, ed. G. Giobbi, A. Tornambe, G. Raimondo, M. Limongi, L. A. Antonelli, N. Menci, & E. Brocato, 440–447

Weiler, K. W., Sramek, R. A., Panagia, N., van der Hulst, J. M., & Salvati, M. 1986, The Astrophysical Journal, 301, 790

Weiler, K. W., van Dyk, S. D., Sramek, R. A., & Panagia, N. 2004, New Astronomy Review, 48, 1377

Weiler, K. W., Williams, C. L., Panagia, N., et al. 2007, The Astrophysical Journal, 671, 1959

Weiß, A., Neininger, N., Hüttemeister, S., & Klein, U. 2001, A&A, 365, 571

Weisskopf, M. C., Elsner, R. F., & O'Dell, S. L. 2010, in Society of Photo-Optical Instrumentation Engineers (SPIE) Conference Series, Vol. 7732, Society of Photo-Optical Instrumentation Engineers (SPIE) Conference Series

Wellons, S., & Soderberg, A. M. 2011, in Bulletin of the American Astronomical Society, Vol. 43, American Astronomical Society Meeting Abstracts #217, #337.15

Woosley, S. E. 1993, The Astrophysical Journal, 405, 273

Woosley, S. E., & Bloom, J. S. 2006, ARA&A, 44, 507

Woosley, S. E., Eastman, R. G., & Schmidt, B. P. 1999, The Astrophysical Journal, 516, 788

Yan, J., Cecil, F. E., Greife, U., et al. 2002, Physical Review C, 65, 048801

Zacharias, M., & Schlickeiser, R. 2012, *Mon. Not. Roy. Astron. Soc.*, 420, 84